Finite Element Analysis of Probe Induced Delamination of a Thin Film at an Edge Interface

Kristopher P. Mount

Thesis submitted to the Faculty of the
Virginia Polytechnic Institute and State University
in partial fulfillment of the requirements for the degree of

Master of Science

in

Mechanical Engineering

APPROVED:

_____

Dr. Robert L. West, Jr.
Chairman

_____ _____

Dr. David A. Dillard **Dr. Kai-Tak Wan**

December 19, 2002

Blacksburg, Virginia

Keywords: Adhesive Blister Test, Finite Elements, Energy Release Rates, Half-Blister

Finite Element Analysis of Probe Induced Delamination of a Thin Film at an Edge Interface

by

Kristopher P. Mount

Dr. Robert L. West, Jr, Chairman
Mechanical Engineering

Abstract

Energy release rates are extracted from non-linear finite element analyses of a thin film bonded to a rigid substrate that is shaft-loaded at its free edge. This geometry is of interest because it simulates a probe test that has proven to be useful in characterizing the adhesion of thin, microelectronic coatings bonded to silicon wafers. Preliminary experimental results indicate that out-of-plane rather than in-plane loading dominates failure in the system. This work therefore focuses on out-of-plane film loading. To validate finite element and energy release rate methodologies, energy release rates from finite element analyses of pressurized and shaft-loaded blister tests are first correlated to theoretical limit cases. Upon validation, mode I, mode II, and mode III energy release rates are extracted from three-dimensional continuum finite element models of the edge-loaded thin film by a three-dimensional modified crack closure method. Having assumed a circular debond as observed experimentally, energy release rates are determined by a step-wise approach around the circumference. The progression of debond is simulated in multiple analyses by altering the boundary conditions associated with increasing the debond radius. Mechanical loading is supplemented with thermal loading, introducing residual stresses in the non-linear analyses. A sensitivity analysis of energy release rates to residual stress is performed. The results indicate that inclusion of residual stress has an important role in both the magnitude and mode-mixity of energy release rates in the thin film. Increasing the length of debond effectively transitions the film from a shearing mode to a bending mode, thereby significantly impacting each mode of energy release rate differently.

Acknowledgments

I would first like to thank my advisor, Bob West, for his guidance, concern, availability, understanding, and patience. He was always willing to lend a helping hand when I came across any troubles, whether they be associated with academics or life in general. Dr. West perhaps unknowingly passed on to me many lessons that I will carry with me the rest of my life.

I would also like to thank my two committee members, Dave Dillard and Kai-tak Wan. Their interest in the subject matter kept the research on the right path. I greatly appreciate their constant support and insight. Bob West and I had little knowledge of fracture mechanics at the start, and we both leaned on the expertise of these two throughout the project.

Thank you to Hewlett-Packard for funding this research.

A special thanks goes to Ken Liechti for giving my work a once over and inspiring confidence in my results.

I would like to thank my family and friends for their constant support and understanding. To my parents, for their advice and constant presence, I love you very much. I know you'll be happy that my six years of college have finally come to an end. To Kevin, who has always had me look on the brighter side of things, even if he didn't realize he was doing so. To Carol and R.O. Settle, Mark Koch, Tony Harris, Jason Surratt, Tamara Loan, Philip Riffe, Abigaille Laxa, Dustin Shanahan, Hieu Le, Christie and Louie Heslip, and Nora Turner: thank you for listening to me complain, for being there whenever I needed it, and for providing the much needed relief outside of work. I could not have asked for better friends, without you guys the road would have been much rockier.

Finally, I would especially like to thank Celia Dew for all her love. There are some things that no one should have to endure, and I could not have asked for more from her.

She will always hold a very special place in my heart. I cannot even begin to explain all that I've learned from her. She always showed me that,

"Love is patient, love is kind …
Love bears all things, believes all things,
hopes all things, endures all things. "
1 Corinthians 13:4,7

and that, …. I will never forget and will always believe.

Table of Contents

List of Figures

List of Tables

Nomenclature

A
a – crack length (mm)
a - coefficient of thermal expansion (mm/mm)
a_I - initial crack length (mm)
a_f – final crack length (mm)

C
CC – crack closure method

D
da – crack length increment (mm)
ds – change in entropy ($kJ/(kg \times K)$)
DA – surface area resulting from crack propagation (mm^2)

E
E – elastic modulus (MPa)

F
F_c – x-force required to hold crack together (N)

G
G_{total} – total energy release rate (J/m^2)
G_I – mode I energy release rate (J/m^2)
G_{II} – mode II energy release rate (J/m^2)
G_{III} – mode III energy release rate (J/m^2)
G – energy release rate (J/m^2)
G_c – critical energy release rate (J/m^2)
g - fracture surface energy (N)

H
h – film thickness (mm)
h/a – thickness to crack length ratio

I
IM – infinite medium theory

K
K_c – fracture toughness ($MPa\ddot{O}m$)
K – (SIF) stress intensity factor ($MPa\ddot{O}m$)

M
MCCM – modified crack closure method

N
u - Poisson's ratio

P
P - load (N)
p – pressure (MPa)
Φ - dimensionless fracture parameter
ψ - mode mixity parameter (°)

R
r – radius (mm)

S
SFT – stress free temperature (°C)
SNR –signal to noise ratio
STR – change in strain energy method
s_a – applied stress (MPa)
s_y – crack tip normal stress (MPa)
s_x – standard deviation
s_x^2 – variance

T
T – temperature ($°C$)
t - crack tip shear stress (MPa)
TP – thin plate theory
T_c – y-force required to hold crack together (N)

U
$U_{elastic}$ – elastic energy of system ($N \times m$)
U_g - surface energy ($N \times m$)
U_{load} – energy induced by load ($N \times m$)
U_S – strain energy ($N \times m$)
U_{total} – total system energy ($N \times m$)

V
V – volume (mm^3)

W

w_0 – central max blister deflection

$w(r)$ – displacement field (mm)

w_0/a – max displacement to crack length ratio

Y

y – displacement (mm)

Chapter 1 Introduction

1.1 Overview

There is a growing need for systems of thin films bonded to silicon or other substrates in the microelectronics industry. Thin film technology is used in a wide range of applications: as coatings for thermal, chemical, or wear protection, as conductive lines in integrated circuits and electronics packages, and as functional layers in actuators. The integrity of the adhesion between the thin film and its adjoining substrate is a controlling factor in the design of thin film systems. Adhesive failure is initiated by mechanisms that attack the system such as mechanical loading, processing, mismatched coefficients of thermal expansion between film and substrate resulting in residual stresses, and adverse chemical environments that alter the chemistry of the bond. Mechanical characterization of the deformation and ultimate failure of thin films is essential to the design of durable and robust systems.

An experimental probe test has been developed based on observed failures of adhesion between microelectronic coatings and substrates under operating environments. Delamination of coatings tends to initiate along free edges due to the vulnerability of the interface between coating and substrate to the surrounding environment. The probe test mechanically loads the coating with a cylindrical punch at a 45° angle to the edge it creates with the substrate, as illustrated in Figure 1.1.

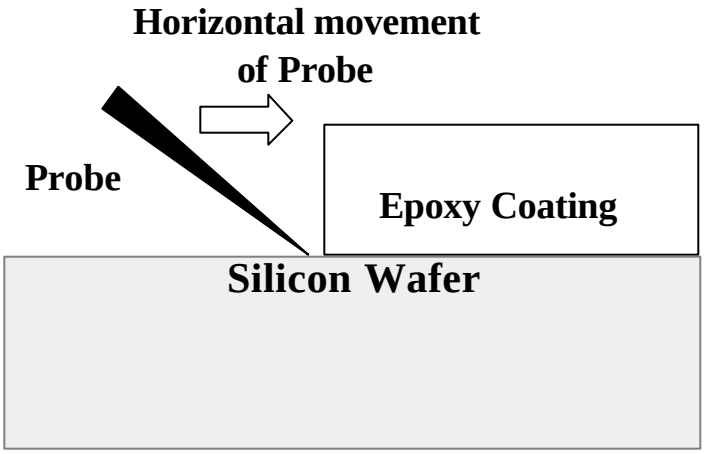

Figure 1.1. Schematic of experimental probe test setup

The loading of Figure 1.1 simulates delamination at the coating's edge that may be induced under in-situ conditions. The test captures the energies associated with delamination based on calculations from the interference fringes developed by loading, and also the final equilibrium dimension (radius) of the circular delamination. A picture of actual experimental delamination patterns of the probe test can be found in Figure 1.2.

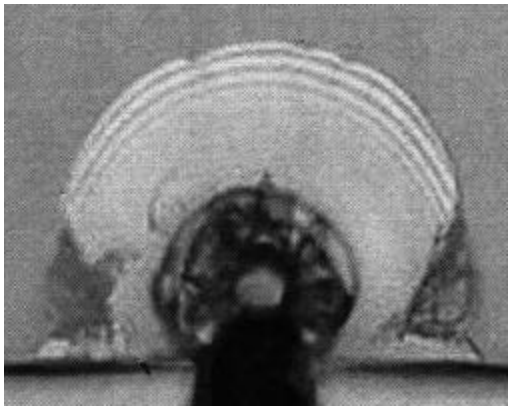

Figure 1.2. Delamination patterns from probe test of microelectronic coating

The focus of this research is to quantify adhesion of the microelectronic coating by applying fracture mechanics methodologies to a finite element analysis of the probe test. Fracture mechanics is a useful tool in understanding delamination of thin films from substrates. By accounting for the change in energies associated with applied loading, sample geometry, and creation of new area, the methods of fracture mechanics are able to determine whether or not the flaw will propagate and lead to failure. The robustness of the fracture mechanics approach comes from its use of stresses combined with displacements, strains, and conservation of energy principles to predict failure conditions and establish adhesive design criteria.

The loading inherent in the probe test setup induces both in-plane and out-of-plane displacements in the coating. Thin films are much stiffer in-plane than out-of-plane, and therefore it is assumed that out-of-plane displacements will dominate failure. On this basis, the work of this thesis focuses upon delamination by out-of-plane deformations. Various fracture mechanics tests have been specifically developed to analyze out-of-plane delamination mechanisms in thin films. One classical test is the pressurized blister test of a thin film. This test is used to determine the critical energy levels associated with

debond propagation in the blister with respect to parameters such as magnitude of loading, film thickness, and material properties. Another classical test is the shaft-loaded blister test, a derivative of the pressurized blister test that explores the same mechanisms of debond as the pressurized blister test but with a different type of loading. These classical tests will be used to validate finite element and fracture mechanics methodologies. Upon validation, these methodologies will be used to examine the experimental test case of probe-induced delamination of thin microelectronic coatings at their edge interface with silicon substrates.

1.2 Problem statement

Of particular interest in this study is to determine how a thin epoxy film adhered to a silicon substrate fails when subjected to both mechanical loading and residual stresses caused by the curing of the adhesive. Analysis of failure is to include determination of the relative strain energy release rates associated with a specific mechanism of failure. Additionally, the quantification of the deformation mechanics of debond, analysis of the effects of length of debond radius on strain energy release rates, and analysis of the sensitivity of strain energy release rates to residual stress will be investigated.

1.3 Hypothesis

The general hypothesis of this research is that it is possible to characterize the mechanisms of failure in mechanically and thermally loaded thin films adhered to substrates by using fracture mechanics techniques with finite element analyses. Furthermore, it is hypothesized that: i) finite element results can be shown to correlate with theory for classical blister testing, and ii) finite element analyses can provide solutions beyond the limits of theory in both classical blister testing and edge-loaded films.

1.4 Objectives

The primary objective of this research is to establish a means of quantifying the energy release rates associated with fracture modes in a thin film/substrate system in order to understand fracture patterns. More specific objectives are as follows:

1. Identify the significant adhesive model parameters within fracture mechanics that are representative of integrity of adhesion,
2. Develop finite element methods by which fracture parameters can be determined,
3. Identify types of finite element models and elements suitable for fracture analysis of thin film/substrate systems,
4. Propose key classical test methods that explore the capabilities of thin films bonded to substrates,
5. Explore classical idealized blister solutions in the framework of design parameters so as to bound finite element solutions with limiting cases and ensure model correlation for these limit cases,
6. Interpret finite element results so as to:
    a) Understand the effects of both mechanical loading and residual stresses due to thermal loading,
    b) Quantify the energy release rates associated with the different fracture modes of failure during debond,
    c) Characterize the sensitivity of design parameters to debond length,
7. Transfer finite element methodology developed for classical blister tests to thin films loaded at the edge of film and substrate.

1.5 Statement of Literature Review

Sufficient references to literature exist in Chapters 2 and 3 to warrant the exclusion of a redundant review chapter encompassing all of the referred literature. Hence, the chapter is omitted, and extensive referencing occurs throughout the thesis.

1.6 Scope of Research

Although the area of thin film testing is very broad, the focus of this work lies in modeling thin film bonded systems using the finite element method to extract the energy release rates. The following areas are restricted in development in this thesis.

Linear elastic material definition

All finite element and analytical analyses are restricted to linear elastic material definitions. At the onset of this work, material parameters beyond those needed to specify linear elasticity were not available. However, large displacements, large strains are captured in the analyses with non-linear geometry.

Static analysis

All analyses are static, or quasi-static. Dynamic cases have not been considered.

Loading

Both mechanical and thermal loading have been held constant in each analysis. Therefore the sensitivity of the thin films to magnitude of loading has not been analyzed. Mechanical loading is out-of-plane; in-plane loading is not accounted for.

Initiation of cracking

This thesis is based on propagating an existing crack. The work does not predict where a crack will initiate in a material.

Mode of failure in edge-loaded film

Two failure modes, buckling and wedging, are thought to drive failure in edge loaded thin film systems. This study only concerns the wedging phase of failure. Buckling would require an entirely separate linear perturbation eigenvalue analysis to estimate critical loads, which has not been undertaken.

1.7 Outline

The chapters of this thesis build upon one another to reach the ultimate goal of the research, the experimental probe geometry. Chapter 2 reviews the concepts in fracture mechanics pertinent to this study. Chapter 2 also develops general analytical expressions for energy release rates of blister testing, and introduces finite element fracture mechanics methodologies for obtaining energy release rates. Chapter 3 describes element types in ABAQUS and explores the best choice of element selection for blister testing. Chapters 4 and 5 introduce the pressurized blister test and the shaft-loaded blister test, respectively. Each chapter correlates axisymmetric and three-dimensional finite element results to theory as a means of validating the finite element models. The blisters are shown to transition between two theoretical extremes – infinite medium to thin plate, thereby demonstrating blister behavior dependence on length of debond. The blisters are also analyzed for energy release rate sensitivity to residual stresses from thermal loading. Finally, insight into the mode of failure is investigated by mode-mixity analyses. Chapter 6 harnesses the insight gained from the models of Chapters 4 and 5 and applies that to simulate edge loading of a thin coating; the probe test geometry. A new technique for determining energy release rates at various points about an assumed debond front is developed. The probe-loaded coatings are analyzed for energy release rate sensitivity to residual stress. Finally, the effects of length of debond radius on energy release rates and mode-mixity are investigated. Chapter 7 summarizes the research and makes recommendations for future work on the project.

Chapter 2 Fracture mechanics

2.1 Background

The development of the field of fracture mechanics originally came about by failures in structures designed on the basis of limiting the maximum stress in the structure to a certain percentage of the tensile strength of the material. Intuition led engineers to begin considering the effects of geometrical stress intensifiers and inherent material flaws. The founding of fracture mechanics is often attributed to both C.E. Inglis and A.A. Griffith. In 1913, Inglis [1] showed that the local stresses around a notch, corner, or hole could be much higher than the average stress of the specimen. Using elasticity theory, Inglis demonstrated that the degree of stress concentration was dependent upon the flaw geometry. Based on these studies, Inglis defined stress concentration factors. In the 1920's Griffith [2] analyzed Inglis's work and found stress concentration factors to be inadequate in certain cases. Griffith's work ultimately became the foundation of modern fracture theory. Griffith explored Inglis's results by investigating the effect of scratches on fatigue. He confirmed that scratches could increase the stress and strain level by a factor of between two and six. However, Griffith also found that the maximum stress or strain on a certain specimen was the same no matter what the size of the scratch was, as long as the scratches were geometrically similar. Since this conclusion conflicted with his fatigue results, Griffith rejected the theory that simple critical stress or strain criteria could predict fracture for sharp cracks or notches, and instead turned to basic energy concepts [3]. Griffith assumed that all real "elastic" bodies have inherent cracks in them and hypothesized that in order to make the most critical of these cracks grow, the strain energy released from crack propagation must be equal to or greater than the surface energy required to create new crack faces [4]. Griffith's energy balance criterion for crack growth can be expressed mathematically for an increment of crack extension as [5]:

$$\frac{dU_S}{da} \geq \frac{dU_g}{da} \tag{2.1}$$

where U_s is the strain energy, U_g is the surface energy and da is the crack length increment. Thus, Eq. (2.1) states that the strain energy release rate must be greater than

or equal to the surface energy creation rate for crack growth to occur. For a double ended crack of length $2a$ in an infinite plate of unit width under a uniformly applied stress σ_a, the strain energy, U_s, becomes [5]

$$U_S = \frac{\pi \sigma_a^2 a^2 (1-\nu^2)}{E} \tag{2.2}$$

where E is the elastic modulus and ν is Poisson's ratio. The total surface energy, U_g, becomes

$$U_g = 4\gamma a \tag{2.3}$$

where γ is the fracture surface energy. Substituting Eq. (2.2) and Eq. (2.3) into Eq. (2.1) and taking the derivative with respect to crack length yields the critical condition for crack growth [5],

$$\frac{\pi \sigma_a^2 a(1-\nu^2)}{E} \geq 2\gamma . \tag{2.4}$$

According to a history by B. Cotterell [3], G.R. Irwin [6] went on to define the strain energy release rate as the crack extension force, G. Fracture would then initiate when G reached a critical value, G_c. Irwin's collaborator, J.A. Kies [7] observed that the critical stress for a given crack size depended only on G_cE, where E is the elastic modulus. In recognition of Kies, Boeing engineers [8] later termed $(G_cE)^{1/2}$ the fracture toughness, K_c. Irwin [9] similarly established the stress intensity factor (*SIF*) $K=(GE)^{1/2}$. Both the fracture toughness and the *SIF* term are valid only for plane stress conditions. A Poisson's correction is required for plane strain or other conditions. Applying the stress intensity factor to a center crack in an infinite plate subjected to a uniform stress σ_a yields [10],

$$K = \sigma_a \sqrt{\pi a} . \tag{2.5}$$

Thus two equivalent fracture mechanics approaches were established: one based on energy release rates, G, and the other based on stress intensity factors, K. Both methods offer a finite quantification of unbounded stress states at the crack tip. The difference between the two approaches lies in what they represent: stress intensity factors (K) characterize the magnitude of *stresses* surrounding the crack tip whereas strain energy release rates (G) quantify the *energy* available in a unit area to propagate a crack.

There are three modes of fracture, I, II, and III, as illustrated in Figure 2.1 below [10].

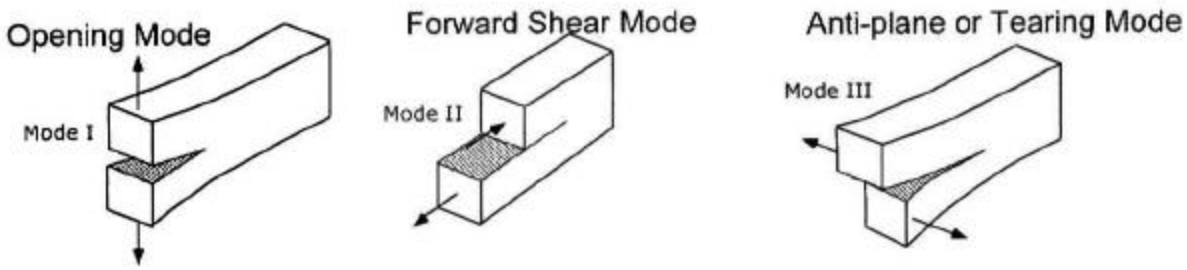

Figure 2.1. Schematics of modes of fracture [10]

Oftentimes, a specimen is loaded in such a way that more than one type of mode is present. Since G values are based on energy, and energies are additive, the energy release rate for a multi-mode loaded specimen is as follows:

$$G_{total} = G_I + G_{II} + G_{III} \tag{2.6}$$

Although the two fracture mechanics approaches are equivalent by $K=(GE)^{1/2}$ for plane stress conditions, finite element work in this research will focus on Griffith-type fracture behavior (G values) as opposed to Irwin-type fracture behavior (K values). This is based on the fact that the use of strain energy release rates is often preferred for bonded systems [10]. The use of G has been accepted as the standard fracture parameter because of both its convenience and its basis on a sound energy balance principle [11].

2.2 Energy release rates in blister tests

As stated in Section 2.1, strain energy release rates quantify the energy available in a given unit area to propagate a crack. A crack can be anticipated to propagate in areas where the magnitude of strain energy release rate is highest. The following analysis of development of energy release rate expressions is based on personal discussions with Wan [12]. Determination of energy release rates for blister tests begins with a simple energy balance.

$$U_{total} = -U_{load} + \left[U_{elastic} + U_g\right] \tag{2.7}$$

$$-dU_{total} = d\left[U_{load} - U_{elastic}\right] - dU_g$$

With surface energy, dU_g, defined as follows,

$$dU_g = G_c dA \tag{2.8}$$

where dA is an incremental area created by crack propagation. The energy balance becomes

$$\frac{-dU_{total}}{dA} = \frac{d}{dA}\left[U_{load} - U_{elastic}\right] - G_c$$

From the 2nd law of thermodynamics,

$$dU_{total} = -TdS \tag{2.9}$$
$$dS \geq 0$$

where T is temperature ($°K$), and dS is change in entropy ($kJ/(kg{\cdot}K)$). Therefore,

$$-TdS = dU_{total} \leq 0$$

and

$$\frac{d}{dA}\left[U_{load} - U_{elastic}\right] - G_c \geq 0$$

which represents the Griffith fracture criticality condition:

$$G = \frac{d}{dA}\left[U_{load} - U_{elastic}\right] \geq G_c \tag{2.10}$$

Eq. 2.10 holds true for both linear and non-linear systems. In order to better understand this expression, we observe a load-displacement curve,

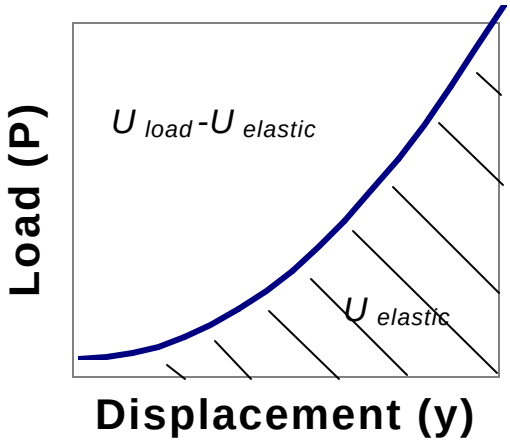

Figure 2.2. Nonlinear load-displacement curve

where

$$U_{load} = Py$$
$$U_{elastic} = \int Pdy \tag{2.11}$$

In a linear elastic analysis, the load-displacement curve becomes,

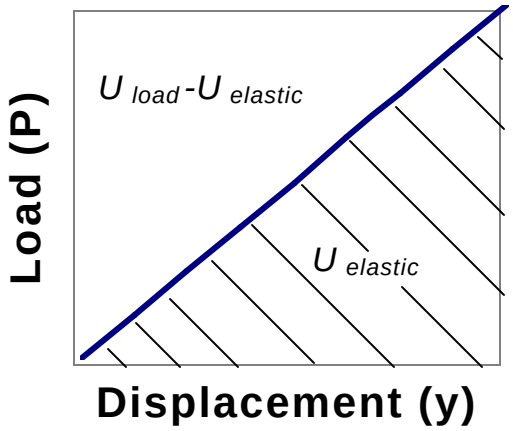

Figure 2.3. Linear elastic load-displacement curve

and Eq. (2.11) becomes,

$$U_{elastic} = \tfrac{1}{2} Py = \tfrac{1}{2} U_{load} \tag{2.12}$$

Rearranging the results of Eq. (2.12) and incorporating into Eq. (2.10) gives the expression for energy release rate, G,

$$G = \frac{d}{dA}\left|2U_{elastic} - U_{elastic}\right| = \left|\frac{dU_{elastic}}{dA}\right| \tag{2.13}$$

This equation only applies to linear elastic fracture mechanics problems. Irwin [6] went on to state that crack propagation occurs when the available energy release rate, G, equals the critical energy release rate, G_c,

$$G = G_c.$$

The following section develops finite element techniques for obtaining energy release rates numerically.

2.3 Finite element fracture mechanics methods

2.3.1 Introduction

Finite element analyses often provide solutions to problems where closed-form solutions are not available due to complex shapes, loading conditions, or boundary conditions. For this reason, finite element approaches for solving linear elastic fracture mechanics problems have been investigated for the past three decades. Most prominent contributors to fracture mechanics have either used, or have considered using finite element techniques to solve fracture mechanics problems. The finite element methods developed over the years include:

- computing the change in strain energy for two crack lengths [13]
- computing a change in compliance for two crack lengths [4]
- performing the virtual crack closure method [14]
- evaluating the J-integral [15]

These methods require one or more analyses in order to obtain an accurate energy release rate. Depending upon the specifics of the problem at hand, some methods are more economical than others, and some provide more accurate results. This thesis considers the change in strain energy approach, the virtual crack closure method, and the J-integral method for blister-type testing. The change of strain energy approach was chosen for its convenience, and the modified crack closure method and the J-integral method are the two most popular ways of computing energy release rates in finite element analyses. The methods are described and developed in the ensuing sections and are compared for efficiency and adherence to theory in the blister tests analyzed in Chapters 4 and 5.

2.3.2 Change in strain energy approach

The change in strain energy approach is the simplest method for obtaining energy release rate results. The method requires two analyses in order to obtain the model strain energy at an initial crack length, a_i, and at a final crack length, a_f. Using the finite element code ABAQUS 6.1, strain energy can be directly queried from a model. Dividing the change in strain energy by the new surface area resulting from crack propagation, ΔA, yields the total energy release rate [13],

$$G_{total} = \frac{(U_S(a_f) - U_S(a_i))}{\Delta A} = -\frac{dU_S}{dA} \tag{2.14}$$

Unfortunately, this approach is unable to distinguish between the different modes of fracture. The approach lumps all modes of G into G_{total}.

2.3.3 Modified crack closure method

Several different forms of the crack closure method are scattered throughout the literature. Rybicki and Kanninen [14] proposed perhaps the most convenient way of evaluating G, known as the modified crack closure method (MCCM). Their method is based on Irwin's assumption that if a crack extends by a small amount Δa, the energy absorbed in creating the crack is equal to the work required to close the crack to its original length. Hence, this method is also referred to as the virtual crack closure method. In equation form, this statement is

$$\begin{aligned} G = \lim_{\Delta a \to 0} \frac{1}{2\Delta a} \int_0^{\Delta a} s_y(\Delta a - r, 0)\bar{v}(r, p)dr + \\ \lim_{\Delta a \to 0} \frac{1}{2\Delta a} \int_0^{\Delta a} t_{xy}(\Delta a - r, 0)\bar{u}(r, p)dr \end{aligned} \tag{2.15}$$

where G is the energy release rate, Δa is the crack increment, s_y and t_{xy} are the stresses near the crack tip, and u and v are the relative sliding and opening displacements. The first and second integrals of Eq. (2.15) yield the expressions for the energy release rates for mode I and mode II deformations, respectively. The mode I energy release rate becomes the first line of Eq. (2.15), and the mode II energy release rate becomes the second line. Rybicki and Kanninen's MCCM can be translated to a finite element analysis based on nodal forces and displacements. The key to the translation is to think of the energy release rates as being the amount of work required to close a crack an amount Δa. In the finite element representation of Figure 2.4, this is one half the product of the forces and displacements at a and b required to close these nodes.

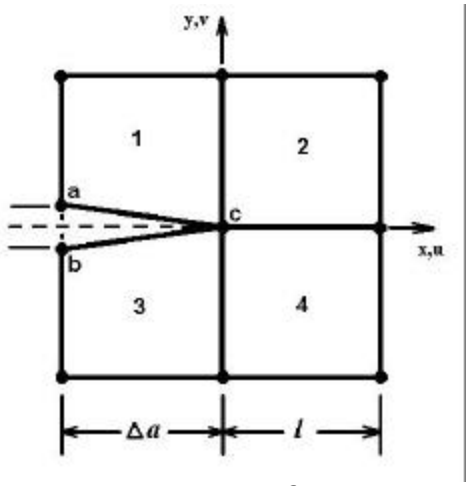

Figure 2.4. 2-D Illustration of crack closure method

The energy release rate expressions for a 2-D representation are,

$$G_I = \lim_{\Delta a \to 0}\left[\frac{1}{2\Delta a} F_a\left(v_a - v_b\right)\right] \tag{2.16}$$

$$G_{II} = \lim_{\Delta a \to 0}\left[\frac{1}{2\Delta a} T_a\left(u_a - u_b\right)\right] \tag{2.17}$$

The values of F_a and T_a are taken to be the y and x forces, respectively, required to hold nodes a and b together, thereby preventing crack growth. To maintain a single analysis, the forces at a and b can be approximated to be equal to the forces at c, if and only if length l is equivalent to length Δa, and elements 1,2,3, and 4 are of the same proportions. The values v_a, v_b, u_a, and u_b are the y-x displacements of nodes a and b.

In practice, the MCCM compares favorably to other methods of obtaining strain energy release rates. Sankar and Pinheiro [11,16] performed comparison studies of strain energy release rate methods. They compared finite element methods such as the J-integral, crack tip force method, and the crack closure method to the analytical method. They used three specimens; the double cantilever beam (DCB), the end notch flexure specimen (ENF), and the cracked lap shear specimen (CLS). The DCB best represents the opening mode, or mode I crack propagation. With this specimen, Sankar and Pinheiro found negligible difference in energy release rate between the crack closure method and any finite element method or analytical technique.

The advantage of the crack closure method is its ability to distinguish between the different modes of fracture. In axisymmetric analyses, reaction forces and displacements in the z and radial directions can be obtained and used to calculate G_I and G_{II}, respectively. In the three dimensional analyses of this thesis, reaction forces and displacements in the z, radial, and tangential directions can be obtained and used to calculate G_I, G_{II}, and G_{III}, respectively. Zhao and Wang [17] used virtual crack closure to analyze mode III crack behavior in laminated composites. They adapted MCCM to obtain energy release rate results in a three-dimensional representation using the following formulae [17],

$$\begin{aligned} G_I &= -\frac{1}{2\Delta x\Delta y}\left[F_{zi}(w_j - w_{j'})\right] \\ G_{II} &= -\frac{1}{2\Delta x\Delta y}\left[F_{yi}(v_j - v_{j'})\right] \\ G_{III} &= -\frac{1}{2\Delta x\Delta y}\left[F_{xi}(u_j - u_{j'})\right] \end{aligned} \tag{2.18}$$

where Δx and Δy indicate the incremental crack area, F_{xi}, F_{yi}, and F_{zi} are the nodal forces at a crack front node i in the x, y and z directions respectively, and (u_j-$u_{j'}$), (v_j-$v_{j'}$), and (w_j-$w_{j'}$) are the relative displacements an element away from the crack front at the node pair j and j' in the x, y, and z directions respectively. The three modes of energy release rates can then add together to form G_{total}.

$$G_{total} = G_I + G_{II} + G_{III} \tag{2.19}$$

The MCCM used in this thesis stems from Zhao and Wang's technique, but has been adjusted to radial and tangential coordinates. Thus the equations for energy release rates become:

$$\begin{aligned} G_I &= G_z = \frac{1}{2\Delta A}\left[F_{iz}(z_{ifinal} - z_{iinitial})\right] \\ G_{II} &= G_{radial} = \frac{1}{2\Delta A}\left[F_{iradial}(u_{ifinal} - u_{iinitial})\right] \\ G_{III} &= G_{tangential} = \frac{1}{2\Delta A}\left[F_{itheta}(v_{ifinal} - v_{iinitial})\right] \end{aligned} \tag{2.20}$$

where u_i, v_i, and z_i are the radial, tangential, and vertical components of displacement.

This study also expands Rybicki and Kanninenn's MCCM to two analyses for some cases. The first analysis phase queries reaction forces at the crack tip and the second analysis phase extends the crack a distance Δa and then retrieves the displacements from the same nodes that were queried for reaction forces in the first analysis. Although lengthier, this approach ensures greater accuracy because it uses results obtained from the same location in the field.

2.3.4 J-Integral method

The J-integral is often used to characterize the energy release associated with crack growth. The original development of the J-integral method is attributed to J.R. Rice [15]. In a linear elastic analysis, the J-integral is equivalent to the energy release rate, G. The J-integral calculation combines the idea of virtual crack advance of the crack closure method with a strain energy approximation, thus making the J-integral a robust calculation. Onset of cracking is analyzed in ABAQUS by means of contour integrals [18]. Contour integral evaluations are possible at any location along a crack front. Each evaluation can be thought of as the virtual motion of a block of material surrounding the crack tip. Each block is defined by contours, or rings of elements completely surrounding the crack tip. The nodes defining the crack tip are specified by the user, and ABAQUS then finds the surrounding elements that form each contour ring. Results at each contour ring provide an estimate of the contour integral. Thus, the number of possible evaluations is the number of contours, which can be specified by using the CONTOURS parameter on the *CONTOUR INTEGRAL option. Figure 2.5 illustrates a typical mesh for J-integral evaluation.

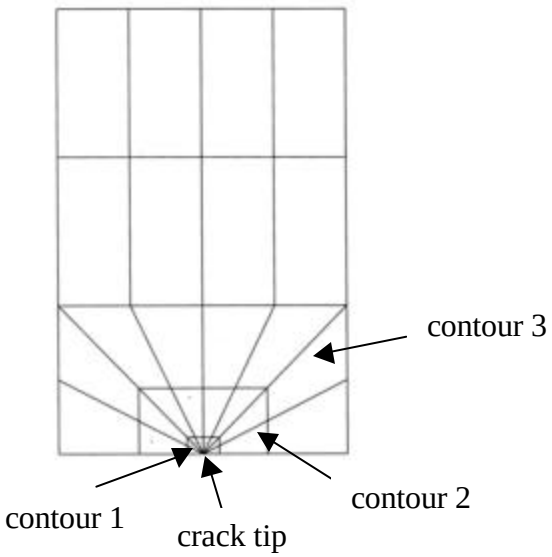

Figure 2.5. Typical 2-D J-integral meshing scheme (Courtesy of ABAQUS, Inc. [18])

The contour integrals in ABAQUS are evaluated using a domain integral method. This method expands the contour integral into an area integral in two dimensions or a volume integral in three dimensions, over a finite domain surrounding the crack front. Since the integral is taken over rings of elements radiating outwards from the crack tip, the crack tip singularity has less effect on energy quantities such as the J-integral.

The J-integral in ABAQUS is as follows [18],

$$\bar{J} = \int_A l\ (s) n \cdot H \cdot q dA \tag{2.21}$$

where dA is a surface element along a vanishing small tubular surface enclosing the crack tip, n is the outward normal to dA, and q is the local direction of virtual crack advance. H is given by

$$H = \left(WI - s \cdot \frac{du}{dx} \right) \tag{2.22}$$

where W is the elastic strain energy for elastic material behavior and I is the identity matrix. The J-integral estimates from different contours may vary due to the approximate nature of finite elements. However, large variations of J between contours indicate that mesh refinement is needed.

The pre-processor graphical user interface of ABAQUS, ABAQUS/CAE, is not equipped to fully handle fracture mechanics problems. Hence, the development of models requires

significant use of a text editor and ABAQUS/Standard code to build the input file. For two-dimensional models, only one node set must be provided to define the crack tip. For three-dimensional cases, a node set must be given for each node along the crack front. These nodes must be given in order from one end of the crack to the other, and must include the mid-side nodes of second order elements. The direction of virtual crack propagation must also be specified. Symmetry may be invoked in cases where the crack front is defined on a symmetry plane. This doubles the change in potential energy calculated from virtual crack front advance so as to correct the contour integral values. Sharp cracks can be modeled using small strain assumptions. A focused mesh with a crack-tip strain singularity should be used for the fracture mechanics evaluation. A linear elastic material mesh should exhibit a square root singularity.

In a two-dimensional model, the crack tip is modeled with a ring of collapsed quadrilateral elements. One side of each of the elements surrounding the crack tip should be collapsed so that all three nodes, 2 corner nodes and 1 mid-side node, share the same geometric position in space. The midside nodes of the sides connected to the crack tip are then moved to the ¼ point nearest the crack tip. This can be accomplished in ABAQUS by using the SINGULAR parameter on the *NFILL option with second-order isoparametric elements. Finally, to finish the square root singularity, the nodes of the collapsed side are constrained to move together using an *EQUATION or *MPC.

In a three-dimensional model, the method is repeated except a plane of a quadratic brick is collapsed. The same rules apply to create a square root singularity; midside nodes of elements at the crack tip are moved to the ¼ points and the nodes of the collapsed face are constrained to move together.

Kim and Lee [20] used the J-integral analysis in ABAQUS to obtain stress intensity factors of an oblique edge crack subjected to normal and shear tractions. Using seven contours, they achieved results to within 5% of analytical results.

Y. Cao [21] used the J-integral method in ABAQUS for three-dimensional modeling of a subsurface median crack in trilayer sandwiches. Cao used a special block of elements to capture the crack front, which required re-meshing at each step when the crack front moved. The cracked block contains singular elements at the crack tip with mid-side nodes moved to the ¼ point. The remainder of the structure maintained the same mesh

scheme throughout the analysis. With each new iteration, the cracked block with a modified crack front was reassembled into the rest of the structure. Using a three contour evaluation, Cao correlated *SIF's* derived from J-integral results to within 3% of results achieved with a modified displacement FE method, and to within 5% of theoretical results.

The two-dimensional J-integral analyses contained within this thesis follow the same procedure as Cao's work. A revised block of mesh containing singular elements with mid-side nodes moved to the ¼ point was reassembled into a standard mesh created in CAE with each increment of crack propagation. This is represented in Figure 2.6.

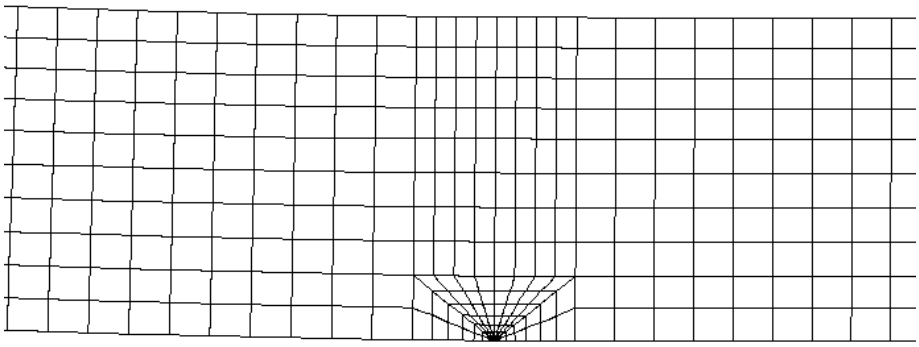

Figure 2.6. Sample mesh scheme for J-integral blister analyses

Sample code for the J-integral analysis of pressurized blisters can be found in Appendix A. The appendix does not include node and element specification for the standard mesh created in CAE due to the amount of space it would require.

Since the J-integral evaluation requires direct specification of the direction of crack propagation, the J-integral approach only yields a single G value. Therefore it would require significant analysis time to produce G_I, G_{II}, and G_{III} values.

2.4 Chapter summary

This chapter has reviewed the early developments of fracture mechanics and has sought understanding of the driving principles. The two main fracture parameters, stress intensity factor, K, and energy release rate, G, have been developed. From these concepts, general analytical development of energy release rates for fracture mechanics problems was possible. Finite element fracture mechanics methodologies for obtaining

energy release rates were then reviewed and developed. The following chapter concerns the choice of element type for these finite element fracture methodologies.

Chapter 3 Element Selection

3.1 Overview

Element selection in finite element models is based on many factors, beginning with how the physics of the problem change with spatial dimensionality. The range of spatial dimensionality in finite element analyses can be divided into four categories. The following list presents these categories in order of increasing complexity:

- One dimensional
- Two dimensional
- Axisymmetric
- Three dimensional

A general rule of thumb in the finite element world is to try to use the simplest representation possible without sacrificing accuracy of results. The complexity of the geometry and loading inherent in blister testing immediately eliminates any hope for the use of one-dimensional or two-dimensional geometry. Therefore, the discussion of element selection will be limited to axisymmetric and three-dimensional elements. The axisymmetric and three-dimensional elements used in this analysis occupy two separate element families; the structural element family and the solid-continuum element family. The following sections discuss the selection criteria for elements in each family.

3.2 Structural elements

Structural elements are used in finite element analyses to model 3-D problems with 2-D shells or 1-D beams. This simplification reduces the computing cost of modeling in exchange for a more complicated approximate theory. Structural elements can be very advantageous when used in proper applications. The attractiveness of modeling with structural elements led to the decision to use 3-D shell elements for initial modeling of the blister-type experiments.

Shells approximate a three-dimensional continuum with a two-dimensional, bi-axial state of stress. The reduction of dimensionality found in shell elements is achieved by taking advantage of the thinness of the shell. Shells are divided into two main categories, thick

and thin shells. Typically, thin shell theory applies when the shell thickness is less than 1/20 of the typical global shell dimensions. ABAQUS [22] bases its thin shell elements on Kirchoff's thin plate theory. Thin shells neglect transverse shear deformation and follow the Kirchoff constraint that the shell normal remains orthogonal to the shell mid-surface. Four and eight noded elements with five degrees of freedom per node and reduced integration (S4R5, S8R5) are recommended for 3-D thin shell application. Thick shell theory applies when the shell thickness is between 1/10 and 1/20 of the typical global shell dimensions. Thick shell element development in ABAQUS is based on Mindlin plate theory, which includes transverse shear effects. Hence, planes initially normal to the mid-surface are allowed to experience rotations different from the rotations of the mid-surface. ABAQUS recommends the use of four and eight noded elements with reduced integration and finite membrane strains (S4R, S8R) for 3-D thick shell applications. Solid continuum elements should be used when the thickness to span (h/a) ratio exceeds 1/10. The general rule of thumb is summed by the following :

thin shells <= h/a: 1/20 <= thick shells <= h/a: 1/10 <= bricks

At a thickness of 0.04 *mm*, this bracketing becomes,

bricks <= a=0.4 *mm* <= thick shells <= a=0.8 *mm* <= thin shells

At h=0.04 *mm* and with a 0.01 *mm* prescribed displacement, the max displacement to crack length ratio, w_0/a, bracketing is,

thin shells <= w_0/a=1/80 <= thick shells <= w_0/a=1/40 <= bricks

An analysis of the shaft-loaded blister test has been undertaken to determine the validity of shell elements based on the scale of problems seen in the models of this thesis. The geometry is indicated in Figure 3.1.

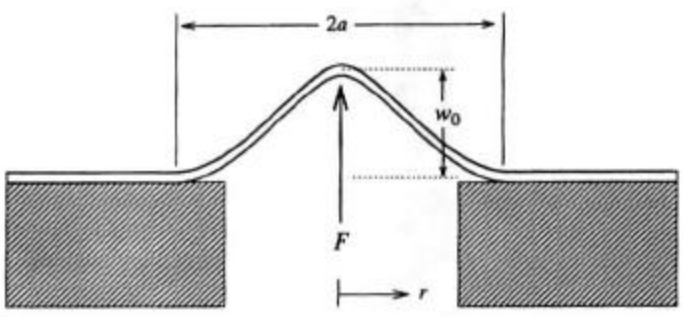

Figure 3.1. Geometry of shaft-loaded blister for shell element validation

Figure 3.2 compares the effect of element choice on displacement profiles of a shaft-loaded blister at a debond radius of 1.99 *mm*, $h/a \approx 1/50$. Loading is applied by prescribing a 0.01 *mm* displacement at the center of the blister. This results in a w_0/a, of 1/20=0.005. Data from all finite element cases is taken from the mid-surface of the models since shell theory assumes only mid-surface deflections.

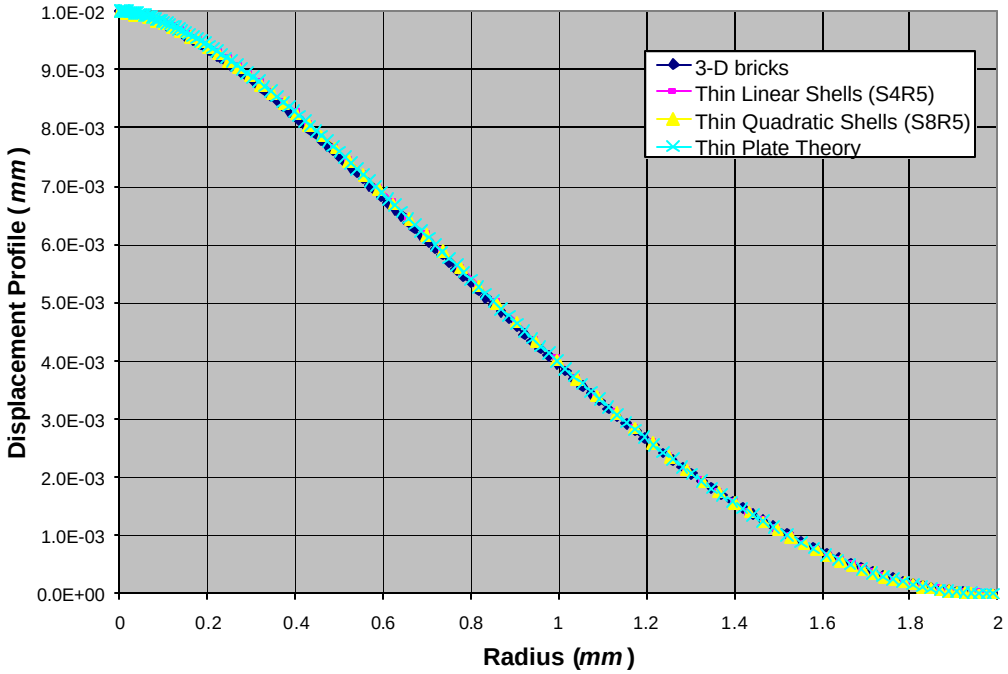

Figure 3.2 Thin shell/brick element comparison at 1.99 *mm* debond radius

It is evident in Figure 3.2 that there is little difference in deflection profiles between shell elements, brick elements, and thin plate theory [31] at an *h/a* of approximately 1/50, as would be expected according to the rule of thumb presented earlier. Table 3.1 presents a quantitative assessment of the performance of the shell elements compared to the 3-D brick elements. Error is defined as the converged transverse deflection of the mid-surface of the shell models relative to the converged transverse deflection of the mid-surface of the 3-D model, calculated as,

$$error = w_{3-D} - w_{thinshell} \tag{3.1}$$

The analysis includes calculation of standard deviations and signal-to-noise ratios. Standard deviation, s_x, is the square root of the variance, s_x^2, of the data over the entire displacement profile of the blister,

$$\hat{s}_x = \sqrt{\frac{\sum (error - meanerror)^2}{n-1}} \tag{3.2}$$

$$\hat{s}_x^2 = \frac{\sum (error - meanerror)^2}{n-1} \tag{3.3}$$

where n is the number of data points analyzed. The signal-to-noise ratio, *SNR*, gives an indication of the error over the entire blister relative to the maximum displacement. The SNR is defined as the maximum signal divided by the standard deviation,

$$SNR = \frac{w_0}{\hat{s}_x} \tag{3.4}$$

Table 3.1. Statistical data for element comparison at 1.99mm debond radius, w_o =0.01mm

	Thin linear shells (S4R5)	**Thin quadratic shells (S8R5)**
Variance	1.18E-09	1.09E-09
Standard Deviation	3.44E-05	3.30E-05
Signal-to-Noise Ratio	290.6	303.2

Table 3.1 indicates that both the linear and quadratic thin shell results correspond highly to the 3-D brick results. The thin quadratic shell results are in slightly better agreement with the 3-D brick results.

Moving into the thick shell region, Figure 3.3 compares thin shell elements, thick shell elements and brick elements for the case of a shaft-loaded blister at a debond radius of 0.49 *mm*, $h/a \approx 2/25$, with a prescribed 0.01 *mm* displacement at the center of the blister. This results in a $w_0/a = 1/50 = 0.02$.

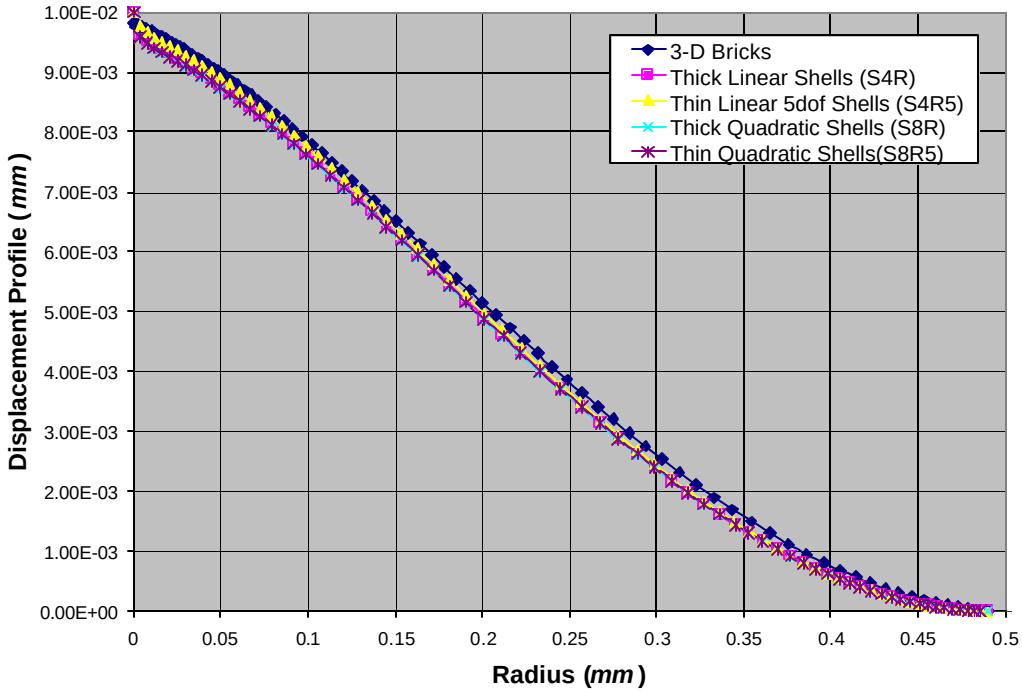

Figure 3.3. Thin shell/thick shell/brick element comparison at 0.49 *mm* debond radius

Figure 3.3 indicates that the "thick shell" elements perform no better than "thin shell" elements at 0.49 *mm* debond radius. All four shell element types slightly undershoot the mechanics captured in 3-D solid-continuum representation. Table 3.2 provides a statistical analysis of the shell element curves in Figure 3.3 against 3-D brick elements.

Table 3.2. Statistical data for element comparison at 0.49mm debond radius, w_o =0.01mm

	Thick linear shell (S4R)	Thin Linear 5dof shell (S4R5)	Thick quadratic shell (S8R)	Thin quadratic shell (S8R5)
Variance	5.82E-09	8.99E-09	7.78E-09	6.50E-09
Standard Deviation	7.63E-05	9.48E-05	8.82E-05	8.06E-05
Signal-to-Noise Ratio	131.1	105.5	113.4	124.0

Table 3.2 indicates that the results of thick and thin shell elements are comparable. Thick linear shells (S4R) perform the best, but overall, the SNR's are at most 45% of the SNR's calculated for the 1.99 *mm* debond radius case. These results indicate that the performance of shell elements is beginning to be compromised as the length of debond radius is decreased. This compromise is magnified as the thickness to span ratio transitions into the brick element regime.

Figure 3.4 illustrates the failure of shell elements for a shaft-loaded blister at a debond radius of 0.09 *mm*, $h/a \approx 2/5$, with a prescribed 0.01 *mm* displacement at the center of the blister. This results in a $w_0/a \approx 1/10 = 0.1$.

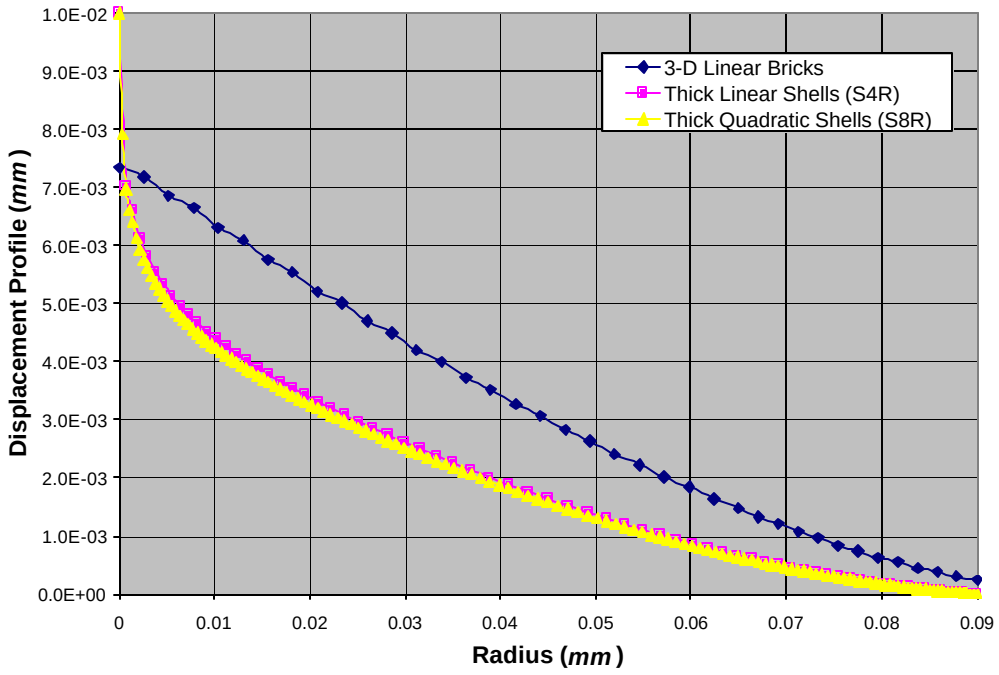

Figure 3.4. Thin shell/brick element comparison at a 0.09 *mm* debond radius

Figure 3.4 clearly indicates the failure of shell elements in capturing the transverse shear deformation present in the 0.09 *mm* debond radius model. The 3-D solid continuum model experiences high compressive strains at the blister center, thereby reducing the mid-surface's center deflection. The physics inherent in shell theory does not allow for this change in deflection because the mid-surface is analytically forced to the prescribed displacement. Table 3.3 gives the statistical comparison of the thick shell elements to the 3-D solid brick elements.

Table 3.3. Statistical data for element comparison at 0.09mm debond radius, w_o=0.01mm

	Thick linear shells (S4R)	Thick quadratic shells (S8R)
Variance	3.82E-07	4.29E-07
Standard Deviation	6.18E-04	6.55E-04
Signal-to-Noise Ratio	16.2	15.3

The SNR's for the thick shell elements of Table 3.3 indicate extremely low correlation to the 3-D brick element models. The difference between using linear or quadratic

interpolation is insignificant. Combined, Figure 3.4 and Table 3.3 provide evidence of the need for solid continuum representation for debonds resulting in $h/a>1/10$, $w_0/a=>1/40$.

The results of this analysis of structural elements indicate that caution must be used when applying shell element models to fracture of thin film systems. Shell elements fail to capture the correct deformation mechanics when applied outside their recommended limitations. Initial experimental results of the target geometry of this thesis indicate that the maximum debond radius for the probe loaded thin film/substrate system is about 0.4 to 0.5 *mm*. Based on the above analysis, this geometry scale falls outside the recommended limitations of shell elements. Therefore all remaining finite element analyses are based on solid continuum elements, which are described in detail in Section 3.3.

3.3 Solid continuum elements

Solid continuum elements are the building blocks of finite element analysis. Solid continuum element theory makes the least amount of assumptions on the deformation mechanics. For small deformations, the three-dimensional continuum element deformation mechanics are exact. However, element selection for solid continua is no easier than element selection for more complicated model theories. The wide variety of elements available for solid continua makes it important to tailor element selection to the problem at hand. The solid element library in ABAQUS includes first order, linear interpolation elements and second order, quadratic interpolation elements. Continuum elements come in the form of triangles and quadrilaterals in two dimensions / axisymmetry, and tetrahedra, triangular prisms, and bricks in three-dimensions. Any of these elements' stiffness matrices can be computed using either full or reduced integration methods. The following comparisons are based on the solid element discussion of the ABAQUS/Standard User's Manual, Volume II [23], and Cook [24].

3.3.1 Order of interpolation

Displacements and other degrees of freedom are only calculated at the nodes of an element. Displacements at any other point in the element are obtained by interpolating from these nodal displacements. For isoparametric elements, the interpolation order is determined by the number of nodes used in the element. For example, an element with only corner nodes such as an 8-noded brick (C3D8, shown in Figure 3.5a) uses linear interpolation in each direction, and hence are often called linear or first-order elements. Elements with mid-side nodes such as 20-noded bricks (C3D20, shown in Figure 3.5b) use quadratic interpolation and are often called quadratic or second-order elements.

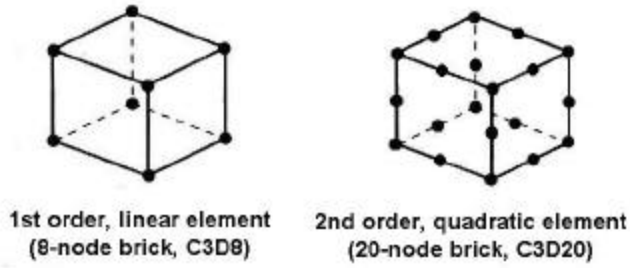

Figure 3.5 Linear and quadratic brick elements (Courtesy of ABAQUS, Inc. [23])

Second-order elements generally provide higher accuracy than first-order elements for problems that don't involve complex situations such as contact, impact, or severe distortion. Second-order meshes are able to capture geometric features such as curves with fewer elements than first-order meshes, and also outperform first-order meshes in stress concentration and fracture mechanics problems. Perhaps the greatest advantage of second-order elements over first-order elements is their effectiveness in bending-dominated problems, which is a result of their ability to represent high stress gradients and curved geometries.

First-order elements typically provide better performance in impact and contact situations, or where kinematic discontinuities exist because they are less sensitive to distortion than second-order elements. Bending behavior in first-order elements can be improved by adding incompatible deformation modes to the standard displacement degrees of freedom. The effect of these modes is to add internal degrees of freedom,

which eliminate both the parasitic shear stresses that contribute to stiffness in bending, and the artificial stiffening due to Poisson's effect in bending.

3.3.2 Triangle/tetrahedra vs. quadrilateral/bricks

In general, triangles/tetrahedra are to be avoided unless needed to capture complex geometries. First order triangles/tetrahedra are overly stiff, requiring extremely fine meshes to obtain accurate solutions, thus making them very uneconomical. Typically, a good mesh of quadrilaterals/bricks usually provides a more accurate solution at far less cost. Quadrilaterals/bricks have a better rate of convergence and are less sensitive to mesh orientation than triangular/tetrahedral elements, which facilitates ease of meshing.

3.3.3 Integration

ABAQUS uses numerical techniques to integrate various output quantities over the volume of each element. The material response is evaluated at each integration point in an element using Gauss Legendre quadrature. When using continuum elements, a choice must be made whether to use full or reduced integration. Gauss quadrature can best be explained in one-dimension. Gauss quadrature evaluates an integral of a function as the sum of a finite number of terms [24]:

$$I = \int_{-1}^{1} f\,dx \quad \longrightarrow \quad I \approx \sum_{i=1}^{n} W_i f_i \tag{3.5}$$

where W_i is a weight, and f_i is the value of $f=f(x)$ at a location called a "Gauss" point. The order of Gauss quadrature is based on the number of Gauss points used to approximate the integral. If $f=f(x)$ is a polynomial, n-point Gauss quadrature yields the exact integral if f is of degree (2n-1) or less. For example, if f=a+bx, the integral is exactly integrated by a one-point Gauss rule. Use of more than one point for this case still yields the exact result but requires greater computation. If f is not a polynomial, Gauss quadrature yields an approximate result, whose accuracy improves with increasing the number of Gauss points.

In two-dimensions, integration is performed over a quadrilateral and a Gauss rule of order n uses n^2 points. Likewise, in three dimensions, Gauss quadrature of order n is performed over a hexahedron using n^3 points. It would seem that using many Gauss points would

lead to improved accuracy, however that is not always the case. Finite element solutions are approximations, and usually err by being too stiff due to constraints imposed by the form of the assumed displacement field. Overstiffness is usually made worse by using more Gauss points, or full integration, because the additional points capture higher-order terms in the stiffness matrix. These higher-order terms resist some deformation modes that lower-order terms do not, hence stiffening the model. Although this results in greater accuracy in evaluating the integral used to compute the stiffness matrix, it establishes a more accurate evaluation of an assumed, but approximate representation of true stiffness. This can often lead to less accuracy in the result.

Fully integrated elements may suffer from both shear and volumetric locking. Shear locking occurs in first-order fully integrated elements subjected to bending. The numerical formulation of the elements gives rise to parasitic shears that really do not exist and cause the element to become too stiff in bending. Second-order elements do not suffer from shear locking because their quadratic interpolation function allows them to better represent the displacement fields associated with bending. Volumetric locking may also occur in a fully integrated mesh whose material behavior is nearly incompressible. An incompressible material requires that the volume at each integration point remain fixed, which puts severe constraints on the kinematic displacement field. Basically, the number of degrees of freedom of the element becomes less than the number of constraints, thereby "locking" the mesh. Volumetric locking can be eliminated by using reduced integration elements or hybrid element formulations. Hybrid element formulations impose incompressibility constraints on each element in an average sense by a Lagrange multiplier technique. Hybrid elements require greater computational cost due to the introduction of the Lagrange multipliers. Therefore hybrid elements should only be used when necessary, for example, in first-order meshes with strictly incompressible material behavior, or in second-order meshes with nearly incompressible material behavior.

On the other hand, using too few Gauss points, or reduced integration, may cause element instabilities and mesh distortion. A common instability caused by reduced integration in first order elements is called hourglassing. First order reduced integration elements have only one integration point and thus it is possible for them to distort in such a way that the

strains calculated at the integration point are all zero, which leads to uncontrolled deformation of the mesh. Second-order element meshes do not suffer from hourglassing because neighboring elements cannot share the mode. It is impossible for two adjacent second-order elements to both display this mode while remaining connected, and thus the effect is non-propagating. Geometrically linear problems are not susceptible to hourglass inaccuracy effects. However, in geometrically non-linear problems, hourglass modes interact with strains at the integration points which leads to inaccuracy and instability. Fortunately, a commercial code such as ABAQUS is designed so that the smallest necessary number of Gauss points are used, without reaching instability. If fewer points are used, stabilization methods such as hourglass control are invoked to prevent instability.

Overall, reduced integration reduces running time and yields more accurate results in second-order elements. However, the accuracy achieved with full versus reduced integration in first-order elements is highly dependent upon the nature of the problem, and its susceptibility to instabilities. The following section highlights the key properties and attributes of each element type.

3.4 Element comparison (axisymmetric, 3-D) [23,24]

First order Triangles and Tetrahedron (CAX3,C3D4)

- Usually overly stiff
- Very poor convergence rate
- Extremely fine meshes required to obtain accurate results
- Mesh orientation has significant influence on accuracy.
- Only useful as filler elements in non-critical areas

First order Fully Integrated Quads and Bricks (CAX4,C3D8)

- Tend to be overly stiff in bending due to parasitic shear, shear locking
- Immune to hourglassing
- Use selectively reduced-integration procedure to model nearly incompressible materials
- Fully incompressible material models should be modeled with hybrid elements

First order Reduced Integration Quads and Bricks (CAX4R,C3D8R)

- Very economical and perform well

- Effective with nearly incompressible materials, but require hybrid formulation for fully incompressible materials
- Susceptible to hourglassing and other instabilities when highly distorted such that a Gauss point senses no strain and the stiffness matrix has no resistance

Second order Triangles and Tetrahedron (CAX6,C3D10)

- Suitable for general use
- Sensitive to mesh orientation
- Useful in contact problems and with incompressible materials
- Should be used only when geometry demands its use

Second Order Fully Integrated Quads and Bricks (CAX8,C3D20)

- Excellent general purpose elements
- High accuracy in problems that don't involve contact, impact, or severe distortion
- Very effective in bending dominated problems
- Effective with stress concentrations and fracture mechanics problems
- Hybrids should be used with nearly or fully incompressible materials

Second Order Reduced Integrated Quads and Bricks (CAX8R,C3D20R)

- Super convergence provides high accuracy
- Very economical due to the smaller number of integration points
- Hybrids only needed in fully incompressible material models
- Quads have only 1, non-communicable, hourglass mode and therefore hourglass control is not needed
- Bricks have 6 hourglass modes that are non-propagating as long as mesh has two or more elements in at least two directions

Neglecting triangle and tetrahedra elements, the following section performs an axisymmetric test case of the pressurized blister test to determine what element type is most suitable for the models in this thesis.

3.5 Axisymmetric test case

In order to select the most suitable element type, an experiment based on axisymmetric models of pressurized blisters has been developed. The experiment's selection criteria is based on energy release rate results using the change in strain energy and crack closure methods. The experiment does not apply to the J-integral approach to determining energy release rates because the J-integral method requires meshes of second order isoparametric elements in order to capture the singularity at the crack tip, as described in

Section 3.3.4. The experiment assumes a Young's Modulus of E=3400 *MPa*, Poisson's ratio of n=0.32, film thickness of h=0.04 *mm*, and a pressure of 0.006895 *MPa*. A schematic of the pressurized blister test is presented in Figure 3.7.

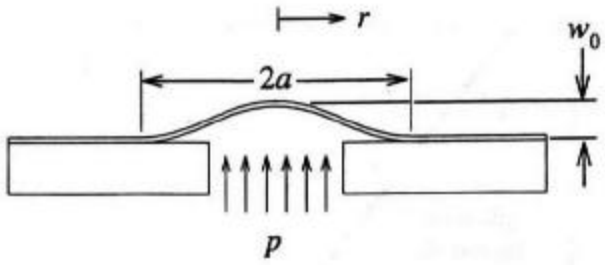

Figure 3.6. Pressurized blister test used for element selection

Three models with varying blister radii in thin plate theory range were queried for total energy release rates, G_{total}, using both the modified crack closure method (MCCM) and change in strain energy method (STR). For convenience, the MCCM will be referred to as CC for the remainder of the work. The level of meshing is consistent in all analyses. Goals for each mesh type tested were for the energy release rates of the two theories to match, and for these results to correlate with thin plate theory (TP). Percent errors are defined with respect to theory; and between the two finite element methods, with respect to change in strain energy approach. For example,

$$\%error = 100 \times \frac{abs(G_{TP} - G_{STR})}{G_{TP}} \tag{3.6}$$

Table 3.4 displays the results of the comparison test. The thin plate (TP) G_{total} values for the 2*mm* debond vary because they are based on the maximum central deflection of the midplanes of the blisters.

Table 3.4. Element comparison for axisymmetric pressurized blister test (thin plate region)

Case	Element type	# Elements	G_{total} (kJ/m^2) STR	CC	TP	Percent Erorrs (%) CC to STR	STR to TP	CC to TP
0.5*mm* debond								
h/a =2/25	linear, full int (CAX4)	3454	1.40E-06	1.41E-06	1.34E-06	0.32	4.68	5.02
	quadratic, full int (CAX8)	3454	1.40E-06	1.08E-06	1.34E-06	22.70	4.52	19.21
1*mm* debond								
h/a =1/25	linear, full int (CAX4)	4840	2.01E-05	1.93E-05	1.97E-05	3.81	2.01	1.88
	quadratic, full int (CAX8)	4840	2.01E-05	1.53E-05	1.97E-05	23.97	2.12	22.36
2*mm* debond								
h/a =1/50	linear, full int (CAX4)	6580	3.07E-04	2.94E-04	3.03E-04	4.35	1.31	3.10
	linear, incompat modes (CAX4I)	6580	3.07E-04	2.92E-04	3.04E-04	4.99	1.01	4.04
	linear, red. int (CAX4R)	6580	3.08E-04	2.97E-04	3.05E-04	3.65	0.98	2.71
	quadratic, full int (CAX8)	6580	3.08E-04	2.30E-04	3.04E-04	25.35	1.28	24.40
	quadratic, red int (CAX8R)	6580	3.08E-04	2.27E-04	3.04E-04	26.49	1.29	25.54

From the STR to TP percent error column of Table 3.4, it is evident that switching from linear interpolation elements to quadratic interpolation elements has negligible effect on G_{total} values resulting from the change in strain energy method. However, G_{total} results using crack closure are significantly impacted by element choice as can be seen in the difference in results in the CC to TP column between element types. Analyses with linear elements provide correlation for crack closure to change in strain energy (CC to STR) to within 5% difference for all debond lengths. Adherence to thin plate theory (CC to TP and STR to TP) also remains equal to or less than 5% difference for analyses using linear elements. Analyses with quadratic interpolation meshes on the other hand, experience approximately 20-25% error between crack closure and change in strain energy (CC to STR), and crack closure and thin plate theory (CC to TP). These findings are consistent with experiments done by Rybicki and Kanninen [14], who found that poor results were obtained when crack closure was used with higher order elements. Possible reasoning for the failure of the second-order elements is that the crack-closure method involves releasing one node from the adhered surface, and thus this location is a singularity. The node at this location undergoes severe distortion, which is detrimental to second-order elements, as noted in Section 3.3.1.

Zeroing in on the different types of first-order meshes tried on the 2 *mm* debond radius model in Table 3.4, it becomes evident that reduced integration produces slightly more accurate results than full integration or incompatible modes. Analysis of the data used in computing crack closure indicates that the fully integrated and incompatible mode meshes were too stiff, resulting in low displacements. This increased stiffness could be due to shear locking in the fully integrated meshes.

Having established that first-order reduced integration elements (CAX4R) best capture energy release rates in the thin plate region for the change in strain energy and crack closure methods, the question arises as to whether this holds true at smaller radii where the models approach infinite medium behavior ($h \to \infty$). To address this issue, another element comparison was conducted at a 0.0067 *mm* debond radius much like Table 3.4, but representative of the infinite medium (IM) geometry. Table 3.5 presents the data from this comparison.

Table 3.5. Element comparison for axisymmetric pressurized blister test (infinite medium)

			G_{total} (*kJ/m*^{2})			Percent Erorrs (%)		
Case	**Element type**	**# Elements**	**STR**	**CC**	**IM**	**CC to STR**	**STR to IM**	**CC to IM**
0.0067*mm* debond								
h/a=6.0	linear, red int (CAX4R)	9196	5.20E-11	4.54E-11	5.13E-11	12.85	1.50	11.54
	linear, full int (CAX4)	9196	5.16E-11	4.71E-11	5.29E-11	8.65	2.59	11.01
	quadratic, full int (CAX8)	9196	5.17E-11	4.52E-11	5.17E-11	12.46	0.05	12.41
	quadratic, red int (CAX8R)	9196	5.17E-11	3.38E-11	5.17E-11	34.66	0.05	34.63

Looking at the percent errors listed in the STR to IM column of Table 3.5, it is evident that all element meshes provide excellent correlation of G_{total} results for the change in strain energy method. However, the CC to IM column indicates that the crack closure method fails to produce accuracy better than 11%. Even so, the linear meshes still outperform quadratic meshes using the crack closure method. The deviance of the crack closure results from theory is caused by the inability of the finite element solution to accurately reproduce the singularity that exists at the change in boundary conditions for such a small crack length. Extensive mesh refinement would improve results, but as for element selection, the data of Table 3.5 is insufficient to warrant switching from first-order to second-order element meshes.

Overall element behavior in 3-D solid continua is no different than element behavior in axisymmetric solid continua, thereby making it safe to assume that first order, reduced integration bricks (C3D8R) will best capture energy release rates in 3-D models. Table 3.6 compares results of 3-D solid continua elements to the results of the axisymmetric solid continua elements.

Table 3.6. Element comparison for axisymmetric and 3D pressurized blister test (infinite medium)

			G_{total} (kJ/m^2)			Percent Erorrs (%)		
Case	Element type	# Elements	STR	CC	IM	CC to STR	STR to IM	CC to IM
0.0067*mm* debond								
h/a=6.0								
AXI	linear, red int (CAX4R)	9196	5.20E-11	4.54E-11	5.13E-11	12.85	1.50	11.54
AXI	linear, full int (CAX4)	9196	5.16E-11	4.71E-11	5.29E-11	8.65	2.59	11.01
3D	linear, red int (C3D8R)	67100	5.23E-11	5.23E-11	5.17E-11	0.001	1.34	1.34

Column STR to IM in Table 3.6 demonstrates that energy release rates based on the change in strain energy method do not change between axisymmetric and fully 3-D models. However, columns CC to IM and CC to STR show that the crack closure method from the analysis with 3-D elements produces a solution that is in good agreement with both theory and the change in strain energy method. This result validates the use of first order, reduced integration elements for 3-D solid continua crack closure analyses. Table 3.6 also proves that increasing the dimensionality of the model from axisymmetric analysis to 3-D analysis improves the accuracy of the crack closure method for models representative of semi-infinite mediums, a=small. This improvement could possibly be due to the fact that a 3-D analysis discretizes the blister about it's circumference, thereby providing an additional dimension. This allows estimates of internal energy in the model to be more localized, whereas an axisymmetric analysis averages the internal energy about the circumference. Since crack closure captures a local effect, the 3-D analysis is therefore able to provide a more accurate representation.

3.6 Chapter summary

This chapter began by demonstrating the limitations of structural elements in modeling thin films at the geometry scale of this thesis. These limitations instigated a move towards the use of solid continua elements rather than structural elements. The next section discussed the advantages and disadvantages of element order of interpolation,

element shape, and element degree of integration. The pros and cons of the various element types in ABAQUS were then highlighted in a small summary. To determine an element type suitable for the geometry of this thesis, an axisymmetric test case of the pressurized blister test was developed. For blisters with large debond lengths, first-order, reduced integration, quadrilateral elements produced the most accurate energy release rates using the crack closure and change in strain energy methods. Results from analyses of the blister at a small debond length were not sufficient to warrant any change in element choice, although no choice of element type gave accurate results with the crack closure method. First order, reduced integration, brick elements were then used in a three-dimensional model of the pressurized blister test. The 3-D elements produced excellent results with both the change in strain energy and crack closure approaches. This result proved that increasing the dimensionality of the model within the analysis corrected the problem of obtaining accurate energy release rates with the crack closure method at small debond lengths. The following chapter introduces and fully examines the pressurized blister test.

Chapter 4 Verification Model: Pressurized Blister Test

4.1 Verification

In order to validate the results obtained in the finite element analysis, classical analytical solutions to delaminating thin films have been investigated. The purpose of analytical solutions is three-fold: first they provide an independent approximation to the problem of interest. This ensures an understanding of the mechanics as well as an appreciation for the relative orders of magnitude of problem parameters. Secondly, the classical solutions verify that we have modeled the problem correctly, thereby giving confidence in the solution for the probe loaded edge interface. Finally, the classical solutions create an environment in which the different means of determining energy release rates can be compared. This chapter explores the classical solution of the pressurized blister test, and Chapter 5 investigates a variant of the pressurized blister test, the shaft-loaded blister test. Both blister tests represent out-of-plane loading of thin films and therefore provide good preliminary approximations to the probe test.

4.2 Overview

The first means of verifying both the mechanics of the finite element model and the energy release rate methodology is the pressurized blister test. The pressurized blister test consists of a thin circular film adhered to a rigid substrate, except for a central portion of radius a. When the central non-adhered portion is pressurized, the film lifts off the substrate, forming a blister. The blister radius remains fixed until a critical pressure, p_{cr}, is reached. At this pressure, the blister increases in size, indicating adhesive failure along the interface. Blister test behavior can be bounded by two extreme theoretical cases: thin plate theory associated with relatively large blister debond lengths and semi-infinite medium theory associated with very small blister debond lengths.

There are four objectives behind the finite element analysis of the pressurized blister test.

1. Accurately model the bounding extremes where thin plate and semi-infinite medium theory apply. This will allow for assessment of the ability of the finite element model

to successfully capture both the deformation mechanics and the available energy release rates. Verification of blister finite element results to theory provides a basis for developing an analysis of the probe-loaded geometry.

2. Experimentally show that increasing the debond length while holding the specimen thickness constant causes the behavior of the model to transition between the two limiting cases of a semi-infinite medium and a thin plate.
3. Determine the sensitivity of the blister test to residual stress. Thin films are generally highly sensitive to residual stresses caused by thermal strains induced by mismatched coefficients of thermal expansion between the film and substrate.
4. Calculate the mode-mixity of energy release rates of the blister, with and without residual stress. The mode-mixity gives insight into the mode of fracture that is dominating failure.

4.3 Pressurized blister theory

4.3.1 Thin plate

The limit case of thin plate theory in pressurized blisters can be physically represented by large debond lengths, a (mm), relative to specimen thickness, h (mm) (h/a=small). The pressurized blister test with thin plate geometry is depicted in Figure 4.1.

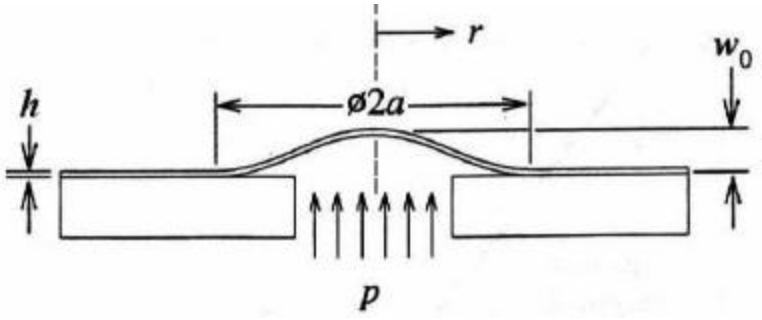

Figure 4.1. Schematic of a pressurized thin plate blister

The following analysis develops an expression for the strain energy release rate, G (J/m^2), for a pressurized blister in the limit case of thin plate theory. The analysis assumes linear elastic material properties, and small strain, small displacement theory, with no regard for residual stress.

The following development is based on the research of M.L. Williams [25], Anderson et al [26], Bennett et al [13], Jensen [27], Wan and Mai [28], J. G. Williams [29], Wan and

Lim [30] and on personal discussions with Wan [12]. Derivation of the energy release rate for a pressurized blister with thin plate theory begins with quantification of the elastic strain energy, $U_{elastic}$.

$$U_{elastic} = \int p dV \tag{4.1}$$

with p being the applied pressure (MPa), and V the volume (mm^3) under the deformed shape of the blister. The blister volume is obtained by integrating the profile displacement field, $w(r)$ (mm), about the blister circumference.

$$V = 2p \int_0^a w(r) r dr \tag{4.2}$$

Assuming linear elasticity, Timoshenko's clamped circular plate under uniform loading [25] provides the axisymmetric displacement field, $w(r)$,

$$w(r) = \frac{3p(a^2 - r^2)^2}{16E'h^3} \tag{4.3}$$

from which the central displacement w_o, can be derived,

$$w_0 = \frac{3pa^4}{16E'h^3} \tag{4.4}$$

with $E' = E/(1-\nu^2)$ (MPa), a is the debond radius (mm), r is the variable radius (mm), and h the specimen thickness (mm). Hence, the volume under the deflected blister is,

$$V = \frac{6pp}{16E'h^3} \int_0^a r(a^2 - r^2)^2 dr$$

$$V = \frac{ppa^6}{16E'h^3} \tag{4.5}$$

Rearranging Eq. (4.5) to solve for p and returning to Eq. (4.1), the elastic energy stored in the blister is

$$U_{elastic} = \int \frac{16E'h^3}{pa^6} V dV$$

$$U_{elastic} = \frac{1}{2} pV = \frac{pp^2a^6}{32E'h^3} \tag{4.6}$$

The strain energy release rate is the change in stored elastic strain energy with respect to change in area, dA, due to the creation of new surface areas by crack advance,

$$G = \frac{dU_{elastic}}{dA}$$

But $A=\pi a^2$ => $dA/da=2\pi a$ => $dA=2\pi a da$. This leads to

$$G = \frac{dU_{elastic}}{da}\frac{da}{dA} = \left(\frac{dU_{elastic}}{da}\right)\left(\frac{1}{2pa}\right) \tag{4.7}$$

Substituting Eq. (4.6) into Eq. (4.7) and differentiating yields,

$$G = \frac{3p^2a^4}{32E'h^3} \tag{4.8}$$

The available energy release rate, G, for a pressurized blister can be written in terms of the applied pressure and the maximum deflection at the center of the blister, Eq. (4.4), giving the simpler form, [29]

$$\boxed{G = \frac{pw_0}{2}} \tag{4.9}$$

4.3.2 Semi-infinite medium

The limit case of semi-infinite medium theory in pressurized blisters can be physically represented by small debond radii relative to specimen thickness (h/a=large), resulting in a half-space. The pressurized blister test with semi-infinite geometry is depicted in Figure 4.2.

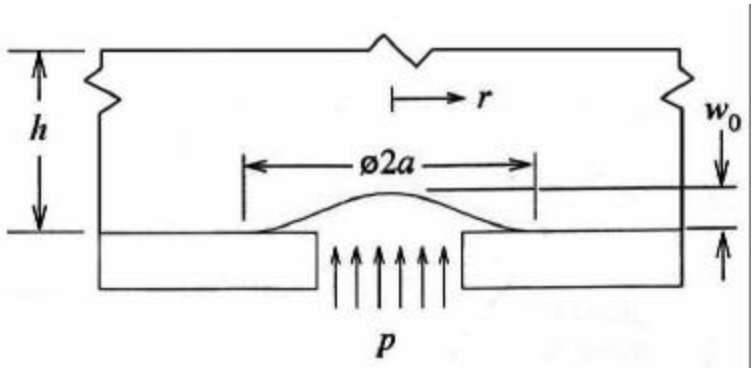

Figure 4.2. Schematic of a pressurized infinite medium blister

The analysis that follows develops an expression for the energy release rate, G (J/m^2), of a pressurized blister in the limit case of infinite medium theory. Again, the classic solution assumes linear elastic material properties, small strains, and small displacements, and the analysis occurs in the absence of residual stress.

Again, the following development is based on a solution by Mossakovskii and Rybka [31], Bennett et al [13], Anderson et al [26], and on personal discussions with Wan [12]. Derivation of the energy release rate for a pressurized blister with infinite medium theory begins with quantification of the elastic strain energy, $U_{elastic}$.

$$U_{elastic} = \int p dV \tag{4.10}$$

With p being the applied pressure (MPa), and V the volume (mm^3) under the deformed shape of the blister. The blister volume is obtained by integrating the displacement field, $w(r)$ (mm), about the blister circumference.

$$V = 2p \int_0^a w(r) r dr \tag{4.11}$$

Sneddon's analysis [32] provides the deflection, $w(r)$, of a pressure loaded penny-shaped crack between a semi-infinite medium and a rigid substrate with crack length a,

$$w(r) = \frac{4p(a^2 - r^2)^{1/2}}{pE'} \tag{4.12}$$

from which the central displacement, w_0, can be derived,

$$w_0 = \frac{4pa}{pE'} \tag{4.13}$$

with $E' = E/(1-\nu^2)$ (MPa), a is the debond radius (mm), r is the variable radius (mm), and h the specimen thickness (mm). Hence,

$$V = \frac{8pp}{pE'} \int_0^a r\sqrt{(a^2 - r^2)} dr$$

From Mathematica®

$$V = \frac{8pa^3}{3E'} \tag{4.14}$$

Rearranging Eq. (4.14) to solve for p and returning to Eq. (4.10), the elastic energy stored in the blister is

$$U_{elastic} = \int \frac{3E'}{8a^3} V dV$$

$$U_{elastic} = \frac{1}{2} pV = \frac{4p^2 a^3}{3E'} \tag{4.15}$$

The energy release rate, G, is the stored strain energy with respect to the change in area, dA, due to the creation of new surface areas by crack advance,

$$G = \frac{dU_{elastic}}{dA}$$

Again, $A=\pi a^2 \Rightarrow dA/da=2\pi a \Rightarrow dA=2\pi a da$. This leads to

$$G = \frac{dU_{elastic}}{da}\frac{da}{dA} = \left(\frac{dU_{elastic}}{da}\right)\left(\frac{1}{2pa}\right) \tag{4.16}$$

Substituting Eq. (4.15) into Eq. (4.16) yields,

$$G = \frac{2p^2 a}{pE'} \tag{4.17}$$

The available energy release rate, G, for a penny crack in a semi-infinite medium can be written in terms of the applied pressure and the maximum deflection at the center of the blister, Eq. (4.13), giving the simpler form, of Eq. (4.18).

$$\boxed{G = \frac{pw_0}{2}} \tag{4.18}$$

4.4 Finite element model development

Having established the theoretical limiting cases of the pressurized blister test, a design envelope has been established in which a finite element analysis can occur. The pressurized blister test has been modeled using both three-dimensional and axisymmetric finite element models. Axisymmetric models are fully capable of handling the blister test and are the standard of this analysis. However, three-dimensional models are also developed because the geometry of the edge-loaded model in Chapter 6 can only be captured by a three-dimensional representation. Three-dimensional linear elasticity with small deformations is exact and three-dimensional models impose no theoretical constraints beyond their linear or quadratic interpolation functions. Therefore three-dimensional models contain more modeling potential than axisymmetric models, but the ability of axisymmetric models to capture three-dimensional space with two-dimensional mechanics make axisymmetric models more efficient. Due to this gained efficiency, the majority of analyses in this work make use of axisymmetric models rather than three-dimensional models. In certain cases three-dimensional results will be compared to

axisymmetric results to ensure that three-dimensional models and methodologies provide accurate solutions. Unless otherwise specified, the material properties used throughout this work are listed in Table 4.1.

Table 4.1 Listing of symbols and values for material properties

Property	Symbol	Value
Modulus of elasticity	E	3.4*GPa*
Poisson's ratio	ν	0.32
Thickness	h	0.04 *mm*
Debond	a	variable
Pressure	p	0.01 *MPa*
Net coefficient of thermal expansion	α_{film}-$\alpha_{substrate}$	85E-6 *mm*/(*mm*$^{\circ}$C)
Stress free temperature	*SFT*	175 °C
Operating temperature	T	20 °C

4.4.1 Three-dimensional solid model

Figure 4.3 represents the geometric model developed for the three-dimensional blister models. Radial symmetry in pressurized blister tests allows any size pie slice or arc segment to be used, as long as symmetry conditions are prescribed at the edges. This thesis uses a quarter circular model because this is the only symmetry plane available in the half-blister geometry to be analyzed in Chapter 6.

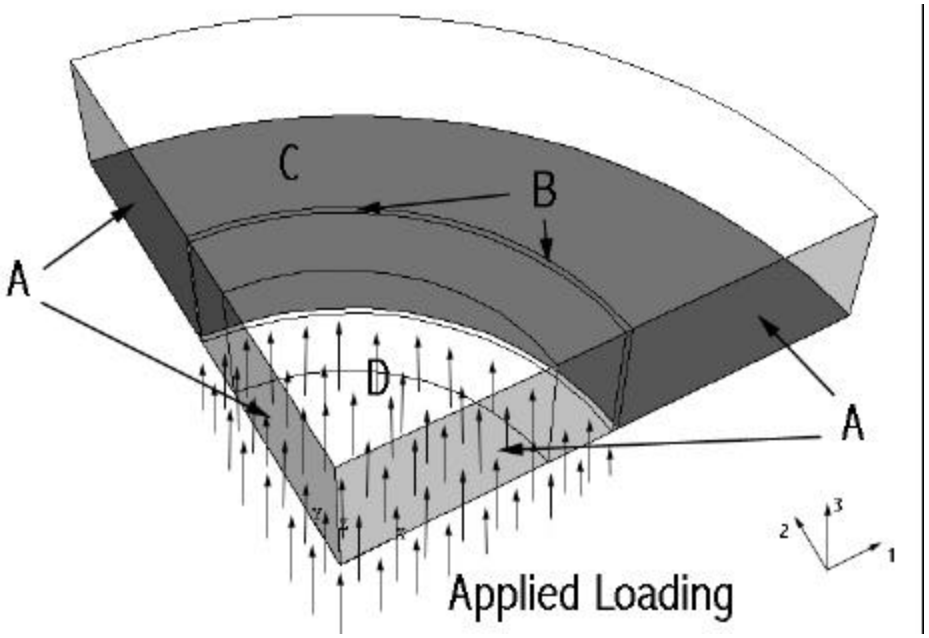

Figure 4.3. Three-dimensional pressurized blister finite element model setup

The edges denoted A are symmetry planes. The left symmetry plane (2-3) has the boundary condition, u_1=0. The right symmetry plane (1-3) has the boundary condition, u_2=0. The volume pointed out by B is a partition that is one element wide to facilitate determination of energy release rates, which will be described in detail in *Section 4.4*. The radius at which the partition of B exists is the assumed extent of debond for the model. Section C points to the bottom surface of the film. This region is sufficiently large to negate any effects caused by the curtailing of geometry at the model's edge. The entire area of C is prescribed as encastre, meaning all nodes are constrained in all degrees of freedom (u_1=u_2=u_3=0). This boundary condition is representative of intact adhesion to an rigid substrate beyond the area of debond. The volume designated D contains a meshing scheme to stabilize the mesh into uniformly sized elements before reaching volume B. The applied loading is uniform pressure loading over the debonded region, as indicated in the figure. The loading is applied to the bottom of the adhesive over a quarter-circular area of debond radius a. The radius a is increased in successive models to simulate increasing debond.

Having been qualified in *Chapter 3 Element Selection*, reduced integration brick elements (C3D8R) are used for three-dimensional models of the pressurized blister. Figure 4.4 demonstrates a typical deformed three-dimensional mesh. The mesh is refined towards the edge of debond (radius a) from both directions to capture the singularity caused by stress concentrations at the boundary change. Capturing the singularity is important because determination of energy release rate results occurs at this location. Overall mesh refinement of three-dimensional models is such that the strain energy, U_S, of the model is converged to 0.03% between meshes, calculated as,

$$PercentConvergence = \left| \frac{U_{refined} - U_{coarse}}{U_{coarse}} \right| \times 100. \tag{4.19}$$

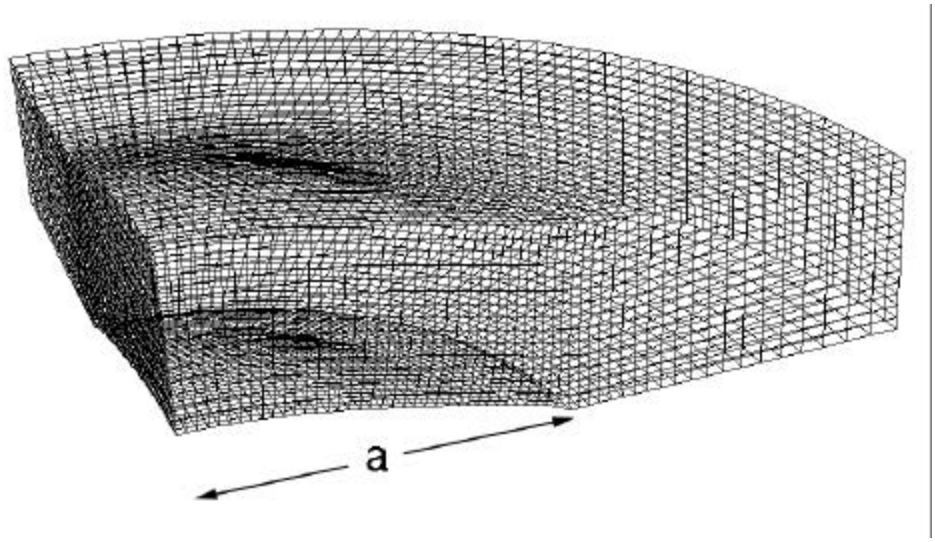

Figure 4.4 Typical mesh scheme for three-dimensional pressure blister models

4.4.2 Axisymmetric solid model

The axisymmetric model of the pressurized blister is a two-dimensional simplification of the three-dimensional model of Figure 4.3. If you could imagine slicing the three-dimensional model radially with a straight edge and viewing that slice perpendicular to its face, you are left with the axisymmetric configuration of Figure 4.5.

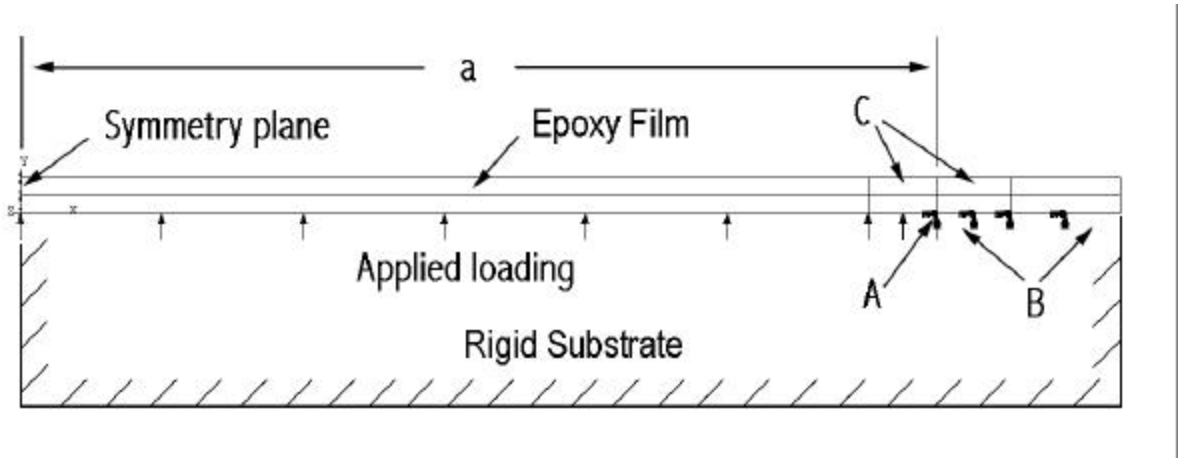

Figure 4.5. Schematic of axisymmetric finite element model setup for pressurized blister

The symmetry plane by which the model is revolved is denoted to the left. Pressure is applied over the debond radius, *a*, which is a parameter changed from model to model to simulate crack growth. Point A represents the extent of debond, with applied loading to the left, and simulated adherence denoted by B to the right. The length of the adhered

area (A to end) is sufficient to ensure there are no effects from the truncated geometry. In reality, the material would continue past this point. The adherence is captured in a fully restrained boundary condition ($u_1=u_2=q_3=0$). The areas indicated by C are zones of mesh refinement, designed to capture the singularity at the crack tip A. The axisymmetric model has also been exposed to residual stresses. Residual stress can arise from many different factors: thermal mismatch, moisture absorption, and chemical reaction to name a few. In this research, residual stress is incorporated into finite element models by the inclusion of thermal mismatch. A coefficient of thermal expansion, α ($^{\circ}C^{-1}$), is applied to both the film and substrate (for a rigid substrate $\alpha_{substrate}=0$) and the temperature is varied from the stress free temperature, SFT ($^{\circ}C$), to the operating temperature, T ($^{\circ}C$). The values for these quantities can be found in Table 4.1.

Overall mesh refinement of the axisymmetric models converges the strain energy, U_S, of the model to 0.05% as calculated in Eq. 4.19. Axisymmetric pressurized blister models use first order, reduced integration, quadrilateral elements (CAX4R) as selected in *Chapter 3 Element Selection*. Figure 4.6 presents a typical deformed axisymmetric mesh with a small crack length, *a*.

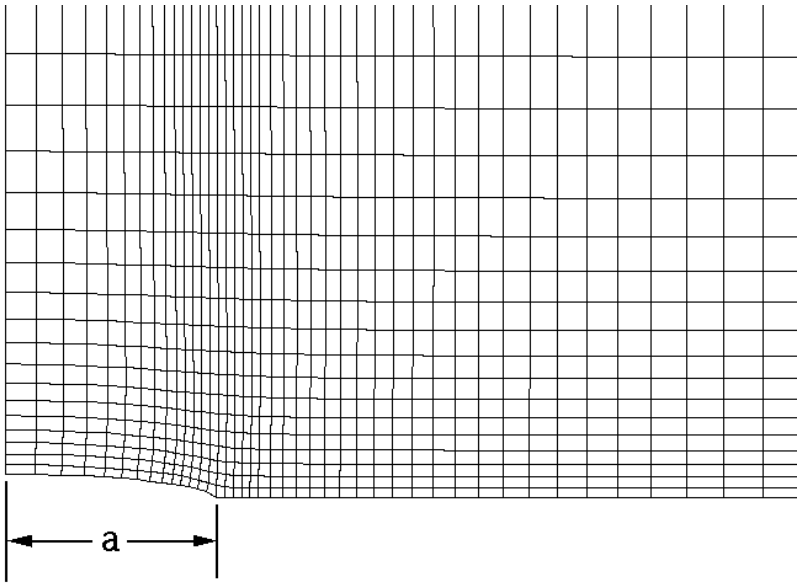

Figure 4.6. Typical mesh scheme for axisymmetric pressure blister models

4.5 Energy release rate extraction

4.5.1 General data extraction

The main focus of this effort is to determine energy release rates, G, in pressurized blister tests. Deformations in pressurized blister tests are independent of q, so that mode III or anti-plane tearing energy release rates are zero by definition. Therefore only G_I and G_{II} need to be calculated in both three-dimensional and axisymmetric models.

Energy release rates are associated with the strain energy developed by reaction forces along the entire crack front and the displacements at the crack front caused by incremental crack advance. Therefore the energy release rates can be calculated in an overall sense by determining the change in strain energy or discretely by the modified crack closure method using reaction forces and displacements.

For both the three-dimensional and axisymmetric models, the strain energy, U, can be queried from an analysis with initial crack length a, and from a second analysis with final crack length ($a+\Delta a$) to calculate the overall energy release rate,

$$G_{total} = \frac{\left|U_f - U_i\right|}{\Delta A} \tag{4.20}$$

Where ΔA (mm^2) is defined as,

$$\Delta A = p\,(a + \Delta a)^2 - pa^2 \tag{4.21}$$

The modified crack closure method used in the majority of this study requires two phases; a phase for extraction of reaction forces, and a phase for extracting displacements. Figure 4.7 illustrates a two-dimensional slice of material that defines the reaction forces, RF_r and RF_z, to be queried from node i in the first phase of the crack closure analysis.

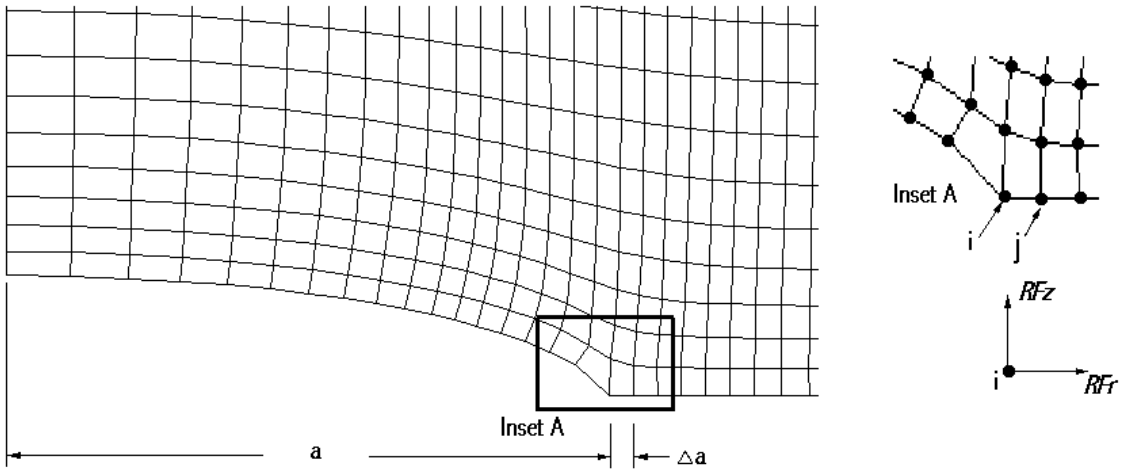

Figure 4.7. Reaction force queries for phase 1 of modified crack closure

Upon releasing one element of length Δa of the bottom surface to simulate debond propagation, the displacements u_r and u_z of node i can be obtained. Figure 4.8 demonstrates the nodal displacements to be queried from models.

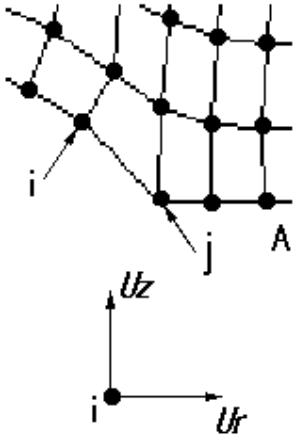

Figure 4.8. Displacement queries for phase 2 of modified crack closure

The following sections describe how energy release rates are calculated from reaction forces, displacement data, and the incremental release length Δa for the three-dimensional and axisymmetric finite element models.

4.5.2 Three-dimensional blisters

Three-dimensional models require summation of G contributions from all nodes along the crack front. The crack front is represented by nodal points as pictured in Figure 4.9.

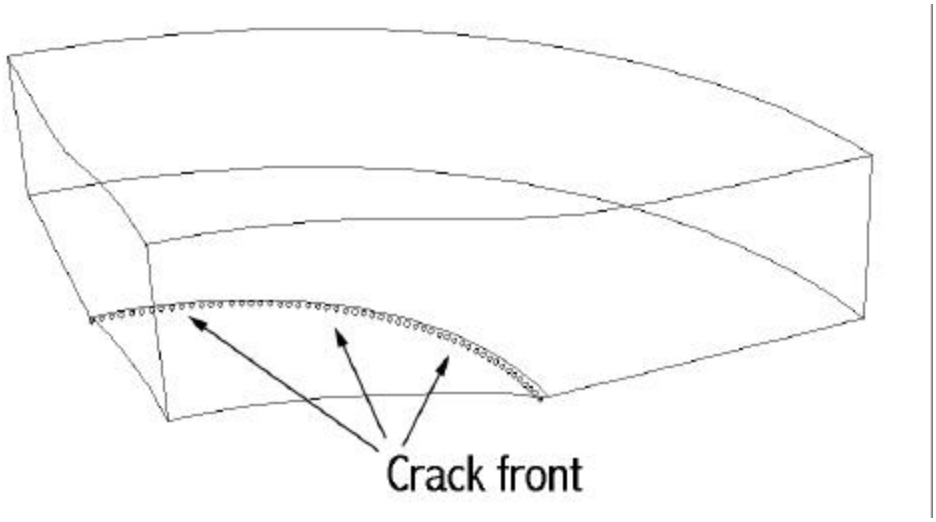

Figure 4.9. Nodal points comprising the crack front in a three-dimensional model

In reality, every point along the crack front of a blister will experience the same reaction forces and displacements because of axisymmetry. A converged three-dimensional finite element analysis will demonstrate this physical reality. Due to the near impossibility of obtaining exactly the same answers at all nodes along the crack front circumference with an approximate method, average nodal reaction forces and displacements are multiplied by the number of nodes along the circumference. Reaction force and displacement data is extracted from models in Cartesian coordinates and is then transformed into modified cylindrical coordinates. Figure 4.10 is a diagram showing how the radial and tangential coordinates vary with changing theta, θ.

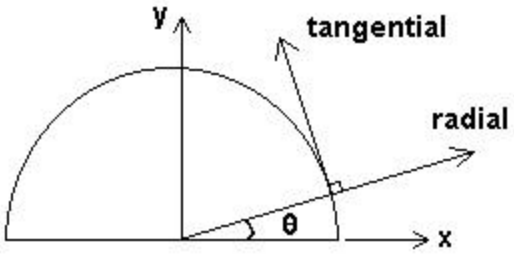

Figure 4.10. Diagram of modified cylindrical coordinate system

The transformation requires a coordinate rotation for each angle the data is extracted from. The rotations are,

$$RF_{\text{radial}} = RF_X \cos(q) + RF_Y \sin(q) \tag{4.22}$$

$$RF_{\text{tangential}} = RF_Y \cos(q) - RF_X \sin(q). \tag{4.23}$$

The same rotation equations apply for displacements, u_{radial} and $u_{tangential}$.
Hence for three-dimensional blisters, the energy release rate expressions are,

$$G_I = \frac{n(\overline{RF}_z)(\overline{u}_z)}{2\Delta A} \tag{4.24}$$

$$G_{II} = \frac{n(\overline{RF}_r)(\overline{u}_r)}{2\Delta A} \tag{4.25}$$

$$G_{total} = G_I + G_{II} \tag{4.26}$$

where n is the number of nodes along the crack front circumference, and ΔA is defined as in Eq. (4.21).

4.5.3 Axisymmetric blisters

In an axisymmetric analysis in ABAQUS, the reaction forces obtained for the two-dimensional planar surface represent an integration of forces about the circumference, 2π. For example, imagine sweeping the two-dimensional planar surface 360° about its center axis in angular increments of 60°. The value of a particular mode reaction force at a node i from the two-dimensional axisymmetric model will actually be the summation of the reaction forces from each increment,

$$RF_i = RF_{60^\circ} + RF_{120^\circ} + RF_{180^\circ} + RF_{240^\circ} + RF_{300^\circ} + RF_{360^\circ}. \tag{4.27}$$

In ABAQUS this representation is not performed incrementally, but rather in integral form. Having thus obtained both nodal reaction forces and displacements as described in Section 4.5.1, the following formulae calculate energy release rates via the modified crack closure method for the axisymmetric case,

$$G_I = \frac{(RF_z)(u_z)}{2\Delta A} \tag{4.28}$$

$$G_{II} = \frac{(RF_r)(u_r)}{2\Delta A} \tag{4.29}$$

$$G_{total} = G_I + G_{II} \tag{4.30}$$

with ΔA defined as in Eq. (4.21).

4.6 Confirmation of deformation mechanics

Having established the limiting cases of thin plate theory and semi-infinite medium theory and developed the finite element structure for the pressurized blister test, results can be analyzed in detail. The following two subsections compare linear displacement profiles from finite element models to profiles from theory in the limiting cases. This comparison will ensure that the finite element models are correctly capturing the deformation mechanics of blister testing. The third subsection establishes the deformation mechanics for the pressurized blister with residual stress, which adds a new complication in modeling. This analysis includes both linear and non-linear geometry.

4.6.1 Thin plate

Figure 4.11 compares linear finite element results and theoretical displacement profiles for the thin plate model with a debond radius of 2 *mm*. The blister is pressurized by 0.006895 *MPa* and meshing has been refined to produce the convergence stated in Sections 4.4.1 and 4.4.2. The axisymmetric model uses first order, full integration quadrilateral elements, and the three-dimensional model uses first order, reduced integration brick elements. Since plate theory assumes all displacements occur at the mid-surface, the displacement profiles of the axisymmetric and three-dimensional solid finite element models were also obtained from the model mid-surface.

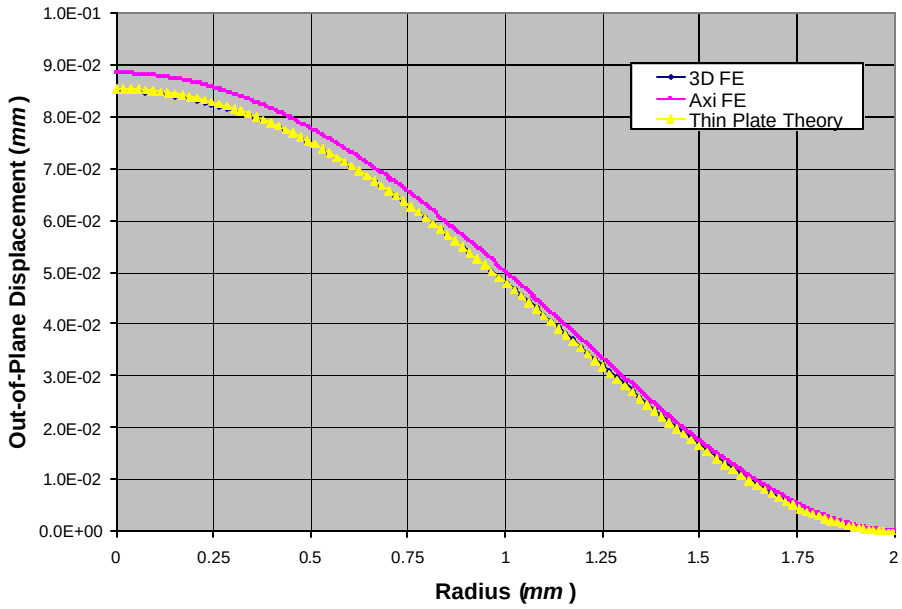

Figure 4.11. Comparison of finite element and thin plate theory profiles at a debond radius of 2 *mm*

In Figure 4.11 it is evident that the axisymmetric results produce a slightly higher displacement result than theory, whereas the three-dimensional results share the same curve as theory. To obtain a quantitative assessment of finite element model performance, a statistical analysis has been performed on the data of Figure 4.11. The analysis includes calculation of standard deviations of finite element results from thin plate theory and signal to noise ratios of this standard deviation. Standard deviation, s_x, is the square root of the variance, s_x^2, of the data,

$$\hat{s}_x = \sqrt{\frac{\sum (residualerror - meanerror)^2}{n-1}} \tag{4.31}$$

$$\hat{s}_x^2 = \frac{\sum (residualerror - meanerror)^2}{n-1} \tag{4.32}$$

where n is the number of data points analyzed, residual error is w_{FEA}-w_{theory} at a particular radius, and mean error is the average of all residual errors. The signal to noise ratio, *SNR*, is defined as the maximum signal divided by the standard deviation,

$$SNR = \frac{signal_{\max}}{\hat{s}_x} \tag{4.33}$$

The singularity effect at the crack tip caused by a change in boundary constraints and described by St. Venant compromises approximately five percent of the data near the debond front, and therefore this data has been eliminated from the study. The results from the truncated deflection data appear in Table 4.2.

Table 4.2. Statistical comparison of finite element results to thin plate theory

Statistic	3-D Solid	Axisymmetric Solid
Standard Deviation	1.440E-04	8.299E-04
Signal to Noise Ratio (*SNR*)	589.3	106.4

The data indicates that both the three-dimensional and axisymmetric models adhere to theory in a range well above the error, or noise level. The counter-intuitive result of Table 4.2 is that agreement with theory is much stronger in the three-dimensional model. Intuition would suggest that the axisymmetric model would better approximate theory due to a shared boundary condition eliminating the circumferential degree of freedom. For this case, it is hypothesized that the discrete representation of the circumferential

degree of freedom in the 3-D model produces a stiffer solution than the direct integration of this degree of freedom in the axisymmetric model. This could explain the high axisymmetric profile seen in Figure 4.11 and the stronger correlation in the 3-D model.

4.6.2 Semi-infinite medium

Figure 4.12 compares finite element results and theoretical displacement profiles for a model representative of a semi-infinite medium, which maintains a crack length of 0.0067 *mm*. Again, the blister is pressurized with 0.006895 *MPa*. Meshing has been refined so as to produce strain energy convergence as stated in Sections 4.4.1 and 4.4.2; 0.03% for three-dimensional models and 0.05% for axisymmetric models. The axisymmetric model uses first order, full integration, quadrilateral elements, and the three-dimensional model uses first order, reduced integration, brick elements. The theoretical profile is based on the displacement between the thin film and the surface of the substrate, and thus the finite element models were queried for displacements along this same surface.

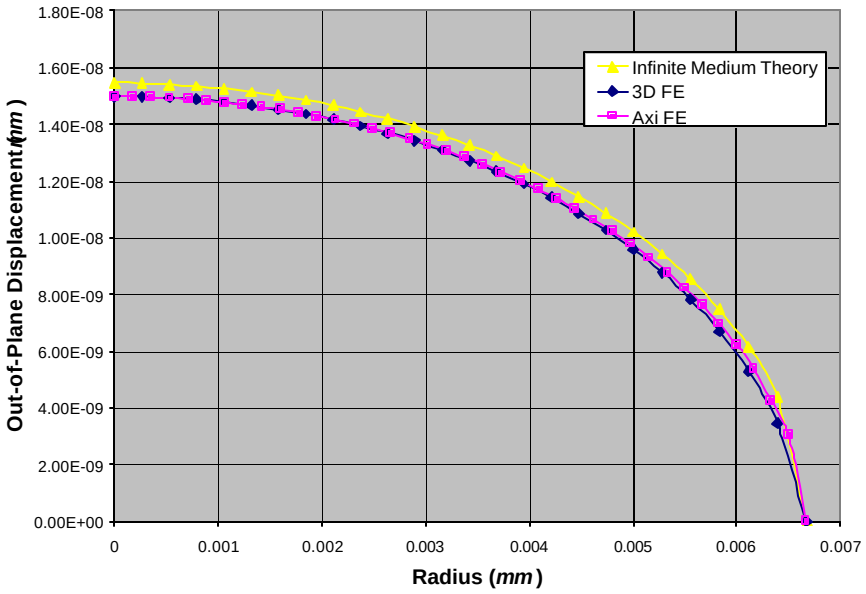

Figure 4.12 Comparison of finite element and infinite medium theory at a debond radius of 0.0067*mm*

The curves in Figure 4.12 indicate that the finite element models provide a slightly stiffer solution than semi-infinite medium theory, which is typical in linear static finite element

analyses. Finite element analyses approximate true solutions by assuming a mathematical model. The mathematical model constrains the behavior according to its assumed form of the displacement field, thereby artificially stiffening the structure. A quantitative assessment of the data in the form of standard deviations and *SNRs* is presented in Table 4.3. Due to the smaller crack length, the singularity effect at the crack front compromises data over a larger percentage of the overall span. Therefore the final ten percent of data near the singularity has been excluded from the analysis to avoid these St. Venant's effects.

Table 4.3 Statistical comparison of finite element results to semi-infinite medium theory

Statistic	3D Solid	Axisymmetric Solid
Standard Deviation	8.570E-11	8.662E-12
Signal to Noise Ratio (*SNR*)	174.9	1728.5

According to the SNR's of Table 4.3, the axisymmetric model demonstrates much higher correlation to theory than the 3-D model for the semi-infinite medium case. Before accepting the large difference in SNR's, consideration must be given to the sensitivity of these numbers to the orders of magnitude at which calculations are carried out. The magnitudes of computed variances are on the order of 10^{-20}. Additionally, it is evident in Figure 4.12 that the sampling of the 3-D results is less than the sampling of the axisymmetric model. Refinement of the meshing in the 3-D model may enhance the correlation of deflection results. Greater refinement would ensure that all of the energy due to loading is transferred into the film.

4.6.3 Inclusion of residual stress

4.6.3.1 Linear Analysis

The inclusion of residual stress in axisymmetric pressurized blister models introduced new complications to modeling. Original linear models without residual stress contained additional material beyond the extent of debond on the average of two times the film thickness. Application of residual stress to this geometry resulted in the blister having no apparent deflection. To determine the cause of the lack of deformation, the blister was treated as a free hanging film without a substrate, and the amount of adhered material beyond the extent of debond was increased from twice the film thickness to fifteen times

the film thickness. The blister maintains a debond radius of 1 *mm* and is subjected to a constant 0.01 *MPa* pressure. The level of meshing is held constant so that the only variable is the amount of adhered material behind the debond. The resulting deflection profiles of this test can be found in Figure 4.13. Figure 4.14 shows the convergence of profiles with varying amounts of adhered material for residual stress models.

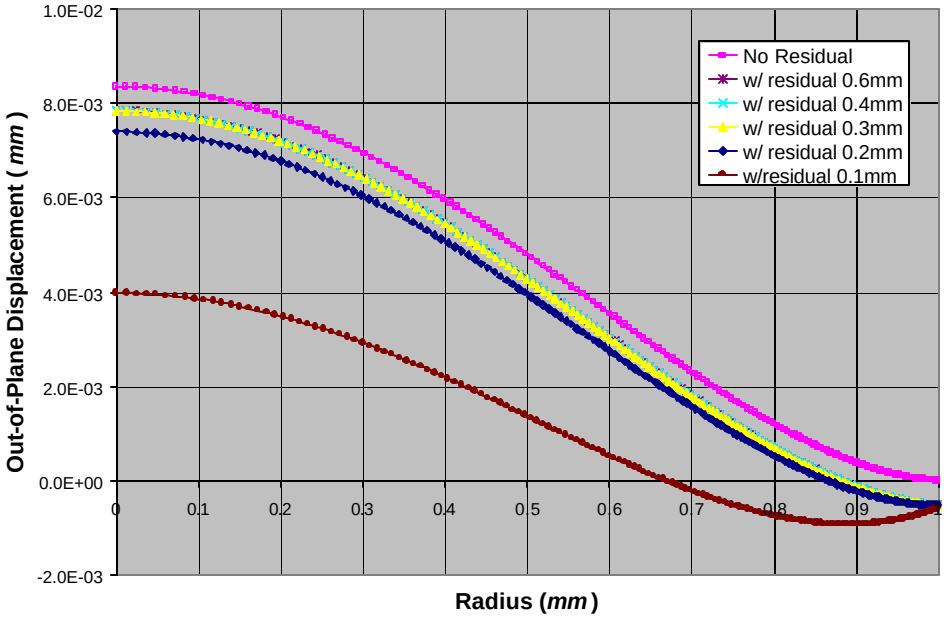

Figure 4.13. Effect of adhered material behind debond – LINEAR ANALYSIS

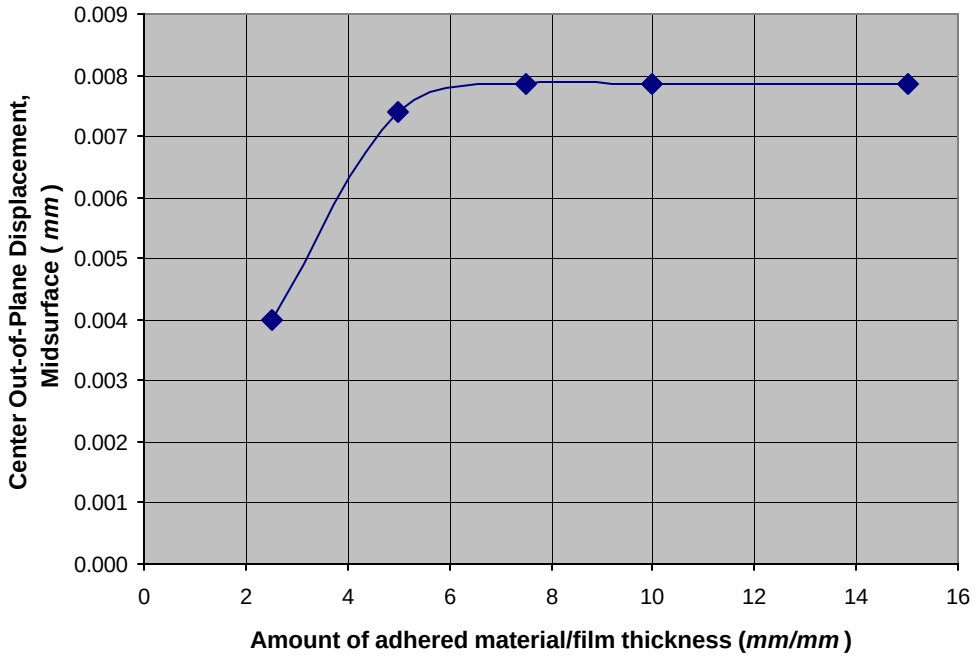

Figure 4.14. Convergence of central deflection with varying amounts of adhered material behind debond - LINEAR

Figure 4.13 indicates that a hinging effect occurs at 1 *mm* for the curves with residual stress when the amount of adhered material behind the extent of debond decreases. According to Figure 4.14 convergence is achieved when the amount of adhered film behind the crack front is approximately 10 times the film thickness, which is 0.4 *mm* of additional material. The percent difference in maximum deflection between adhered material of 0.3 *mm* and 0.4 *mm* is 0.02%, which is defined as,

$$\left| \frac{w_0(0.4mm) - w_0(0.3mm)}{w_0(0.3mm)} \right| \times 100. \tag{4.34}$$

A convergence plot is not necessary for the case without residual stress because the percent difference in maximum deflection between having 0.1 *mm* and 0.6 *mm* adhered material is 0.12%, which is calculated similar to Eq. 4.34. This indicates that the amount of adhered material doesn't play a significant role in the absence of residual stress for the linear case. The downward translation of the converged residual stress curve from the non-residual stress curve is caused by the compression of the film due to residual stress, which shifts the midsurface. This shift sometimes causes negative displacements.

Adjusting this shift results in nearly identical residual and non-residual curves for the linear analysis.

To understand this result, shell and pseudo-axi finite element analyses were developed for comparison purposes. The representations of each of these analyses are illustrated in Figure 4.15. Pseudo-axi representation refers to an axisymmetric blister that is fully restrained across the thickness at the length of debond, *a*. From this point in the thesis, full-axi will refer to the geometric representation used throughout this thesis that only has the bottom surface constrained. Note that neither shell nor pseudo-axi representations would experience effects from additional adhered material beyond the debond due to the clamped boundary condition present across the thickness of the film at the edge of debond.

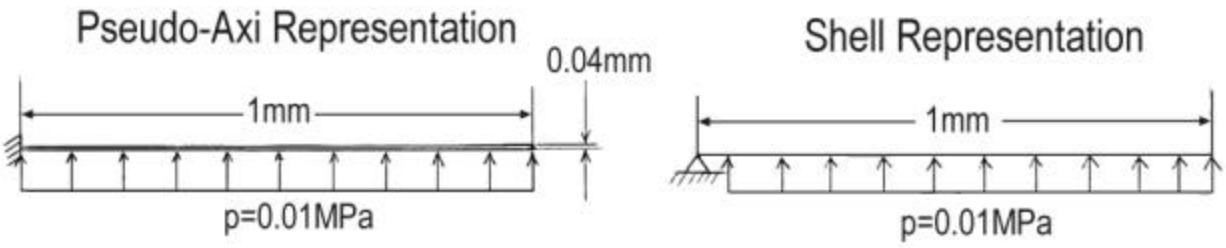

Figure 4.15. Shell and pseudo-axisymmetric representations

The deflection profile results from these representations are shown in Figure 4.16. Mesh refinement of the pseudo-axi model converges the central mid-surface deflection to 2.1% difference between meshes and mesh refinement of the shell model converges the central mid-surface deflection to within 0.01%.

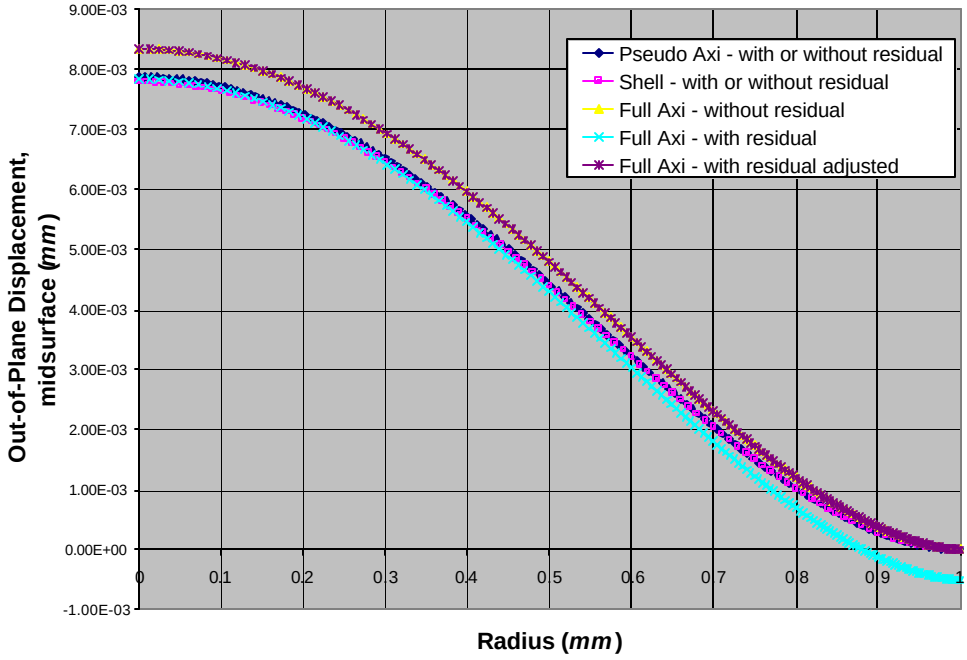

Figure 4.16. Comparison of linear representations for 1 *mm* debond radius

In Figure 4.16, converged pseudo-axi and shell analyses produce the same profile, but the full-axi representation used throughout this work predicts slightly higher deflections. This increase in mid-surface deflection is seen because the full-axi analysis only applies boundary constraints to the bottom surface whereas pseudo-axi and shell analyses apply boundary constraints directly to the mid-surface of the film. Figure 4.16 also confirms that there is no evidence of effects from residual stresses in displacement profiles of linear analyses for any choice of representation. The adjusted residual stress full-axi mid-surface displacement curve has a center blister deflection only 0.06% lower than the full-axi curve without residual stress. It would be expected that the addition of residual stress would cause the deflections to decrease due to compressive strains in the radial direction that artificially stiffen the film. The lack of change in mid-surface deflections with inclusion of residual stress in any blister representation rules out representation issues. The next troubleshooting course of action was to assess the effects of allowing for large strains and large displacements in a non-linear analysis. The results are presented in the following section.

4.6.3.2 Non-linear analysis

The same procedure used in the linear analysis for adding additional adhered material behind the debond was used in a non-linear analysis. The deflection profile results of the non-linear analysis of the pressurized blister test for a 1 *mm* debond radius with 0.01 *MPa* of pressurization are presented in Figure 4.17. To isolate non-linearity as the only variable, the same meshes from the linear analysis are used.

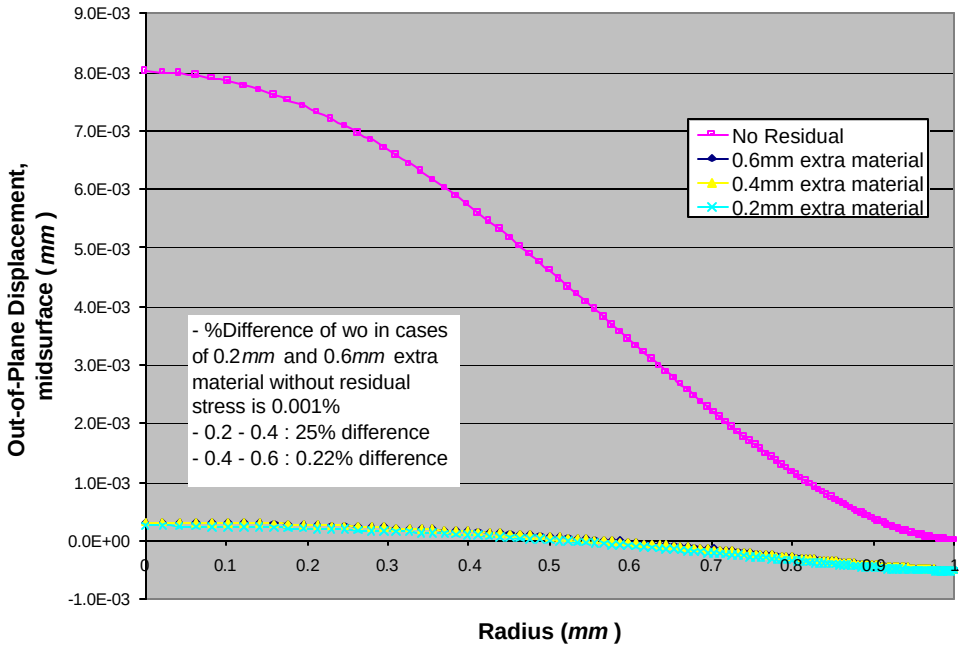

Figure 4.17. Effect of adhered material behind debond - NONLINEAR ANALYSIS

The most interesting aspect of Figure 4.17 is that the converged residual stress model has a much lower deflection profile than the model without residual stress, as hypothesized in *Section 4.6.3.1*. Again, the downward translation of the residual stress curves from the non-residual stress curve is an artifact of a shifted midsurface due to compression of the film by residual stress. At first glance it appears that the amount of material behind the debond has minimal effect. However, convergence is not obtained for this case until the adhered material reaches 10 times the film thickness, as shown in the convergence plot of Figure 4.18. As in the linear analysis, the models without residual stress were unaffected by the amount of additional adhered material behind the extent of debond. The difference in central deflection between additional adhered material of 0.2*mm* and 0.6*mm* was 0.001%.

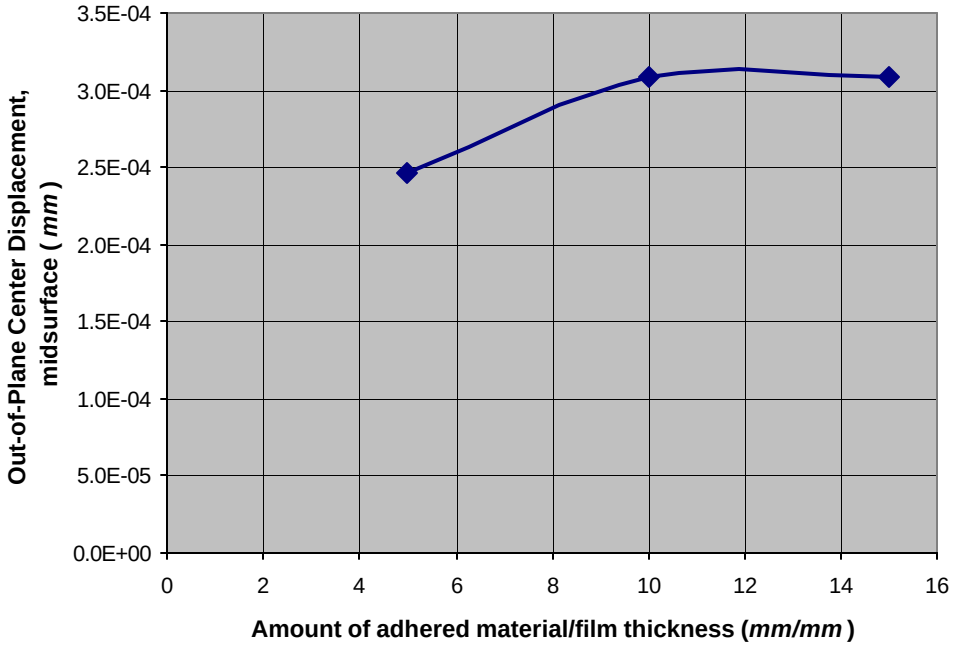

Figure 4.18. Convergence of central deflection with varying amounts of adhered material

A check on the amount of adhered material required for convergence of pressurized blister deflections in the residual stress models has been carried out for all debond radii used in this work. For all cases, the film thickness and applied pressure remain constant. A table of the results can be found in Table 4.4.

Table 4.4. Amount of additional material required for convergence

Debond Radius (*mm*)	Additional Material Required (*mm*)
0.01	1
0.02	0.9
0.08	0.8
0.2	0.8
0.4	0.6
0.5	0.6
1	0.6

Table 4.4 shows that smaller debonds are more susceptible to the effects of residual stress and require a greater amount of adhered material behind the debond for convergence. However, the change in additional material required between the smallest debond radius of 0.01*mm* and the largest of 1*mm* is insignificant compared to the change in radius size.

As in the previous section on linear residual stress analysis, the different model representations of Figure 4.15 were used for comparison purposes, and the meshes remain the same. Refinement of meshing in the pseudo-axi representation converges out out-of-plane maximum displacements to the same percentage as in the linear analysis of *Section 4.6.3.1*. Convergence for the shell representation slightly increases to 0.03% difference in central out-of-plane displacements. The deflection profile results from the non-linear comparison are presented in Figure 4.19.

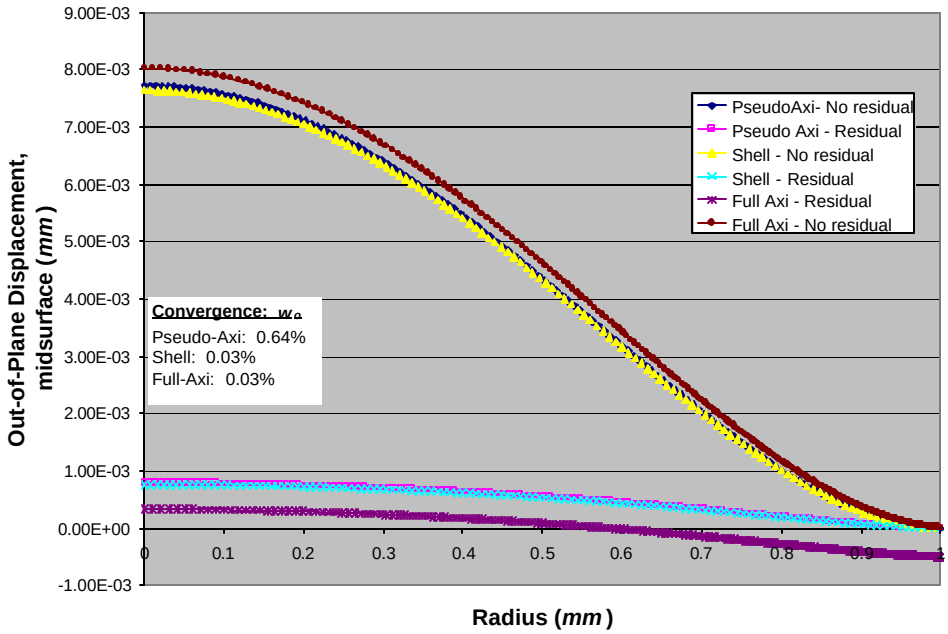

Figure 4.19. Comparison of non-linear representations at a 1 *mm* debond radius

Unlike the linear analysis, all non-linear model representations capture the deformation caused by the addition of residual stress. As expected, deflection profiles decrease in magnitude with residual stress. The pseudo-axi and shell representations have comparable deflection profiles and the full-axi model has a slightly higher deflection profile. Again, this is due to direct application of boundary constraints to the mid-surface in pseudo-axi and shell representations, which overconstrains simulation of adherence. Producing similar results with all representations builds confidence in the models and the choice of non-linear analysis.

4.7 Transitioning from an infinite medium to a thin plate

Following the methodology set forth by Bennett, et al, [13] a linear analysis has been performed to confirm the transition of blister behavior from infinite medium theory to thin plate theory. The difference being that Bennett, et al, varied specimen thickness, whereas this analysis holds specimen thickness constant and varies the debond radius instead. The analysis was repeated for discrete specimen debond lengths ranging from 0.0067 *mm* to 2 *mm* (*h/a*=6 to 0.02) for the axisymmetric model, and from 0.0067 *mm* to 1 *mm* (*h/a*=6 to 0.04) for the three dimensional model. Upon demonstration of transition between the two theories, an attempt is made to develop an empirical expression based on the data from the finite element code that predicts the energy release rate between the two theories. Throughout the transition analysis, the film thickness, *h*, is held to 0.04 *mm* and the pressure is held at 0.06895 *MPa*. The analysis is limited to small displacements, small strains because the theory being compared to is a linear elastic solution with small displacements.

4.7.1 Axisymmetric

The energy release rate results of the axisymmetric pressurized blister models computed by all three methods (crack closure, strain energy, J-integral) are presented in Figure 4.20 against theoretical results. The figure clearly indicates correlation with each theory at either extreme. Mesh refinement produced results such that the strain energy, U_S, of the models is converged to 0.05% difference between successive meshes. Note that the crack closure curve and the strain energy curve coincide.

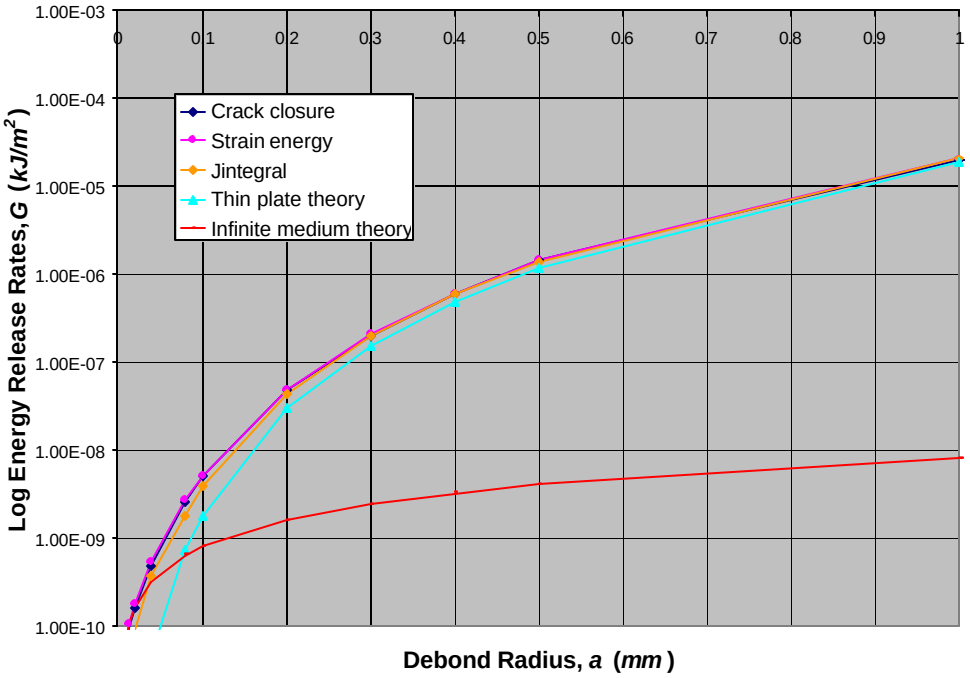

Figure 4.20. Energy release rate results for axisymmetric model of pressurized blister

The data from the axisymmetric analysis can be found in Table 4.5, and includes results from all three methods of obtaining energy release rate results. In the manner of Bennett et al [13], energy release rate data is presented in dimensionless pressure form, p^2a/EG, versus thickness to span (h/a) for comparison purposes where G represents the total energy release rate.

Table 4.5. Axisymmetric dimensionless pressure data

	Finite Element			Theory	
h/a	CC	STR	J-INT	TP	IM
6	1.9792E+00	1.8080E+00	N/A	2.5668E+03	1.7500E+00
5	2.0158E+00	1.7967E+00	N/A	1.4854E+03	1.7500E+00
4	1.9948E+00	1.7791E+00	3.1063E+00	7.6055E+02	1.7500E+00
3	1.8972E+00	1.7248E+00	4.1354E+00	3.2086E+02	1.7500E+00
2	1.7453E+00	1.6014E+00	3.0998E+00	9.5068E+01	1.7500E+00
1	1.1202E+00	1.0637E+00	1.4922E+00	1.1884E+01	1.7500E+00
0.5	4.3026E-01	4.2226E-01	6.1190E-01	1.4854E+00	1.7500E+00
0.4	2.8323E-01	2.7935E-01	3.6099E-01	7.6055E-01	1.7500E+00
0.2	5.8878E-02	5.8790E-02	6.3038E-02	9.5068E-02	1.7500E+00
0.133333	2.0946E-02	2.0676E-02	2.0909E-02	2.8168E-02	1.7500E+00
0.1	9.4509E-03	9.4700E-03	9.5162E-03	1.1884E-02	1.7500E+00
0.08	4.9734E-03	4.9961E-03	5.1225E-03	6.0844E-03	1.7500E+00
0.04	7.2387E-04	6.9545E-04	6.9680E-04	7.6055E-04	1.7500E+00
0.02	9.5123E-05	9.0704E-05	9.0904E-05	9.5068E-05	1.7500E+00

The results of the numerical analyses compared well with the theoretical limit cases. Percent differences were computed using Eq. 4.35 with respect to theoretical values.

$$\%diff = \frac{\left| val_{crackclosure} - val_{theory} \right|}{val_{theory}} \tag{4.35}$$

Taking the limit case of thin plate theory to be h/a=0.02, crack closure differed by 0.058%, strain energy by 4.6%, and J-integral by 4.4%. Considering the limit case of infinite medium theory to be h/a=6, crack closure differed by 13.1% and strain energy by 3.3%. The J-integral method required extensive, time consuming mesh refinement and thus results are not available for this test case. Figure 4.21 demonstrates transition between theories by plotting the dimensionless pressure data, p^2a/EG, from Table 4.3 with the analytical limit solutions of the infinite medium and thin plate, against the thickness to span ratio (h/a).

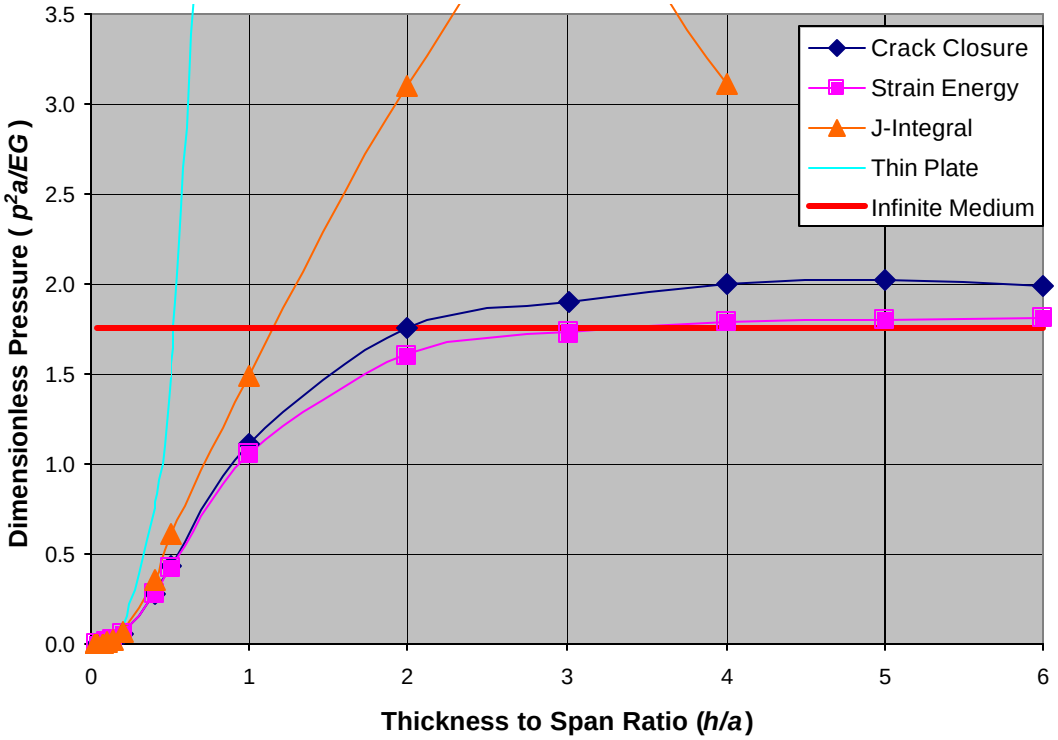

Figure 4.21. Comparison of axisymmetric energy release rate methods and theory

The results of Figure 4.21 are in very good agreement with the transition findings of Bennett et al [13]. Following the strain energy curve of Figure 4.21, it is evident that the models deviate from thin plate theory even at relatively low values of h/a (large debond

radii). At *h/a* ratios of 3 through 6 (debond radii of 0.013 *mm* to 0.0067 *mm*), the models tend towards infinite-medium behavior. The FE strain energy curve closely follows theory at either limiting case. The crack-closure method slightly overshoots the limiting case of an infinite medium. The discrete approximation made when choosing a Δa for the limiting condition of the crack closure integral of Eq. 2.15 could be the cause for this overshoot. Further mesh refinement would lessen the error. The J-integral produced results similar to strain energy at larger debond radii, but failed to remain within theory as the debond radii approached the infinite medium limiting condition. The failure of the J-integral at small debond radii is caused by the extensive distortion resulting from the same pressure being applied to a much smaller amount of material. Therefore significant mesh refinement around the crack is required for accurate results. Since mesh adjustments with the J-integral require direct manipulation of ABAQUS/Standard code, this level of refinement becomes impractical compared to the lower level of refinement required for the other methods of obtaining energy release rates.

4.7.2 Three-Dimensional

The data from the three-dimensional pressurized blister analysis can be found in Table 4.4, and includes results from the crack closure and strain energy methods of obtaining energy release rate results. The J-integral in three dimensions is a challenging analysis, becoming unjustifiable for this comparison. Refinement of meshing is such that the strain energy of the models is converged to 0.08% difference between successive meshes.

Table 4.6. Three-dimensional dimensionless pressure data

	Finite Element		Theory	
h/a	CC	STR	TP	IM
6	1.7822E+00	1.7822E+00	2.5668E+03	1.7500E+00
5	1.7286E+00	1.7259E+00	1.4854E+03	1.7500E+00
4	1.7241E+00	1.7241E+00	7.6055E+02	1.7500E+00
3	1.7302E+00	1.7302E+00	3.2086E+02	1.7500E+00
2	1.5882E+00	1.5881E+00	9.5068E+01	1.7500E+00
1	1.0405E+00	1.0405E+00	1.1884E+01	1.7500E+00
0.5	4.1290E-01	4.1290E-01	1.4854E+00	1.7500E+00
0.4	2.7905E-01	2.7903E-01	7.6055E-01	1.7500E+00
0.2	5.9243E-02	5.9243E-02	9.5068E-02	1.7500E+00
0.133333	2.0125E-02	2.0127E-02	2.8168E-02	1.7500E+00
0.1	9.3468E-03	9.3468E-03	1.1884E-02	1.7500E+00
0.08	4.9719E-03	4.9719E-03	6.0844E-03	1.7500E+00
0.04	6.9016E-04	6.9017E-04	7.6055E-04	1.7500E+00
0.02	9.1092E-05	9.1094E-05	9.5713E-05	1.7500E+00

An important observation of the data in Table 4.6 is that the two energy release rate extraction methods produce almost exactly the same results. This matching of energy release rate by both the crack closure and strain energy methods was not seen in the axisymmetric representation. The greatest percent difference of 0.15% between the two methods occurred at h/a=5, perhaps the least refined mesh. Other differences dropped as low as 0.0001%. The results of the numerical analyses compared well with the theoretical limit cases as well. Taking the limit case of thin plate theory to be h/a=0.02, both crack closure and strain energy differed by 4.8% from thin plate theory. At the other end of the spectrum, considering the limiting case of infinite medium theory to be h/a=6, crack closure and strain energy differed by 1.8% from infinite medium theory. Figure 4.22 graphically compares the data from Table 4.6 by plotting the dimensionless parameter, p^2a/EG, versus the thickness to span ratio, h/a. The analytical limit solutions of the infinite medium and thin plate are also plotted in the figure.

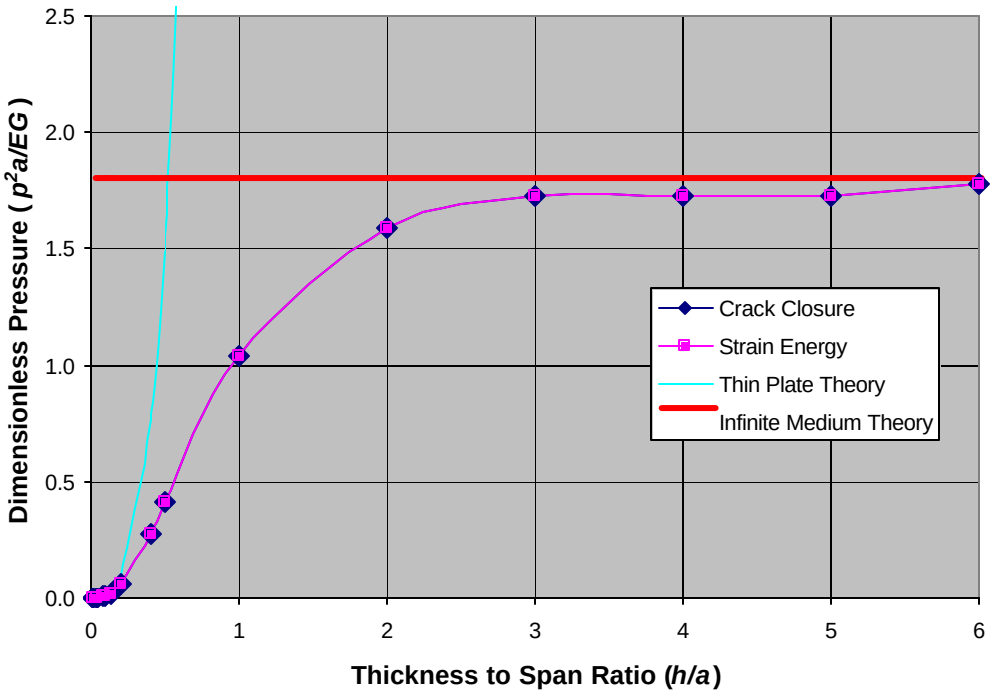

Figure 4.22. Comparison of 3D energy release rates and theory

Figure 4.22 confirms what is presented in Table 4.4. On both ends of the spectra, the finite element energy release rate methods very closely predict the theoretical limits. These results indicate that three-dimensional analyses more closely predict theory than

the axisymmetric results of Figure 4.21. The discrepancy between the two analyses could be due to the fact that the 3-D technique is more representative of Rybicki and Kanninen's [14] crack closure method, which was originally developed for a 2-D planar analysis. Review of literature fails to find an application of the crack closure method to an axisymmetric model.

4.7.3 Dimensionless fracture parameter

The analyses indicate that behavior transition from infinite medium to thin plate is gradual, between h/a=0.2 and h/a=3. The results from this geometrical range do not follow the theory of the two limit cases. Therefore it becomes important to establish fracture parameter master curves to modify the theoretical energy release rate equations, Eq. (4.8) and Eq. (4.16). The modified theory will be based on the form of Eq. 4.36, originally developed by Williams [29].

$$G = \Phi p w_o \tag{4.36}$$

The dimensionless fracture parameter, Φ, replaces the ½ found at both limiting cases, ie Eq. 4.9 and Eq. 4.18. Figure 4.23 plots the fracture parameter against the thickness to debond length ratio for the finite element results.

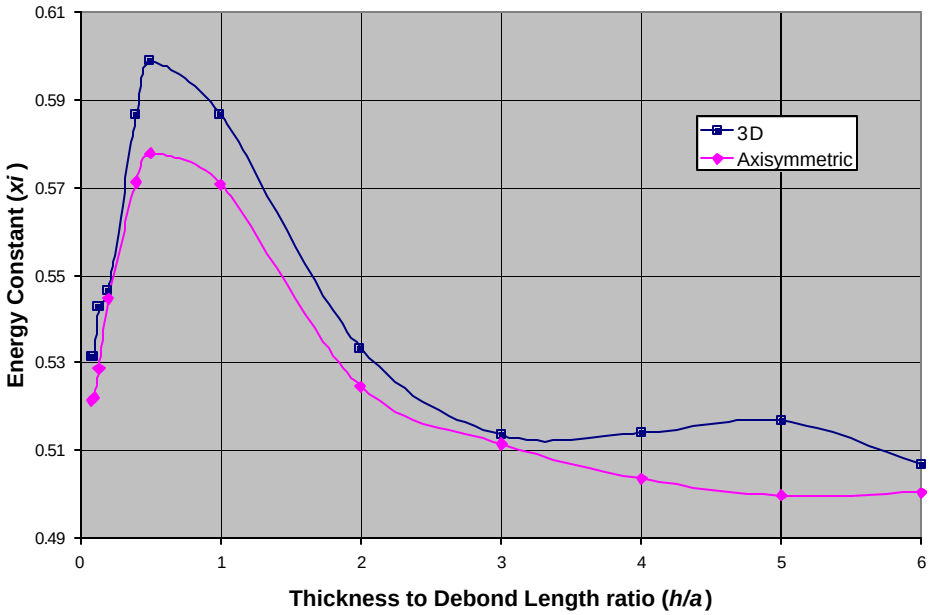

Figure 4.23. Determination of fracture parameter based on finite element results

Since the results of the previous sections indicate that the three-dimensional models produce more accurate results, focus will remain upon the three-dimensional curve in Figure 4.23. It can be seen that Φ values peak at approximately 0.60 around a crack length nearly twice the specimen thickness (h/a=0.5). Significant deviation from theory occurs in the range of h/a=0.05 to h/a=4. The increase in the fracture parameter seen at h/a=5 on the three-dimensional curve initially spanned several h/a's and was cause for concern. A refined mesh at h/a=4 reduced this effect, and produced the result seen in Figure 4.23. This reduction provided proof that the problem could be alleviated by mesh refinement and did not require further attention. For the particular conditions listed in Table 4.1, the fracture parameter curves of Figure 4.23 can be considered master curves for use in modifying the theoretical expression of Eq. (4.9) and Eq. (4.18) to predict energy release rates for conditions between the two limiting cases.

4.8 Energy release rates with residual stress

Inclusion of residual stress in non-linear analyses of the pressurized blister test reduced overall deflections as demonstrated in Section 4.6.3. Figure 4.24 presents energy release rates with and without residual stress, and also compares the linear and non-linear cases without residual stress. Energy release rate results have been extracted by the crack closure method using a one-phase analysis. Refinement of meshing is such that mode I energy release rates are converged to an average of 3.4% difference between successive meshes.

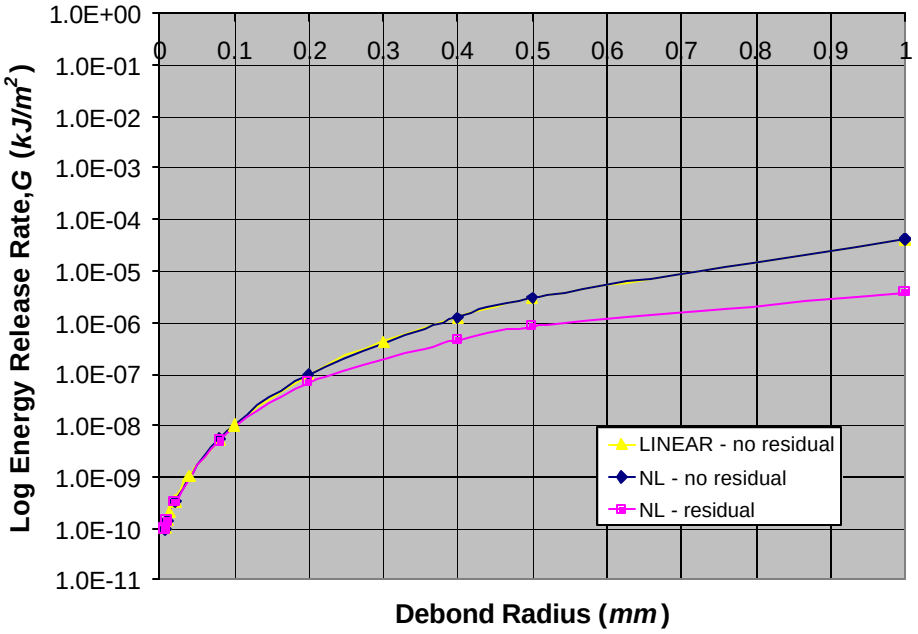

Figure 4.24. Effect on G_{total} of inclusion of residual stress in pressurized blisters

On a log scale, it is difficult to distinguish any differences between the linear and non-linear analyses without residual stress. However, the effect of inclusion of residual stress in the non-linear analysis is unmistakable. Residual stress induced by thermal strains effectively reduces G_I, G_{II}, and G_{total}. The percent reductions in available energy release rates achieved with inclusion of residual stress is plotted in Figure 4.25. Both modes experience the same trend in reduction. There is a steady climb in residual stress influence as the debond progresses. Note that pressurized blisters in the infinite medium range exhibit percent reductions of only 2-15%, whereas those in thin plate range exhibit 85-90% reduction.

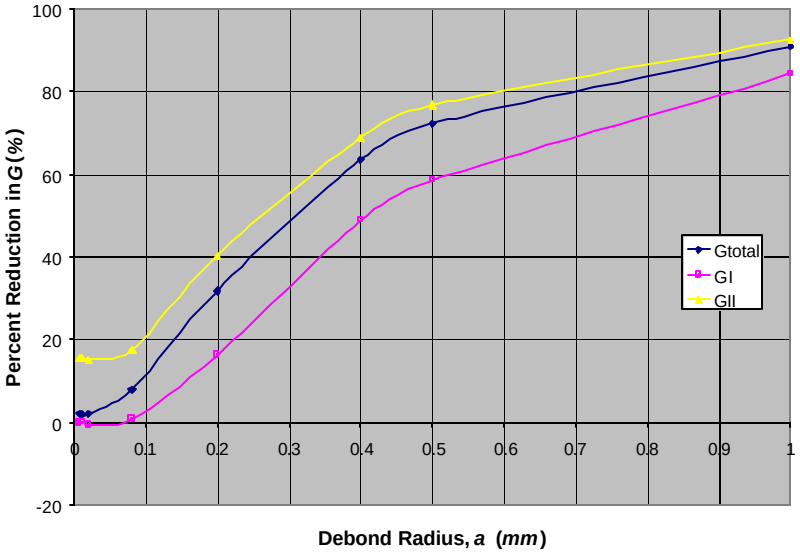

Figure 4.25. Percent reduction of *G* with exposure to residual stress

4.9 Mode Mixity

An important aspect of any fracture mechanics analysis is the mode mixity of available energy release rates. Mode mixity sheds light onto the dominating mode of failure present at a particular location in a system. The pressurized blister test involves both mode I and mode II failure types, which are constant along the blister circumference due to symmetry. Contributions to the energy release rate from mode III are non-existent in the pressurized blister due to the symmetry about the axis of revolution. The crack closure method of obtaining energy release rates has the ability to differentiate the different modes of fracture.

4.9.1 Linear, no residual stress

Figure 4.26 demonstrates the mode mixity results with a pressure of 0.01 *MPa* for both the axisymmetric and three-dimensional representations in the form of percent composition of total *G*, as defined by Eq. 4.37.

$$\%Mode_i = \frac{G_i}{G_{total}} \times 100 \tag{4.37}$$

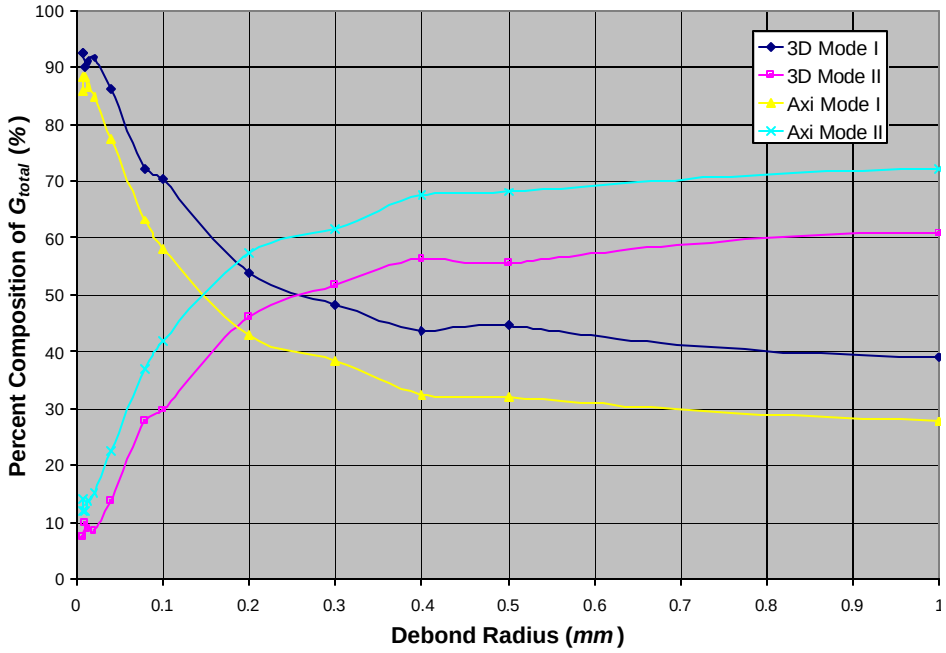

Figure 4.26. Mode composition of energy release rates for pressurized blister test

Figure 4.26 indicates that mode domination transitions from mode I domination at small debond radii to mode II domination at large debond radii. Focusing on the three-dimensional data curve, transition occurs at a debond radius of 0.25 *mm*, corresponding to an h/a=0.16. This is approximately six times the thickness of the specimen. Transition in axisymmetric representations occurs at a debond radius of 0.15 *mm*, an h/a=0.27. Both representations indicate that pressurized blisters approaching the infinite medium limiting case submit to more of a peeling effect, whereas pressurized blisters in the thin plate range experience more of a shearing type failure.

An additional representation of mode-mixity has been proposed by Jensen [27,34]. Jensen develops the mode mixity parameter, y, in order to give the near tip stress field, and defines it in terms of stress intensity factors,

$$\tan y = \frac{K_{II}}{K_I} \tag{4.38}$$

where stress intensity factors K_I and K_{II} for plane stress conditions are defined as,

$$K_I = \sqrt{\frac{G_I}{E}} \qquad K_{II} = \sqrt{\frac{G_{II}}{E}}. \tag{4.39}$$

Analysis of Eq. (4.38) shows that at an angle of 45°, mode I and mode II influence is equivalent. Pure mode I conditions occur at y=0°, and pure mode II conditions occur at

y=90°. According to Jensen's studies the critical stress intensity factor, or fracture toughness of an interface increases as y transitions from 0° to 90°. The results of Jensen's mode-mixity parameter, y, for the case of a pressurized blister under the same conditions as the blister of Figure 4.26 is presented in Figure 4.27.

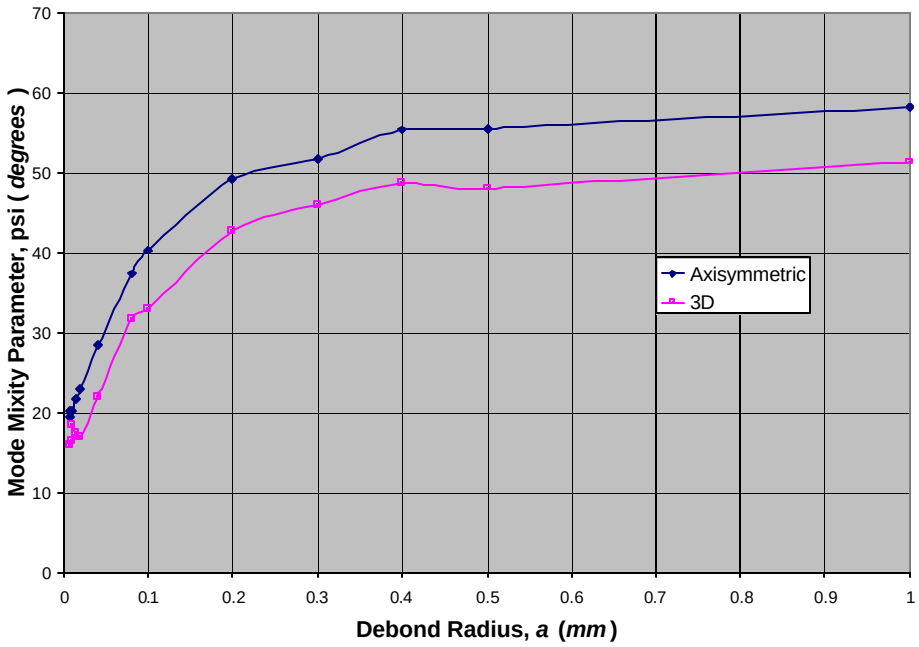

Figure 4.27. Mode mixity parameter for a pressurized blister

Figure 4.27 indicates that as the debond radius increases, mode-mixity transitions from mode I to mode II.

4.9.2 Non-linear, with residual stress

Figure 4.28 presents the mode-mixity results of the non-linear analysis of the pressurized blister test, with a pressure of 0.01*MPa*.

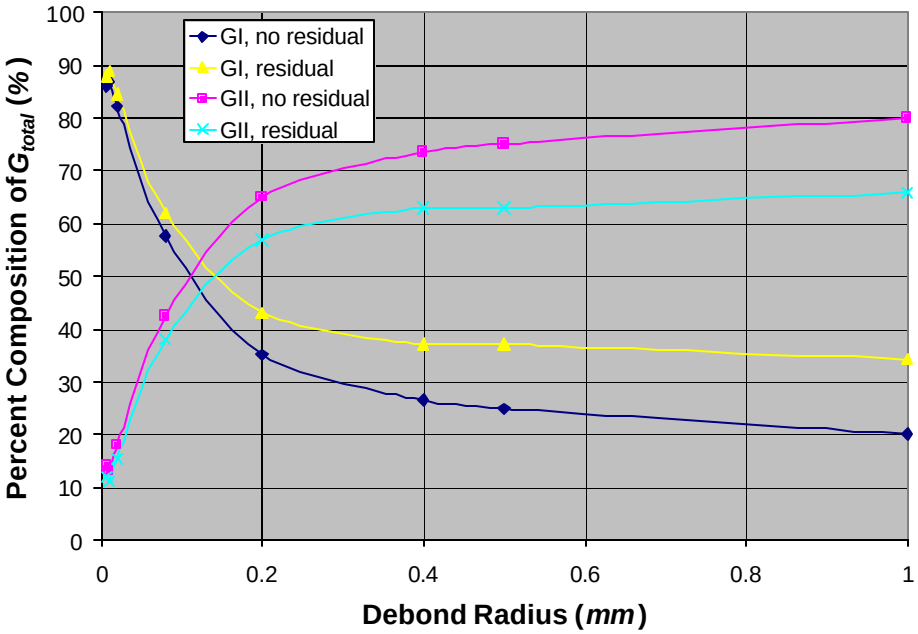

Figure 4.28. Mode-mixity results from non-linear analysis of pressurized blister test

Figure 4.28 indicates that addition of residual stress in the pressurized blister models increases the effect of G_I and proportionately reduces the effect of G_{II}. The effect is more prevalent as the extent of debonding increases. At a debond radius of 0.0067 *mm*, there is only a 2% difference in any particular mode composition with and without residual stress, but at a debond radius of 1 *mm*, the difference becomes nearly 15%.

Figure 4.29 presents mode-mixity in Jensen's y parameter format for the case of non-linear analysis with and without residual stress. This representation confirms the increasing effect of residual stress and the switch in mode dominance from I to II as the length of debond radius increases. The contributions of modes I and II are equivalent at a debond radius of 0.12 *mm* for the case without residual stress, and 0.15 *mm* with residual stress. Non-linear residual stress results reach equilibrium around 54° for large debonds, and around 19° for small debonds. Non-linear, non-residual results reach equilibrium around 63° for large debond radii, and around 22° for small debond radii.

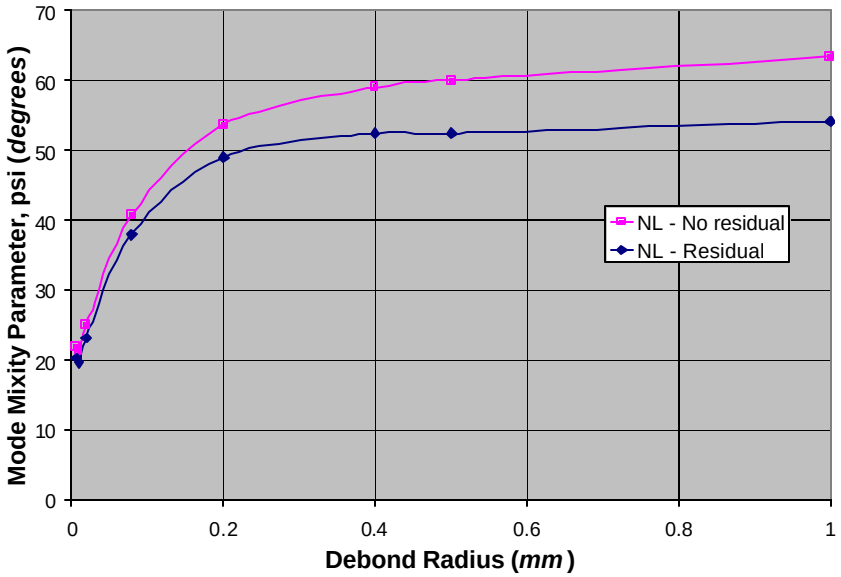

Figure 4.29. Mode mixity parameter, ψ, for a non-linear analysis with residual stress

4.10 Summary

This analysis of the pressurized blister test has established the limiting cases of thin plate theory and semi-infinite medium theory. Axisymmetric and three-dimensional finite element models were then developed and successfully correlated to theoretical results. The finite element results also successfully show that increasing the length of debond while holding the specimen thickness constant causes the behavior of the model to transition from an infinite medium to a thin plate, with these two bounds being the limiting conditions. The transition behavior established in the finite element models allows for expansion of the theoretical energy release rate equations through use of master curves to create an empirical model. The effect of residual stress on blister mechanics and ultimately blister energy release rates was thoroughly investigated. Residual stress was found to reduce both blister deflections and blister energy release rates, with more significant influence on large debond lengths rather than small. Finally, the mode-mixity of energy release rates in the pressurized blister was analyzed and found to transition from mode I dominance at small debond lengths to mode II dominance at large debond lengths. Residual stress was found to somewhat even out mode contributions, although the overall trend remains the same. The following chapter

investigates the shaft-loaded blister test in much the same manner as this chapter investigated the pressurized blister test. The shaft-loaded blister test will better represent the loading seen in the experimental probe test.

Chapter 5 Verification Model: Shaft-Loaded Blister Test

5.1 Overview

A second means of verifying both the mechanics of the finite element model and the energy release rate methods is modeling the shaft-loaded blister test. The shaft-loaded blister test consists of a thin circular film adhered to a rigid substrate, except for a central portion of radius a. When a rigid cylindrical punch is applied to the center of the non-adhered portion, the film lifts off the substrate, forming a blister. The blister radius remains fixed until a critical load, F_{cr}, is reached. At this load, the blister increases in size, indicating adhesive failure along the interface. Blister test behavior can be bounded by two extreme theoretical cases: thin plate theory associated with relatively large blister debond radii and semi-infinite medium theory associated with very small blister debond radii.

The objectives of finite element analysis of the shaft-loaded blister test are the same as the objectives behind the pressurized blister models. However, the shaft-loaded blister is a more valuable tool in this study because it more closely represents the loading conditions seen in the probe test. To briefly recapture the modeling objectives, the first objective is to accurately model the bounding extremes where thin plate and infinite medium theory apply. Correlation of blister finite element results to theory provides a basis for developing the analysis of the probe-loaded geometry. Secondly, it is to be experimentally shown that increasing the debond radius while holding the specimen thickness constant causes the behavior of the shaft-loaded blister to transition between the two limiting cases of an infinite medium and a thin plate. The third objective is to determine the sensitivity of the shaft-loaded blister to residual stress. The final objective of the finite element analysis is determination of the mode-mixity of energy release rates of the blister, which is important in understanding adhesive failure.

5.2 Shaft-loaded blister theory

5.2.1 Thin Plate

The limit case of thin plate theory in shaft-loaded blisters can be physically represented by large debond radii, a (mm), relative to specimen thickness, h (mm) (h/a=small). The shaft-loaded blister test with thin plate geometry is depicted in Figure 5.1.

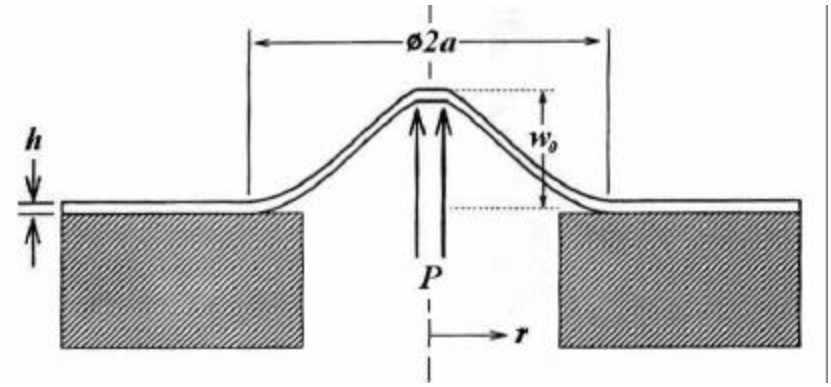

Figure 5.1. Schematic of a shaft-loaded thin plate blister

The following analysis develops an expression for the strain energy release rate, G (J/m^2), for the shaft-loaded blister in the limit case of thin plate theory. The analysis neglects residual stress, and assumes linear elastic material properties as well as small strain, small displacement theory. The development of G is based on the research of Malyshev and Salganik [35], M. L. Williams [25], Jensen [27], Wan and Mai [36], J. G. Williams [29], Wan and Liao [37], Wan [38], Wan, Guo and Dillard [39] and on personal discussions with Wan [12].

Derivation of the energy release rate for a shaft-loaded blister with thin plate theory begins with quantification of the elastic strain energy, $U_{elastic}$, in Eq. 5.1.

$$U_{elastic} = \int P dw_0 \tag{5.1}$$

Where P is the applied load (N) from the rigid punch, and w_0 is the central displacement (mm) caused by this load. Assuming linear elasticity, Timoshenko's clamped circular plate loaded at the center [25] provides the axisymmetric displacement field $w(r)$ (mm),

$$w(r) = \frac{3\,\mathrm{Pr}^2}{2pE'h^3}\log\frac{r}{a} + \frac{3P}{4pE'h^3}(a^2 - r^2) \tag{5.2}$$

from which the central displacement, w_0, can be derived as in Eq 5.3,

$$w_0 = \frac{3Pa^2}{4\pi E' h^3}. \tag{5.3}$$

In Eq. 5.2 and 5.3, $E' = E/(1-\nu^2)$ (*MPa*), a is the debond radius (*mm*), r is the variable radius (*mm*), and h the specimen thickness (*mm*). Rearranging Eq. (5.3) to solve for P, and returning to Eq. (5.1), the elastic energy stored in the blister is,

$$U_{elastic} = \frac{1}{2} P w_0 = \frac{3P^2 a^2}{8\pi E' h^3}. \tag{5.4}$$

$$U_{elastic} = \int \frac{4\pi E' h^3}{3a^2} w_0 dw_0$$

The energy release rate is the change in stored elastic strain energy with respect to change in area, dA, due to the creation of new surface areas by crack advance,

$$G = \frac{dU_{elastic}}{dA}.$$

But $A=\pi a^2$ => $dA/da=2\pi a$ => $dA=2\pi a da$. This leads to

$$G = \frac{dU_{elastic}}{da}\frac{da}{dA} = \left(\frac{dU_{elastic}}{da}\right)\left(\frac{1}{2\pi a}\right). \tag{5.5}$$

Substituting Eq. (5.4) into Eq. (5.5) and differentiating yields Eq. 5.6.

$$G = \frac{3P^2}{8\pi E' h^3} \tag{5.6}$$

The available energy release rate, G, for a shaft-loaded blister can be written in terms of the applied load and the maximum deflection at the center of the blister, Eq. (5.3), giving the simpler form of Eq. (5.7). [35]

$$\boxed{G = \frac{P w_o}{2a^2 \pi}} \tag{5.7}$$

5.2.2 Semi-infinite medium

The limiting case of semi-infinite medium theory in shaft-loaded blisters can be physically represented by small debond radii relative to specimen thickness (h/a=large). The shaft-loaded blister test with semi-infinite geometry is depicted in Figure 5.2.

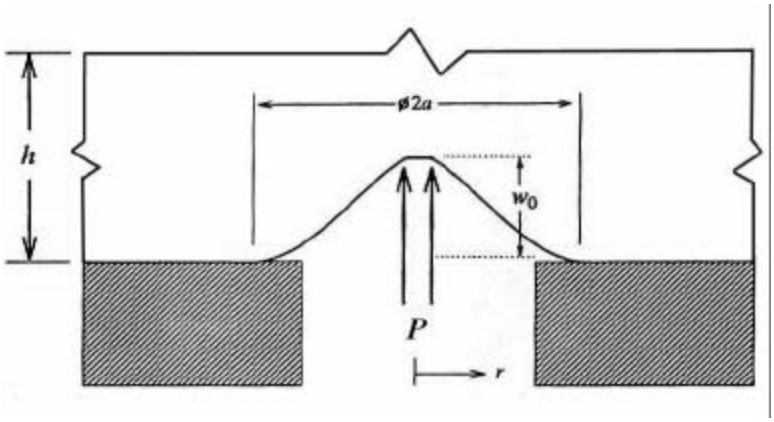

Figure 5.2. Schematic of a shaft-loaded infinite medium blister

An expression for the energy release rate of a shaft-loaded blister in the limit case of infinite medium theory was unable to be developed in this work. Analytical expressions for the profile of a shaft-loaded infinite medium were sought in Sneddon [33] and Johnson [40] (Boussinesq solution of point loading in an elastic half-space), but adequate expressions were not acquired. The finite element analysis performed in this work should shed light on this problem.

5.3 Finite element model development

Much like the pressurized blister test, the shaft-loaded blister test has been modeled using both three-dimensional and axisymmetric finite element models. Axisymmetric models are fully capable of handling the blister test and are the standard model for this analysis. However, three-dimensional models are also developed because the geometry of the edge model in Chapter 6 can only be captured by a three-dimensional representation. Three-dimensional linear elasticity with small deformations is exact and three-dimensional models impose no additional theoretical constraints beyond their linear or quadratic interpolation functions. Therefore three-dimensional models contain more modeling potential than axisymmetric models, but the ability of axisymmetric models to capture three-dimensional space with two-dimensional mechanics make axisymmetric models

more efficient. Due to this gained efficiency, the majority of analyses in this work make use of axisymmetric models rather than three-dimensional models. In certain cases three-dimensional results will be compared to axisymmetric results to ensure that the three-dimensional models and methodologies provide accurate solutions. Unless otherwise specified, the material properties and modeling specifics used throughout this work are listed in Table 5.1.

Table 5.1 Listing of symbols and values for material properties

Property	Symbol	Value
Modulus of elasticity	E	3.4 *GPa*
Poisson's ratio	ν	0.32
Thickness	h	0.04 *mm*
Debond	a	variable
Net coefficient of thermal expansion	α_{film}-$\alpha_{substrate}$	85E-6 *mm*/(*mm*°C)
Stress free temperature	*SFT*	175 °C
Operating temperature	T	20 °C
Shaft radius	s	0.01 *mm*
Prescribed displacement	w_o	0.002 *mm*

5.3.1 Three-dimensional solid model

Figure 5.3 displays the geometry developed for the three-dimensional shaft-loaded blister model. The edge denoted A is a plane of symmetry for the shaft-loaded blister test, and is the boundary condition removed for the edge-loaded model. This thesis uses a quarter circular model because the plane denoted B is the only symmetry plane for the edge-loaded geometry to be analyzed in Chapter 6.

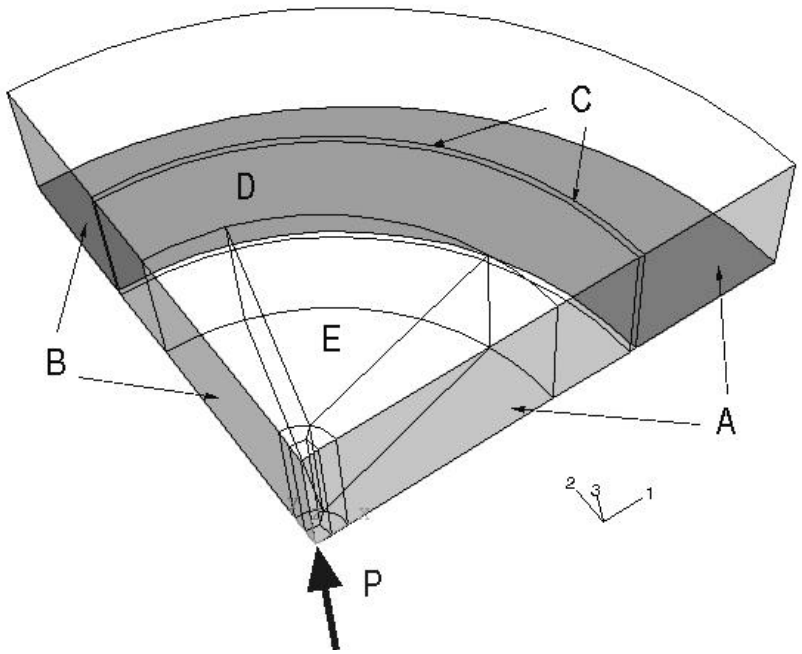

Figure 5.3. Schematic of three-dimensional shaft-loaded blister

In Figure 5.3, plane A has symmetry conditions, u_2=0. Plane B has symmetry conditions, u_1=0. The volume pointed out by C is a partition that is one element wide to facilitate determination of energy release rates, which will be described in detail in Section 6.3. The radius at which the partition of C exists is the assumed extent of debond for the model. Section D points to the bottom surface of the film. This region is sufficiently large to negate any effects caused by the truncation of geometry at the model's edge. The entire area of D is prescribed as encastre, meaning all nodes are constrained in all degrees of freedom (u_1=u_2=u_3=0). This boundary condition is representative of intact adhesion to a rigid substrate beyond the area of debond. The volume designated E is a meshing zone created for two reasons. The first reason is to allow the mesh to even out before reaching partition C, which is where data will be queried. The second reason is to diminish the number of elements spanning the arc near the point of load application so as to avoid mesh distortion. Loading is applied by prescribed displacements on a small quarter-circular area to represent the displacement effects of the point load, *P*.

Having been qualified in *Chapter 3 Element Selection*, reduced integration brick elements (C3D8R) are used for three-dimensional models of the shaft-loaded blister. Figure 5.4 demonstrates a typical deformed three-dimensional mesh. The mesh is refined towards the edge of debond (radius *a*) from both directions to capture the singularity caused by

stress concentrations at the boundary change. Capturing the singularity is important because determination of energy release results occurs at this location. Overall mesh refinement of three-dimensional models is such that strain energy, U, of the model is converged to 0.03% between meshes, calculated as,

$$PercentConvergence = \left| \frac{U_{refined} - U_{coarse}}{U_{coarse}} \right| \times 100. \tag{5.8}$$

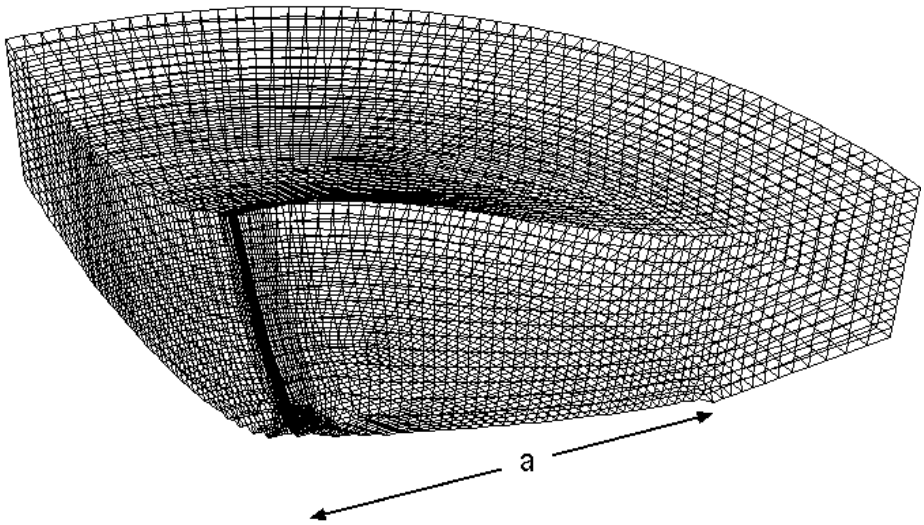

Figure 5.4. Typical mesh scheme for three-dimensional shaft-loaded blister

5.3.2 Axisymmetric model

The axisymmetric model of the shaft-loaded blister test is a two-dimensional simplification of the three-dimensional model of Figure 5.3. Imagine slicing the three-dimensional model radially with a straight edge, and viewing the slice perpendicular to its face. This results in the axisymmetric configuration shown in Figure 5.5.

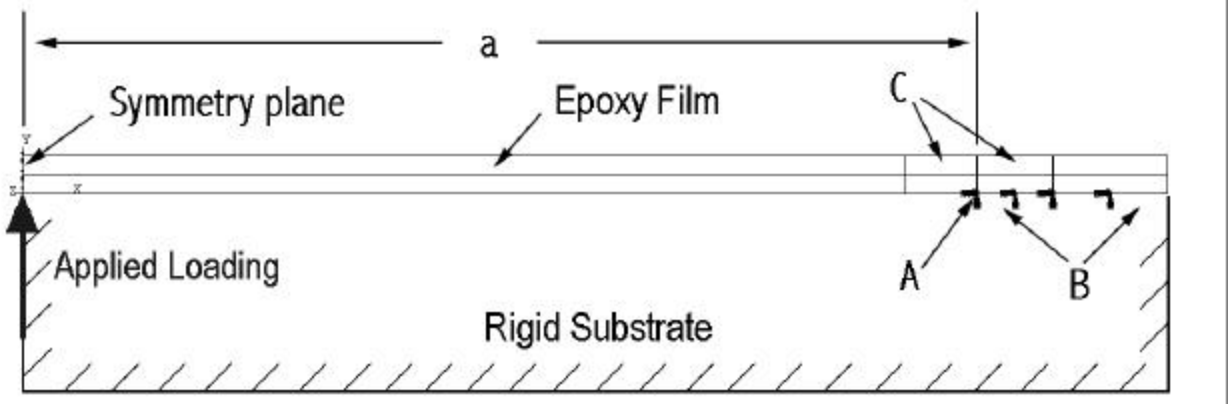

Figure 5.5. Schematic of axisymmetric finite element model setup for shaft-loaded blister

The symmetry plane by which the model is revolved is denoted to the left. The debond length, *a*, is a parameter increased from model to model to simulate crack growth. Point A represents the extent of debond, and region B the simulated adherence to the right. The length of the adhered area in region B is sufficient to ensure there are no effects from the truncated geometry. In reality, the material would continue past region B to the end of the specimen. The adherence of the film to the substrate is captured in a fully restrained boundary condition, $u_1=u_2=q_3=0$. Applied shaft loading is denoted to the left of the schematic. The areas indicated by C are zones of mesh refinement, meant to capture the singularity at the extent of debond. Again, meshes are highly refined near the extent of debond (point A) in order to capture the singularity and to acquire accurate energy release rates. Mesh refinement of the axisymmetric model converges the strain energy of the model to 0.05% difference between meshes, as calculated in Eq. 5.8. Axisymmetric shaft-loaded blister models use first order, reduced integration, quadrilateral elements (CAX4R) as selected in *Chapter 3 Element Selection*. Figure 5.6 presents a typical deformed axisymmetric mesh with a small crack length, *a*. In this figure it is evident that a portion of mesh 0.01 *mm* wide has been prescribed with the 0.002 *mm* displacement, to represent the shaft width.

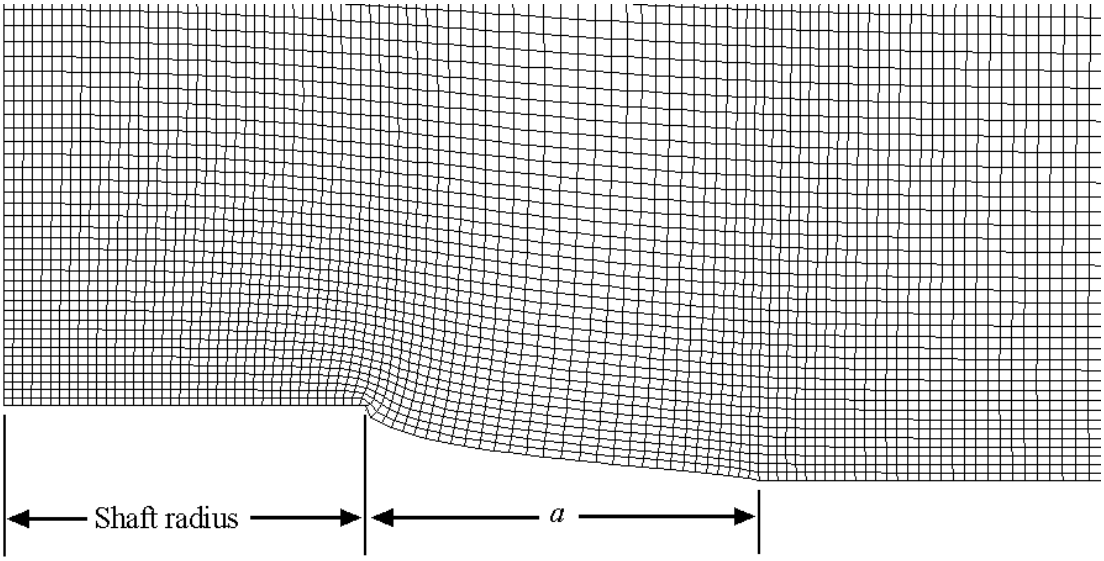

Figure 5.6 Typical mesh scheme for axisymmetric shaft-loaded blister models

5.4 Energy release rate extraction

The method of energy release rate extraction for the shaft-loaded blister model precisely follows the method for obtaining energy release rates for the pressurized blister test, as described in Chapter 4, Section 4.5.2 and 4.5.3.

5.5 Confirmation of deformation mechanics

Having established the limiting case of thin plate theory and developed the finite element structure for the shaft-loaded blister test, results can be analyzed in detail. The following section compares displacement profiles from finite element models to profiles from thin plate theory. This comparison will ensure that the finite element models are correctly capturing the deformation mechanics of blister testing. Although a theoretical expression for blister profiles in the semi-infinite range has not been developed, models with successively smaller debonds should indicate a convergence trend in G, thereby indicating the presence of semi-infinite medium behavior. This behavior is demonstrated in this chapter's transition from an infinite medium to a thin plate, Section 5.6.

5.5.1 Thin plate

Figure 5.7 compares finite element results and theoretical displacement profiles for the thin plate model with a debond radius of 2 *mm* and central loading of 0.01 *mm*. Since Timoshenko's plate theory assumes all displacements occur at the mid-surface, the displacement profiles of the continuum finite element models were also obtained from the model mid-surface.

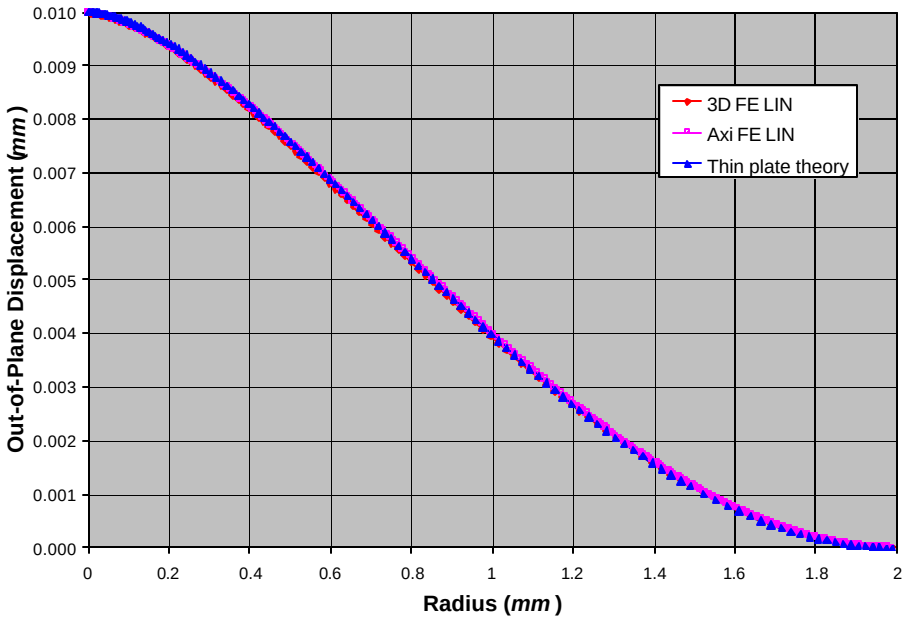

Figure 5.7. Comparison of finite element and thin plate theory profiles at a debond radius of 2 *mm*

Figure 5.7 indicates strong correlation between finite element approximations and theory. A similar statistical analysis to the analysis described in Section 4.6.1 gives an understanding of the degree of correlation between theory and finite element models. The singularity effect at the debond front caused by a change in boundary constraints is described by St. Venant's principle. This singularity zone compromises approximately five percent of the data near the extent of the debond. The results from this singularity zone have been eliminated from the study because distortion of elements in this area leads to inaccurate results that are not seen in the analytical result. The results from the truncated deflection data appear in Table 5.2.

Table 5.2. Statistical comparison of finite element results to thin plate theory

Statistic	3D FE Solution	Axi FE Solution
Standard Deviation	2.583E-05	1.663E-05
Signal to Noise Ratio (*SNR*)	387.1	601.2

The results in Table 5.2 show that both finite element solutions produce high signal to noise ratios, indicating strong correlation to theory. However, the axisymmetric finite element solution shows much stronger correlation to theory than the 3-D solution. This characteristic is consistent with intuition since the axisymmetric model shares a constraint with thin plate theory eliminating any dependence of the mechanics on the circumferential direction displacments. The 3-D model discretely approximates this constraint.

5.5.2 Inclusion of residual stress

Residual stress has only been included in axisymmetric finite element models by the use of thermal mismatch, as explained in section 4.4.2. Numerical quantities for parameters are given in Table 5.1.

5.5.2.1 Linear analysis

Drawing from the experience gained in the pressurized blister test, linear analyses have been assumed to be unable to capture the effects of residual stress in the shaft-loaded blister test. Therefore residual stress is only included in non-linear analyses.

5.5.2.2 Non-linear analysis

As in the pressurized blister, the shaft-loaded blister requires a sufficient amount of material behind the extent of debond so as to not curtail the effects of residual stress. To determine the amount of material required, the material beyond debond was increased incrementally, and the midsurface profiles of each increment are plotted together on the same graph. The results for a 1 *mm* debond radius case loaded by a prescribed central displacement of 0.01 *mm* can be found in Figure 5.8.

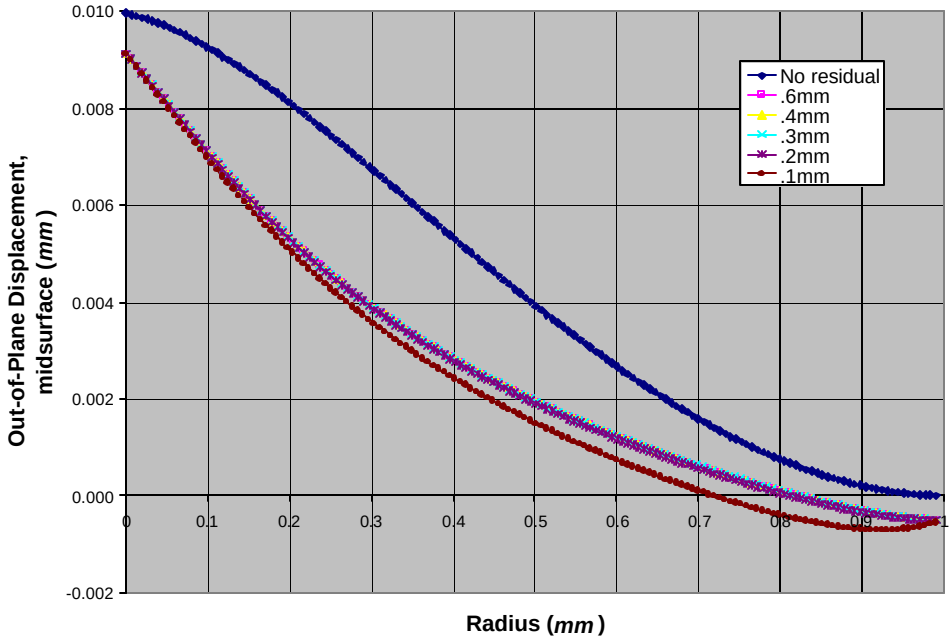

Figure 5.8. Effect of adhered material behind debond – NONLINEAR ANALYSIS

Figure 5.8 indicates that non-linear analyses of residual stress in the shaft-loaded blister test successfully capture a decrease in deflection profile. Residual stress in the film effectively introduces in-plane tensile strains to the blister, thereby reducing out-of-plane deflections when the same loading is applied. Figure 5.8 also demonstrates that the amount of adhered material behind the extent of debond has a significant effect on the profile. This significance is captured in Figure 5.9, which shows convergence of deflection at a debond radius of 0.7 *mm* with varying amounts of additional adhered material.

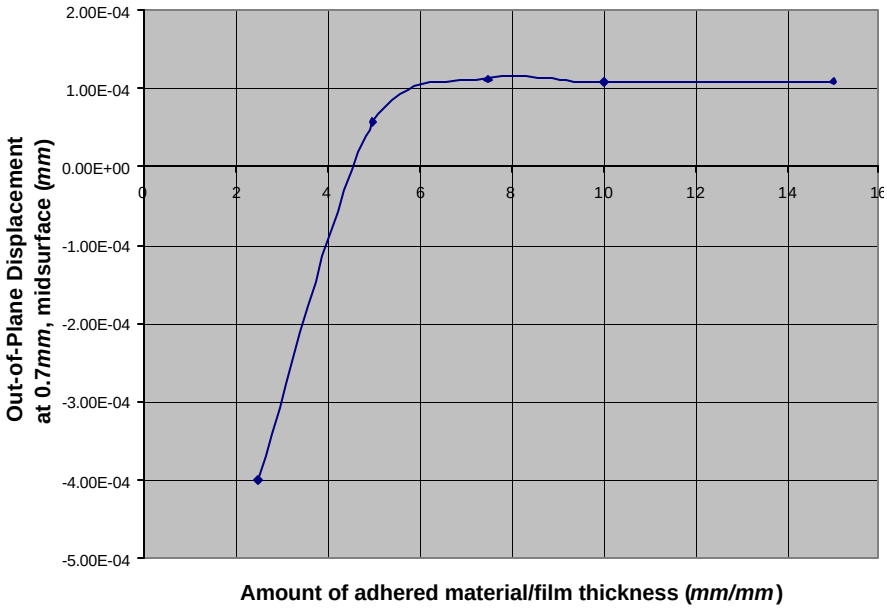

Figure 5.9. Convergence of deflection at a debond radius of 0.7*mm* with varying amounts of adhered material

Figure 5.9 shows that convergence of midsurface deflections at a debond radius of 0.7 *mm* doesn't occur for models with residual stress until the amount of adhered material is nearly 10 times the film thickness. On the other hand, for models without residual stress the deflection at a radius of 0.7 *mm* changes only 0.2% as the amount of adhered material is increased from 0.1*mm* to an amount of 0.6 *mm*. All shaft-loaded blister models used in this work contain sufficient material behind the debond so as to converge the effects of residual stress. Assuming the same guidelines apply, the amount of adhered material beyondthe debond is based on the amount required by the pressurized blister test, as listed in Table 4.4.

5.6 Transitioning from an infinite medium to a thin plate

Following the methodology set forth by Bennett, et al [13], for the pressurized blister test, linear analyses have been performed to confirm the transition of shaft-loaded blister behavior from infinite medium theory to thin plate theory. Bennett, et al, varied specimen thickness, but this work varies debond radius and holds specimen thickness constant, thereby creating the same effect. The analysis was repeated for discrete specimen debond radii ranging from 0.02 *mm* to 1 *mm* (*h/a*=2 to 0.04). Throughout all

analyses, the film thickness, *h*, is held to 0.04 *mm*. Having seen minimal difference in non-linear and linear results in the analysis of the pressurized blister without residual stress, axisymmetric transition data for the shaft-loaded blister test is based on non-linear geometry. The material definition remains linear elastic.

The energy release rate results of both three dimensional and axisymmetric models by the modified crack closure method are presented in Figure 5.10 against thin plate theory.

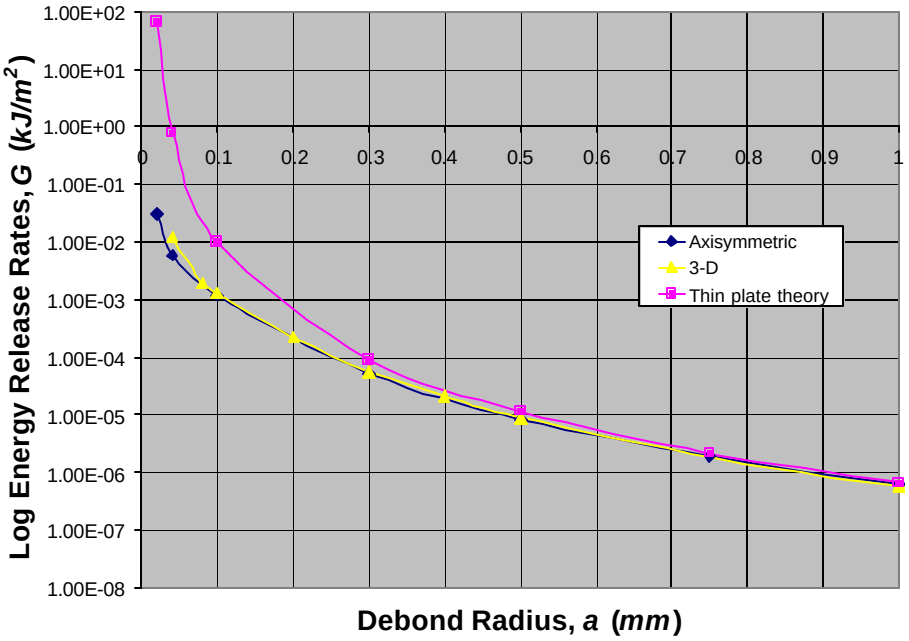

Figure 5.10. Energy release rate results of shaft-loaded blister without residual stress

In Figure 5.10 it is clearly evident that both the three-dimensional model and the axisymmetric model converge towards thin plate theory as the debond radius increases. Refinement of meshing to produce these results was such that the mode I energy release rates of the model are converged to within 6%. The data can be presented in normalized energy release rate form as,

$$Normalized G_{total} = \frac{G_{total} a^2}{F w_0} \tag{5.9}$$

Acquiring the force associated with the prescribed displacement in the three-dimensional models proved to be too difficult a task. Reaction forces had to be hand queried from all nodes with prescribed displacements, which is far more intensive for three-dimensional models than for axisymmetric models. Therefore only axisymmetric model data will be

presented in this form. Figure 5.11 plots the normalized energy release rate versus the thickness to span ratio of the shaft-loaded blisters.

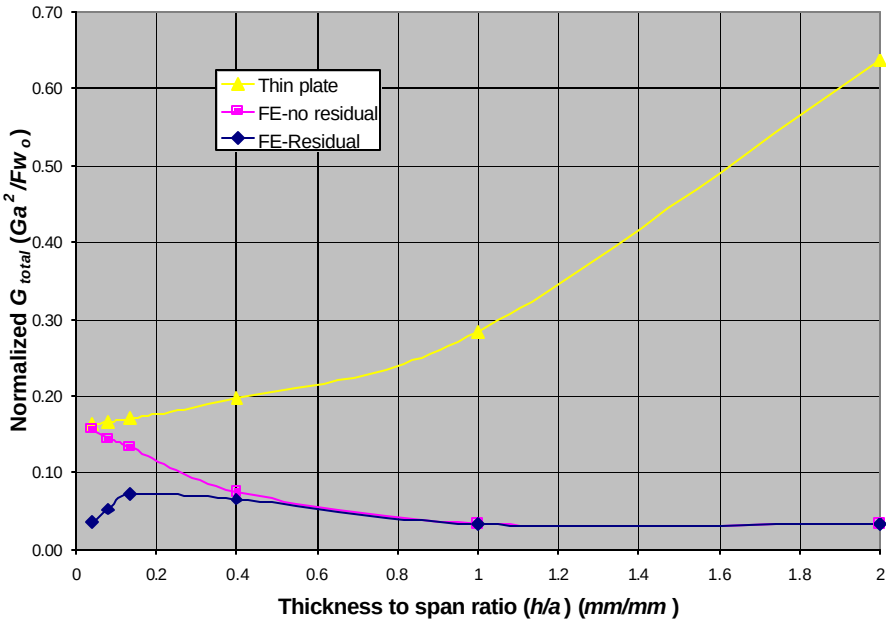

Figure 5.11. Comparison of normalized energy release rates

Again, Figure 5.11 indicates that the finite element data without residual stress converges to thin plate theory at small *h/a* ratios (large debond radii). The same finite element curve then converges to a normalized G_{total} value of 0.033 at large *h/a* ratios (small debond radii), in what would be semi-infinite medium range. Further analysis and examination of variables such as film thickness in the shaft-loaded blister test could potentially help develop an expression for *G* in semi-infinite medium range. The data in the current analysis alone is not sufficient to specify an expression.

Figure 5.11 also indicates that as the radius of debond decreases, the effect of residual stress decreases, and the residual stress curve begins to coincide with the non-residual stress curve. This trend occurs at an *h/a*=1, meaning the debond radius equals the film thickness.

5.7 Energy release rates with residual stress

Inclusion of residual stress in non-linear analyses of the shaft-loaded blister test has already been shown to reduce deflections as in Figure 5.8, as well as alter energy release

rates as shown in Figure 5.11. Figure 5.12 below presents total energy release rates with and without residual stress on a log scale. Figure 5.13 accentuates the degree to which residual stress influences G_{total}, G_I, and G_{II} in a plot of percent reduction in G caused by inclusion of residual stress.

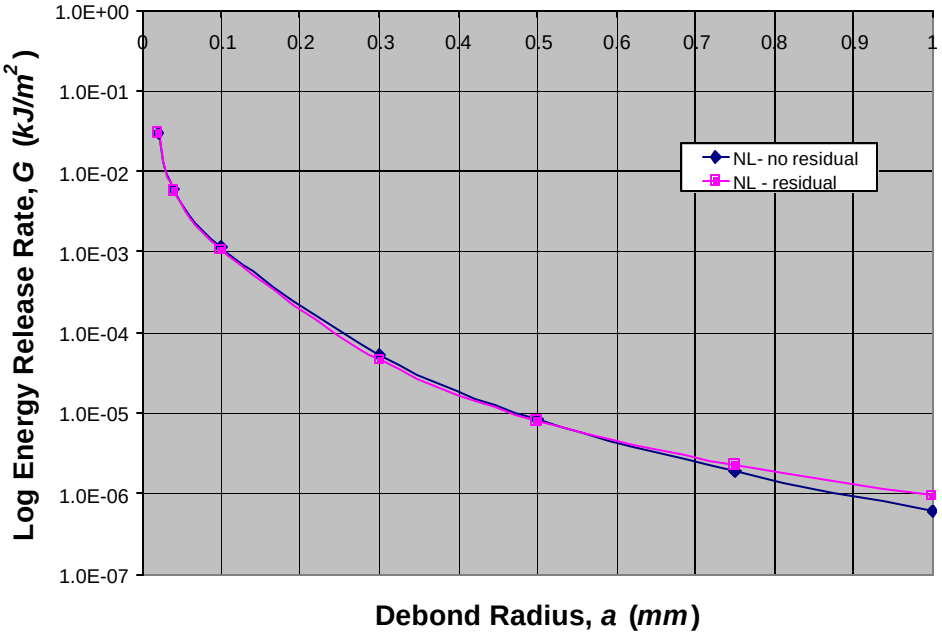

Figure 5.12. Effect on G_{total} of inclusion of residual stress in shaft-loaded blisters

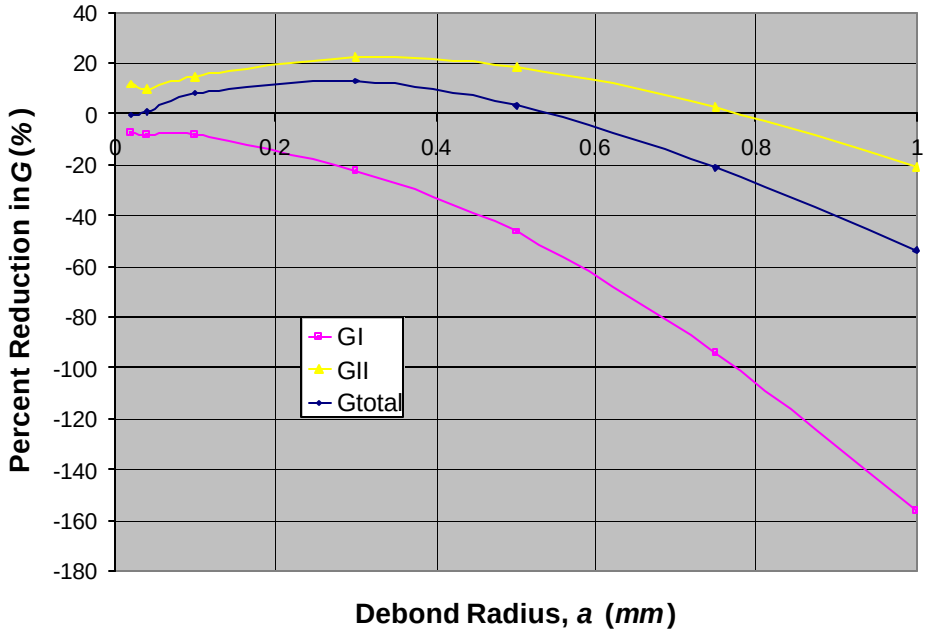

Figure 5.13. Percent reduction of G with exposure to residual stress

Figure 5.13 indicates that at very small debond radii, residual stress has less than a +1% effect on the total available energy release rate of the blister. As the debond radius increases to 0.3 *mm*, residual stress reduces G_{total} by a maximum of -12%, and then as the debond radius increases past 0.3 *mm*, the negative effects of residual stress begin to fade. At a 0.54 *mm* debond radius, residual stress has no impact on G_{total}, but beyond this debond radius, residual stress increases G_{total}. At a debond radius of 1 *mm*, residual stress has increased total energy release rates by +54%.

Figure 5.13 also indicates that residual stress minimally increases G_I at small debond radii (+7% at 0.02*mm*), but greatly augments its influence as the radius of debond progresses (+156% at 1*mm*).

On the other hand, residual stress causes G_{II} to decrease until the debond radius reaches approximately 0.78 *mm* at which point residual stress causes G_{II} to increase. Initial reduction in G_{II} is about -10%, and the percent increase in G_{II} at a large debond radius of 1 *mm* is +20%. A maximum decrease of -22% reduction occurs at a debond radius of 0.3 *mm*.

Possible reasons for the trends caused by residual stress in the shaft-loaded blister are given in *Section 5.8 Mode Mixity.*

5.8 Mode Mixity

An important aspect of any fracture mechanics analysis is the mode mixity of available energy release rates. Mode mixity sheds light onto the dominating mode of failure present at a particular location in a system. The shaft-loaded blister test is susceptible to both mode I and mode II failure types, which are constant along the blister circumference due to symmetry. Contributions to the energy release rate from mode III are non-existent in the shaft-loaded blister because of symmetry about the axis of revolution. As previously stated and explained in Section 2.3.3 and Section 4.5, the crack closure method of obtaining energy release rates has the ability to differentiate the different modes of fracture.

Focusing on axisymmetric non-linear results, Figure 5.14 demonstrates the mode mixity results in the form of percent composition of total G, as defined by,

$$\%Mode_i = \frac{G_i}{G_{total}} \times 100. \tag{5.9}$$

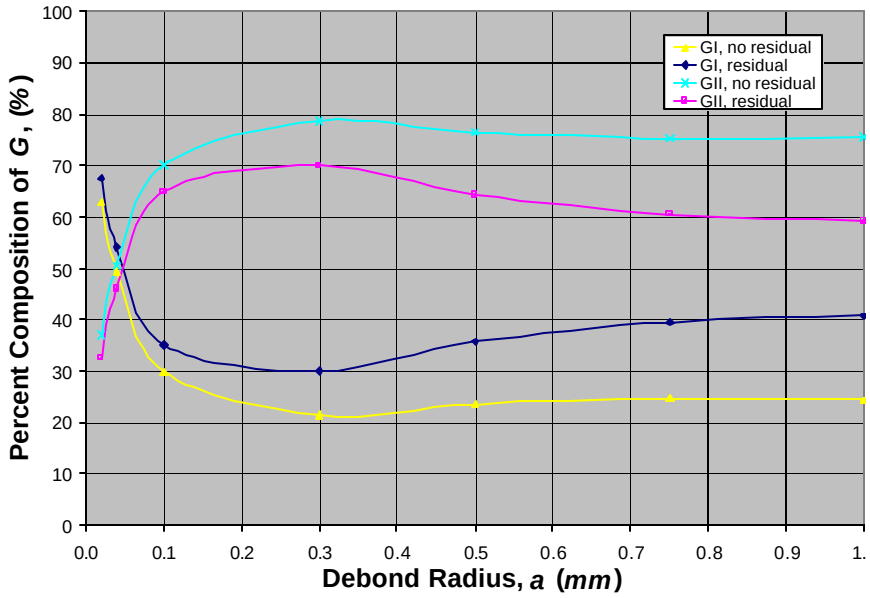

Figure 5.14. Mode composition of energy release rates for shaft-loaded blister test

Figure 5.14 indicates that mode domination transitions from mode I domination at small debond radii to mode II domination at large debond radii. Crossover of modes occurs at a debond radius of approximately 0.04 *mm* (*h/a*=1) for blisters without residual stress and a debond radius of 0.05 *mm* (*h/a*=0.8) for blisters with residual stress. After this point, residual stress causes greater mode I composition and lesser mode II composition than blisters without residual stress. Both models experience respective mode maximums and minimums around a 0.3 *mm* radius of debond.

Having gained insight into the effects of residual stress on mode-mixity, the energy release rate trends of *Section 5.7 Energy release rates with residual stress* can be further analyzed.

The fluctuation of the residual G_{total} curve in Figure 5.12 about the non-residual G_{total} curve is an artifact of mode mixity. Initially, G_{total} is unaffected by residual stress, because residual stress has opposing effects on mode I and mode II. Thereby, the two residual effects cancel each other out. As the radius of debond progresses, mode II achieves dominance of nearly 70/30, and in the range of debond radii from 0.04*mm* to 0.78*mm*, residual stress reduces G_{II}. Therefore the initial overall effect on G_{total} is reduction, even though residual stress significantly increases G_I throughout this range of debond radii. At a debond radius of 0.54*mm*, the increase in G_I outweighs the reductions

from G_{II}. Therefore residual stress begins to increase G_{total}. Beyond a radius of 0.78*mm*, residual stress increases G_{II} as well as G_I, so residual stress significantly increases G_{total} for large debond radii. Table 5.3 summarizes the effects of residual stress by mode and in total.

Table 5.3. Breakdown of residual stress effect on G

a	**0-0.25*mm***	**0.25-0.5*mm***	**0.5-0.75*mm***	**0.75-1*mm***
h/a	**>0.16**	**0.16-0.08**	**0.08-0.053**	**0.053-0.04**
G_I	+	+	+	+
G_{II}	-	-	-	+
G_{total}	-	-	+	+

key: (+) increase (-) decrease

5.9 Chapter summary

This analysis of the shaft-loaded blister test has established the limiting case of thin plate theory. Axisymmetric and three-dimensional finite element models were then developed and successfully correlated to thin plate theory and also shown to converge to a particular value in semi-infinite medium range. Thereby, the finite element results show that increasing the debond radius while holding the specimen thickness constant causes the behavior of the model to transition from an infinite medium to a thin plate, with these two bounds being the limiting conditions. The effects of residual stress on blister mechanics and ultimately blister energy release rates were thoroughly investigated. Under the specific conditions listed in Table 5.1, residual stress decreased G_{total} at small debond radii, and increased G_{total} at large debond radii. Regardless of length of debond radius, residual stress increased G_I. G_{II} on the other hand, decreased with residual stress at debond radii less than 0.8 *mm*, but increased beyond that length. Finally, the mode-mixity of energy release rates in the shaft-loaded blister were analyzed and found to transition from mode I dominance at very small debond radii to mode II dominance at large debond radii. Residual stress was found to have more influence on mode-mixity at larger debond radii, and influenced modes I and II inversely.

With these results and the results of the pressurized blister test, a strong basis has been developed upon which an analysis of the new probe test can be built.

Chapter 6 Edge-Loading of a Thin Film

6.1 Overview

This chapter explores the target geometry of the thesis, a thin film with out-of-plane cylindrical punch loading at its edge. As mentioned in Chapter 1, this geometry was derived from experimental probe testing that was developed to investigate failure of adhesion between microelectronic coatings and substrates under adverse operating environments. Loading in the probe test is by a cylindrical shaft at a 45° angle to the edge interface of the coating and substrate. This mechanical loading is intended to simulate accelerated delamination at the edge of the coating by environmental conditions such as fluctuating temperature fields and chemical exposure. The test captures the energies associated with delamination based on calculations from the interference fringes developed by loading and from the final deformed shape. An overhead view of this setup and the resulting delamination pattern is pictured in Figure 6.1.

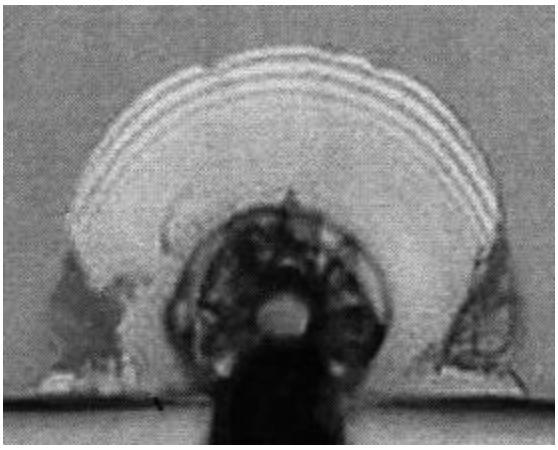

Figure 6.1. Experimental probe test

The delamination pattern in Figure 6.1 is characterized by shearing or tearing at the sides around 15-17° and uniform semi-circular delamination in front of the probe tip. A series of photos showing progressive delamination of the coating can be found in Appendix B. The goal of the work of this chapter is to gain insight into the underlying mechanics driving the delamination experienced by the coating. The loading of the probe test is both out-of-plane and in-plane loading, resulting in wedging and buckling effects, respectively. Based on the fact that thin films are much stiffer in-plane than out-of-plane,

it is assumed that out-of-plane displacement, or wedging, dominates failure. The finite element analyses for the probe test in this chapter therefore focus only upon the wedging (out-of-plane) mechanism of failure. Investigation of buckling would require an entirely separate linear perturbation eigenvalue analysis to estimate critical loads, which has not been undertaken.

The work contained in this chapter builds off of the validated finite element and fracture mechanics techniques developed in Chapters 2, 3, 4, and 5. There are four objectives behind this finite element analysis of edge loaded thin films.

- Develop a numerical technique for characterizing energy release rates at various points about an assumed debond front. Unlike the blister testing of Chapters 4 and 5, the geometry pictured in Figure 6.1 does not have energy release rates that are independent of theta.
- Investigate energy release rate sensitivity to residual stress in the thin film.
- Determine the impact of length of debond radius on energy release rates.
- Analyze results to ascertain reasons for trends seen in experimental testing

6.2 Finite element model development

Due to the complex geometry and boundary conditions of the edge loaded thin film model, three-dimensional finite element models must be developed. Unless otherwise specified, the material properties and modeling specifics used throughout this work are listed in Table 6.1.

Table 6.1. Listing of symbols and values for material properties

Property	Symbol	Value
Modulus of elasticity	E	3.4 *GPa*
Poisson's ratio	ν	0.32
Thickness	h	0.04 *mm*
Debond radius	a	variable
Net coefficient of thermal expansion	α_{film}-$\alpha_{substrate}$	85E-6 *mm*/(*mm*$^{\circ}$C)
Stress free temperature	*SFT*	175 $^{\circ}$C
Operating temperature	T	20 $^{\circ}$C
Shaft radius	s	0.01 *mm*
Prescribed displacement	w_o	0.002 *mm*

Figure 6.2 is a graphical representation of the full test setup used to capture the wedging (out-of-plane) mechanism of failure. The entire coating shown in the figure is adhered to an imaginary substrate except for a small, semi-circular, central portion.

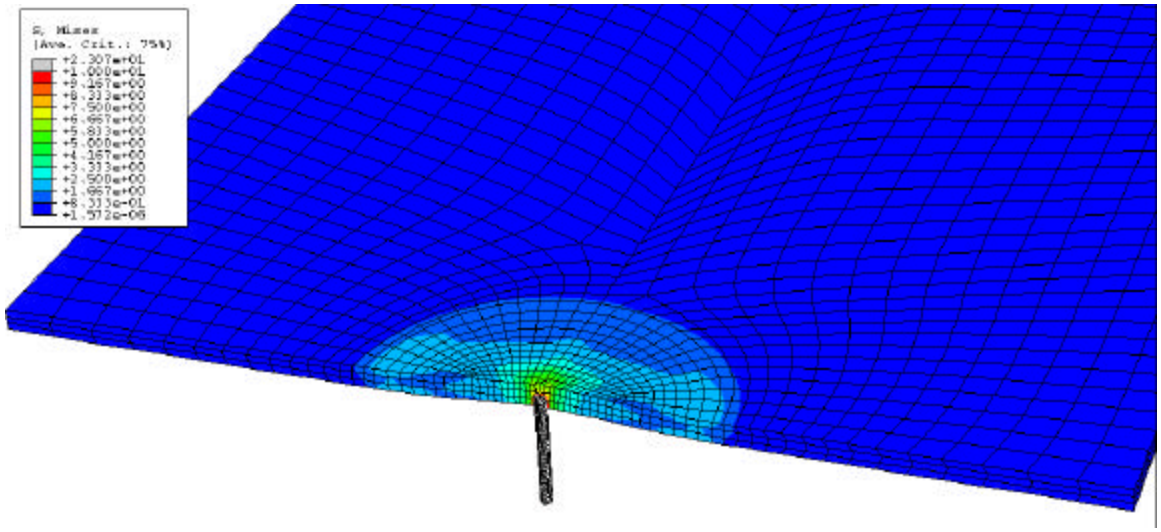

Figure 6.2. Graphical representation of von Mises stresses of an edge-loaded thin film

The working finite element model used for data extraction is pictured in Figure 6.3. The model takes advantage of the symmetry plane, denoted B, that divides the semi-circular blister of Figure 6.2. The only difference between this model and the model for the shaft-loaded blister test of Chapter 5 is the presence of a free edge, denoted A, which will significantly affect energy release rates of the film. Section C of Figure 6.3 is a subdivided volume used to facilitate acquisition of energy release rates, as will be explained in Section 6.3. Letter D points to the darkly shaded section at the bottom surface of the thin film that is restrained in all degrees of freedom, $u_1=u_2=u_3=0$, to represent intact adhesion behind the debond front. Volume E is a mesh reduction zone, intended to transition the meshing scheme about volume C to the meshing scheme about the applied loading. To represent probe loading, vertical loading at the film's edge is applied by prescribing a displacement over a 0.01 *mm* radius quarter-circle at the bottom surface of the model as indicated.

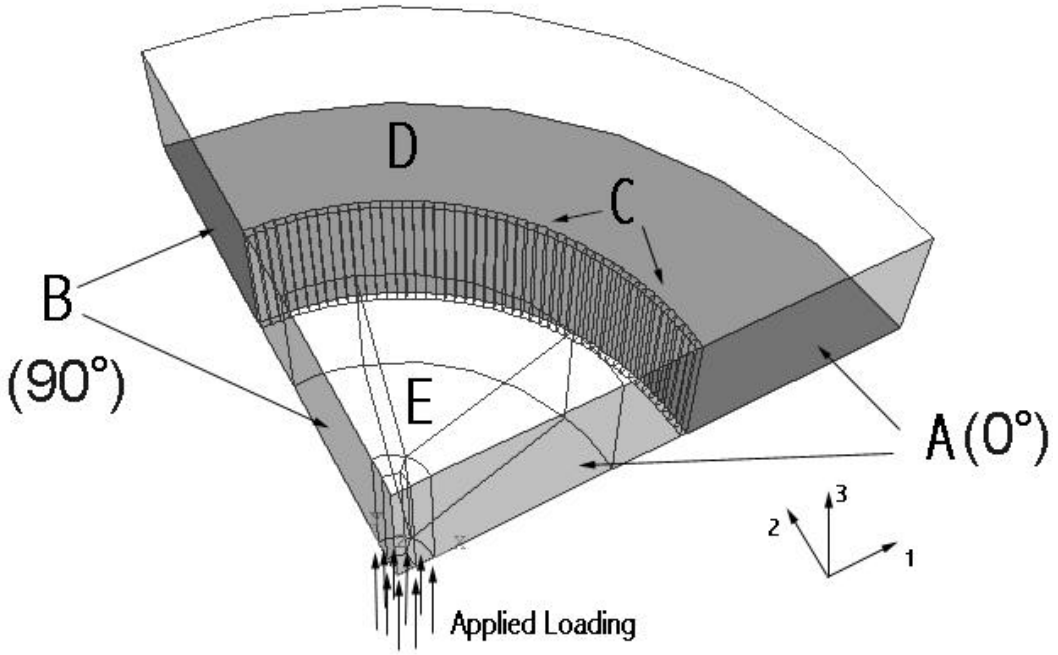

Figure 6.3. Schematic of finite element model of an edge-loaded thin film

The meshing scheme for the edge-loaded model is identical to the scheme of the shaft-loaded blister test. Per recommendation in Chapter 3, first order, reduced integration linear brick elements are used in all analyses.

Analyses have been performed with and without residual stress. Residual stress is incorporated by thermal mismatches between the coating and substrate, as developed in Section 4.4.2. Table 6.1 contains the pertinent data for calculation of residual stress. The models without residual stress are linear analyses, and the models with residual stress include non-linear geometry. The necessity of non-linear analyses for capturing residual stress was established in Chapter 4. The issue of having sufficient adhered material behind the debond for the case including residual stress, has been accounted for in this geometry based on the results of Chapters 4 and 5.

The three-dimensional continuum meshes for each radius of debond have been refined such that the analyses reach the limitations of computing resources in both memory and disk space. To provide an understanding of the validity of the results at this extent of computer resources, a convergence analysis for the case of a 0.04 *mm* debond radius has been performed. Figure 6.4 gives convergence curves of G_{total} results for various values of theta at a 0.04 *mm* debond radius.

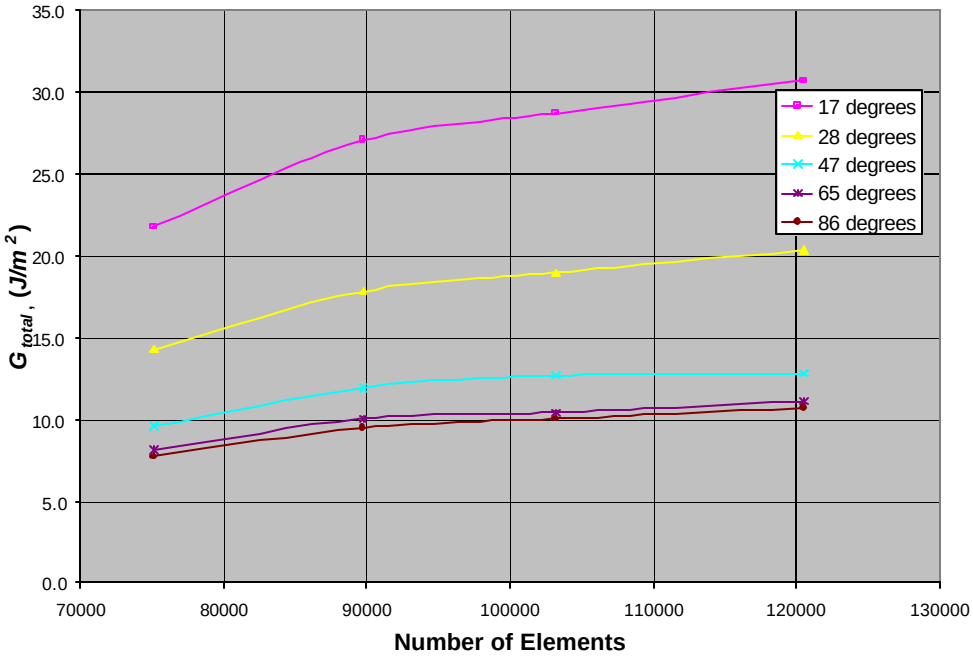

Figure 6.4. Indication of convergence of G_{total} at 0.04 *mm* debond radius

The fact that the curves of Figure 6.4 begin to plateau with increasing numbers of elements along lines of constant theta indicates convergence of G_{total} values. Table 6.2 presents percent differences in energy release rates for all modes of energy release rates of the four convergence models. The percent differences calculation is defined as,

$$\%difference = 100 \times \frac{abs(G_{i+1} - G_i)}{G_i} \tag{6.1}$$

where i represents a G value from the coarser mesh.

Table 6.2. Convergence of energy release rates in 0.04 mm debond by percent differences

	75096 to 89748 elements				89748 to 103194 elements				103194 to 120528 elements			
Theta	G_I	G_{II}	G_{III}	G_{total}	G_I	G_{II}	G_{III}	G_{total}	G_I	G_{II}	G_{III}	G_{total}
0.0	5.8	30.1	35.0	15.3	1.0	6.5	8.6	3.7	0.4	6.9	11.5	3.8
3.8	18.8	25.3	24.7	21.1	4.7	6.0	7.0	5.5	5.3	5.4	7.5	5.9
5.6	20.4	26.3	28.3	23.1	5.2	6.3	8.1	6.0	5.9	5.5	9.4	6.6
9.4	20.8	27.2	26.3	23.0	5.2	6.6	7.3	5.9	5.8	5.6	8.4	6.5
16.9	22.0	31.6	27.1	24.1	5.6	7.5	7.4	6.2	6.2	6.1	8.7	6.9
28.1	23.1	48.1	27.8	24.9	5.8	10.9	7.6	6.4	6.5	7.7	9.0	7.2
37.5	23.8	176.7	28.1	24.9	6.0	25.9	7.7	6.4	N/A	N/A	N/A	N/A
46.9	24.3	42.5	28.2	24.6	6.1	20.2	7.7	6.3	3.8	24.9	12.5	1.1
56.3	24.6	11.9	28.3	24.2	6.2	4.9	7.8	6.2	5.2	7.8	14.3	3.0
65.6	24.9	3.8	28.2	23.7	6.2	28.0	45.9	3.8	6.1	20.1	60.7	6.7
75.0	25.0	0.5	28.2	23.3	6.2	1.0	7.6	5.9	7.0	4.0	33.7	5.9
84.4	24.9	0.8	28.3	23.0	6.3	0.6	7.5	5.8	5.9	11.0	10.1	6.3
86.2	24.9	1.0	48.7	23.0	6.3	0.4	11.6	5.9	7.0	0.6	1.9	6.6

The N/A at the right of Table 6.2 is data that was not collected at this particular theta. As one moves from left to right across Table 6.2, percent differences decrease with increasing number of elements. The final model with a 120,528 element mesh converges G_I to an average of 5.4% for all data entries of theta, G_{II} to 6.1% excluding two outliers, G_{III} to 9.3% excluding two outliers, and G_{total} to an average of 5.5%.

6.3 Step-wise acquisition of energy release rates

Acquisition of energy release rates for this model differs from the methodology established in the three-dimensional models of the pressurized and shaft-loaded blister tests. The pressurized and shaft-loaded blister tests have *G* values that are independent of theta. The edge-loaded model, however, has energy release rates that are highly dependent on theta. This dependency demands that *G* values be sampled at various points about the assumed debond circumference. This can be accomplished by releasing varying theta increments from the bottom surface of volume C from Figure 6.3. The release of five elements is demonstrated in Figure 6.5. For the particular mesh discretization of this model, five elements about the debond front corresponds to the release of 7.5°. Of particular concern is the amount of area released by simulated debond propagation. For the case of Figure 6.5, elements 1 and 5 only have one node released, and thus the effective released area for each of these is ½ the area of an element. Therefore the total released area is 4 elements.

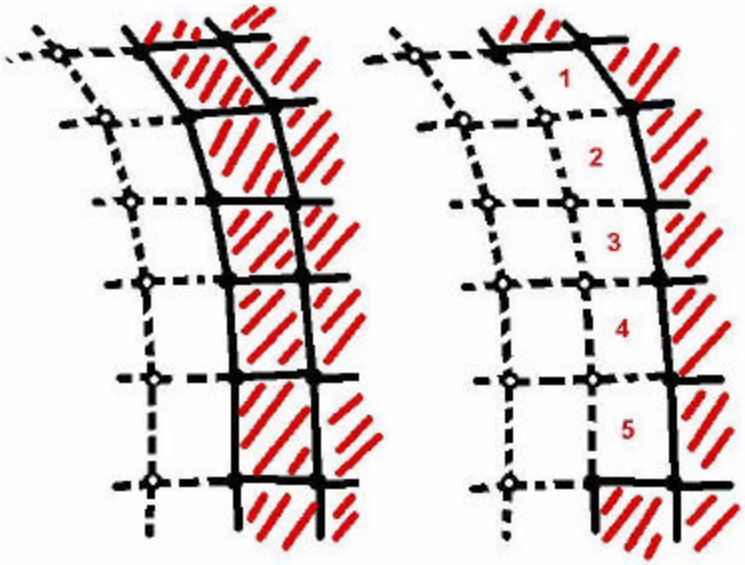

Figure 6.5. Mesh release of 5 elements for a theta increment of 7.5°

A study was performed to determine the optimal theta increment for accurate determination of spatial energy release rates. Using the probe test geometry under a prescribed displacement of 0.01 *mm* and at a debond radius of 0.04 *mm*, energy release rates were obtained for theta increments of 15°, 7.5° and 3.75°. 3.75° increments correspond to the release of one node at a time. The results of this study are displayed in Figure 6.6.

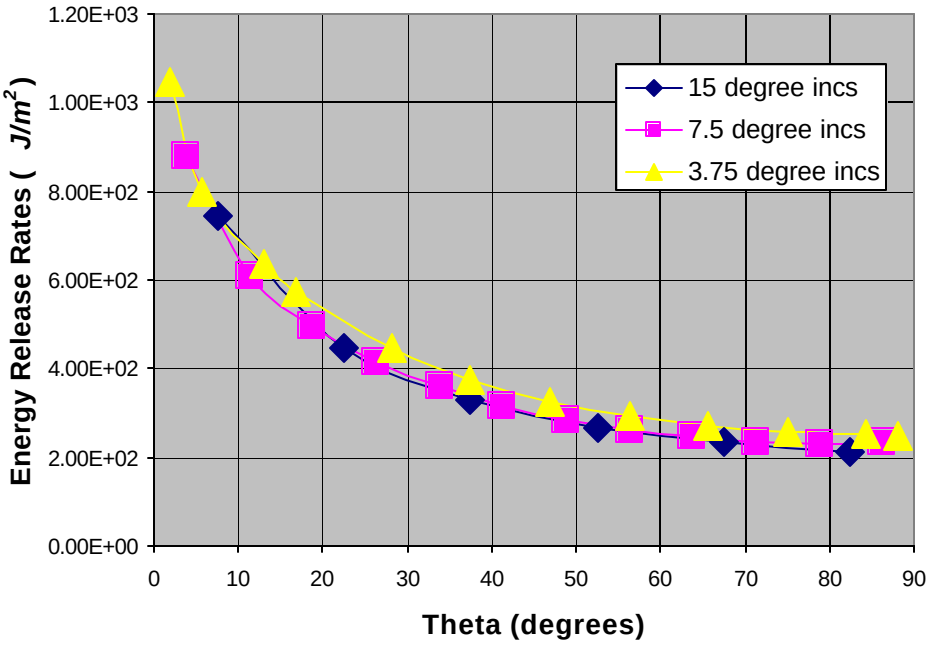

Figure 6.6. Resolution determination for step-wise acquisition of energy release rates

Figure 6.6 indicates that despite the resolution, the associated change in released area appropriately normalizes the energy release rates. The increased resolution is able to capture more localized effects, as can be seen towards the free edge, 0°. Lower resolutions (15°) tend to have more of a smearing effect on the data.

The following discussion demonstrates in detail the calculation procedure for energy release rates for node by node mesh release, which corresponds to the 3.75° increment from above. Figure 6.7 will be used to explain the node by node step-wise energy release rate acquisition for an edge-loaded thin film.

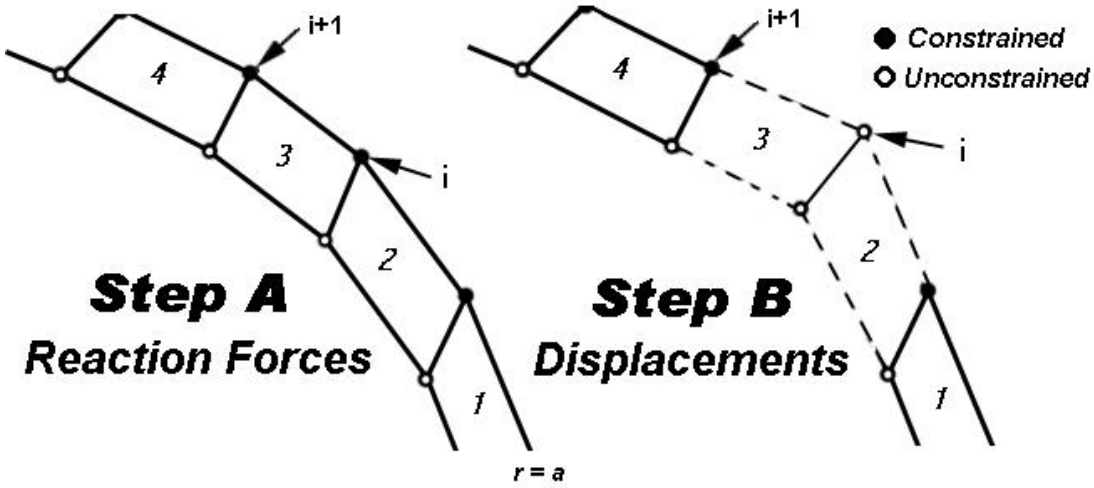

Figure 6.7 Mesh release for acquisition of energy release rates

Figure 6.7 represents a step-wise energy release rate extraction method with two steps of data acquisition, step A and step B. The figure shows a segment consisting of four elements at the base of volume C. The filled in circles (•) represent constrained nodes, which also correspond to the edge of debond. The unfilled circles (o) are unconstrained nodes. In step A, the geometry is unaltered and reaction forces are queried from node i. In step B, elements 2 and 3 are released by freeing node i. Node i is then queried for displacements incurred by release and G_i is calculated. Node i is returned to its original position and becomes fully constrained again. Node i+1 will then be queried for reaction forces, released, queried again for displacements, and finally returned to its initial position. This pattern of unzipping and zipping the mesh continues about the circumference of the debond, from 0° to 90°. The area of one element, $A_{element}$, can be calculated as,

$$A_{element} = \frac{p(r+\Delta r)^2 - pr^2}{4n} \tag{6.2}$$

where n is the number of elements along the bottom surface of volume C. Eq. 6.2 effectively calculates the released incremental area of a full blister, divides by 4 to represent the amount of volume C in Figure 6.2, and divides by the number of elements in the released area. Since the release of one node effectively releases two elements into a triangular configuration for an inner node, the released area is one half the area of two released elements, which corresponds to the area of one released element. Therefore the

effective released area, ΔA_{inner}, for an inner node is equivalent to the area of one element, $A_{element}$.

$$\Delta A_{inner} = A_{element} \tag{6.3}$$

The release of the outer node, at 0°, only effectively releases one element into a triangular configuration. Therefore the effective released area for the outer node, dA_{outer}, is equivalent to one half the area of one element,

$$\Delta A_{outer} = \frac{A_{element}}{2} \tag{6.4}$$

The energy release rates for an inner node at the angle at which node i exists can now be calculated using the modified crack closure method as seen in Eqs. (6.5).

$$\begin{aligned} G_I &= G_{\mathrm{z}} = \frac{1}{2\Delta A_{inner}}\left[F_{i\,\mathrm{z}}(u_{i\,\mathrm{z}})\right] \\ G_{II} &= G_{\mathrm{radial}} = \frac{1}{2\Delta A_{inner}}\left[F_{i\,\mathrm{radial}}(u_{i\,\mathrm{radial}})\right] \\ G_{III} &= G_{\mathrm{tangential}} = \frac{1}{2\Delta A_{inner}}\left[F_{i\,\mathrm{tangential}}(u_{i\,\mathrm{tangential}})\right] \end{aligned} \tag{6.5}$$

The same procedure can be followed to produce the energy release rates for the outer node by replacing ΔA_{inner} with ΔA_{outer}.

6.4 Energy release rate results

The energy release rate results for debond radii of *a* equal to 0.04 *mm*, 0.08 *mm*, 0.1 *mm*, 0.2 *mm*, and 0.3 *mm* are presented in this section. Energy release rate results from linear analyses without residual stress and non-linear analyses with residual stress are given in two formats. The left graphs contain energy release rates in total and by mode. The right graphs are mode-mixity plots, containing the percent composition of *G*. The data for each length of debond radius are presented for the cases with and without residual stress, and then a small synopsis ensues explaining key points to take from the combined four graphs. Particular sensitivities to residual stress and radius of debond will be isolated in Sections 6.5 and 6.6, respectively.

6.4.1 0.04 mm debond radius (h/a=1)

Figure 6.8 presents the results of the linear analysis without residual stress, and Figure 6.9 presents the results of the non-linear analysis with residual stress for the smallest debond tested, 0.04 *mm*. For this case maximum G_{linear} = 26.5 and maximum $G_{residual}$=220, producing a $G_{residual}$ to G_{linear} ratio, $\frac{G_{residual}}{G_{linear}} = 8.3$.

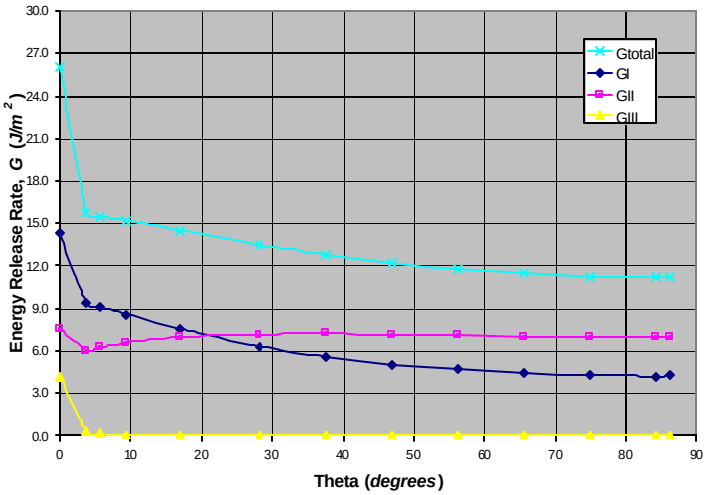

Figure 6.8a

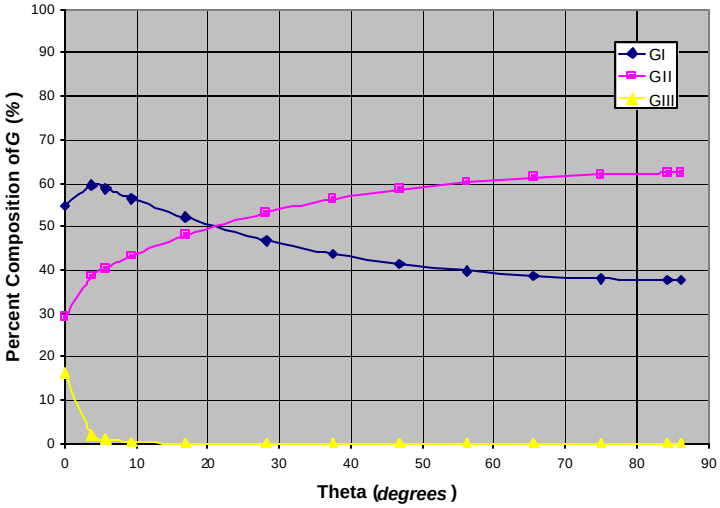

Figure 6.8b

Figure 6.8a. Linear energy release rate plot without residual stress for 0.04 *mm* debond radius
Figure 6.8b. Linear mode mixity plot without residual stress for 0.04 *mm* debond radius

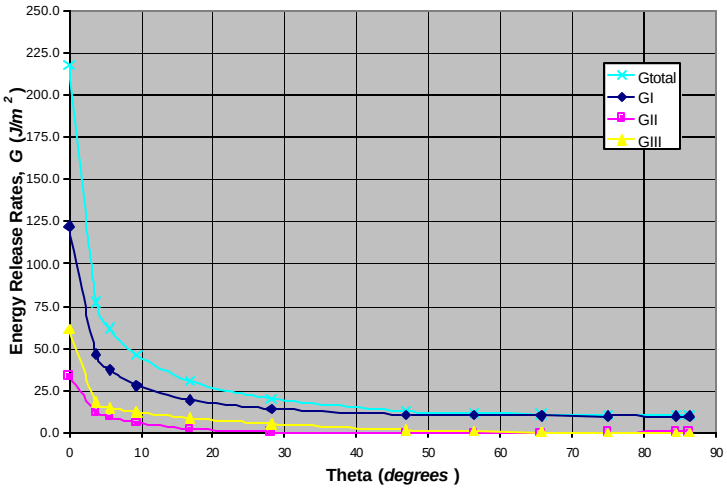

Figure 6.9a

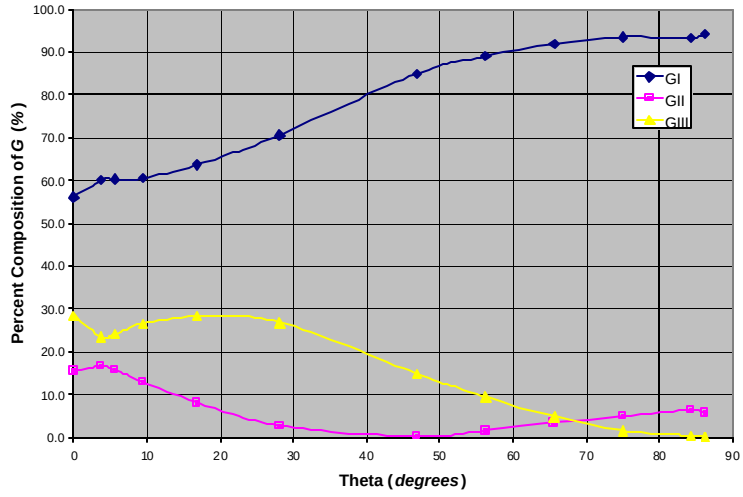

Figure 6.9b

Figure 6.9a. Non-linear energy release rate plot with residual stress with 0.04 *mm* debond radius
Figure 6.9b. Non-linear mode mixity plot with residual stress with 0.04 *mm* debond radius

Figures 6.8a and 6.9a indicate that mode I is the dominant energy release rate for both cases because at a debond radius equal to the size of film thickness (h/a=1.0), out of plane shearing is the dominant mode of failure. Much like the pressurized and shaft-loaded blister tests without residual stress, mode III contributions are mostly negligible in Figure 6.8a. The increase of G_{III} near the free edge is due to activation of Poisson's ratio coupling terms from the large tensile stresses developed during loading. At 90°, mode III energy release rates are forced to zero due to boundary conditions on the plane of symmetry that prescribe the tangential displacement to be zero. The reduction of mode II composition to zero at 44° in Figure 6.9b actually corresponds to a switch in mode II (radial) displacement directions from compressive to tensile. Since strain energy can only be positive, Figure 6.9b cannot reveal this. Figure 6.10 presents the radial, tangential, and z-displacements from the non-linear analysis with residual stress.

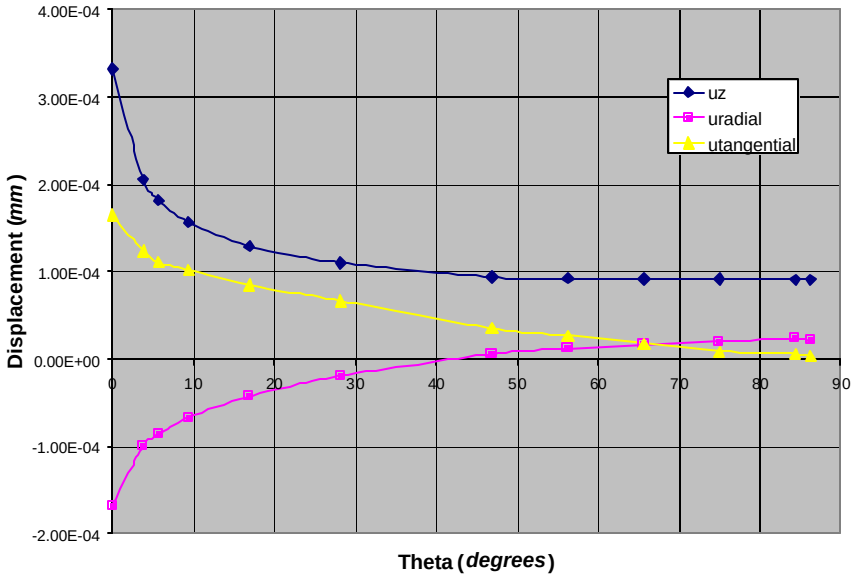

Figure 6.10. Debond front displacements for residual stress analysis at a debond radius of 0.04 *mm*

Figure 6.10 indicates that mode II (radial) displacements transition from negative to positive at a crossover point of approximately 44°. This is the cause for G_{II} becoming zero at this point. This transitioning of mode II displacements, rather than an increase in G_{III} is the cause of the rise in mode III percent composition around 20-30°.

6.4.2 0.08 mm debond radius (h/a=0.5)

Figure 6.11 presents the results of the linear analysis without residual stress, and Figure 6.12 presents the results of the non-linear analysis with residual stress for a 0.08 *mm* debond radius. For this case maximum G_{linear} = 4.6 and maximum $G_{residual}$=173, producing a $G_{residual}$ to G_{linear} ratio, $\frac{G_{residual}}{G_{linear}} = 37.6$.

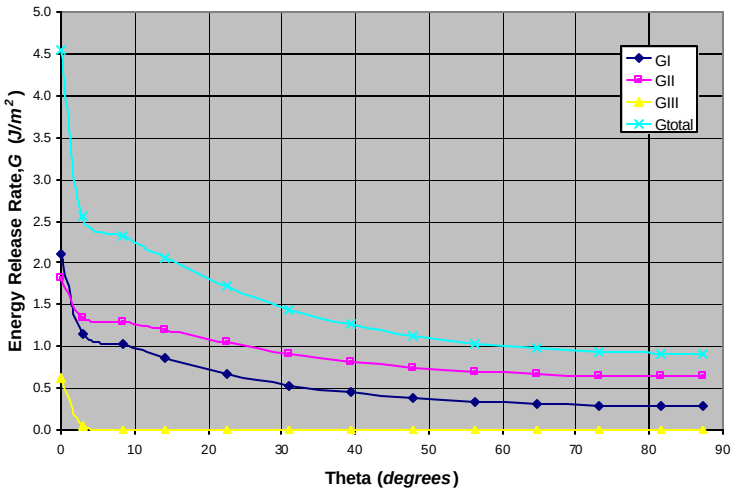

Figure 6.11a

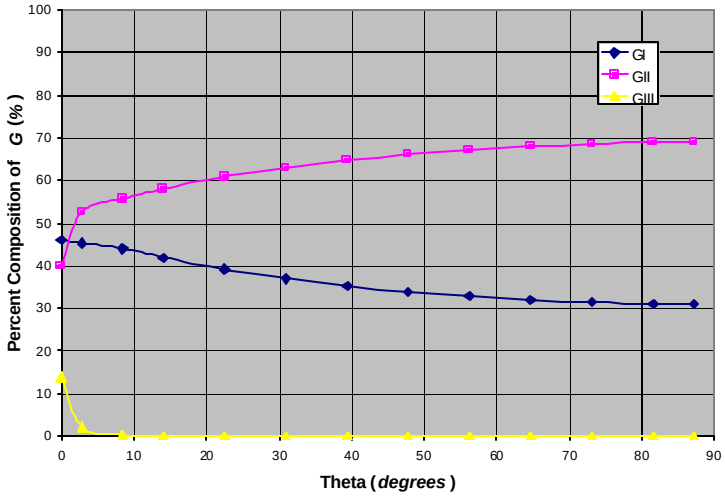

Figure 6.11b

Figure 6.11 a. Linear energy release rate plot without residual stress with 0.08 *mm* debond radius
Figure 6.11 b. Linear mode mixity plot without residual stress with 0.08 *mm* debond radius

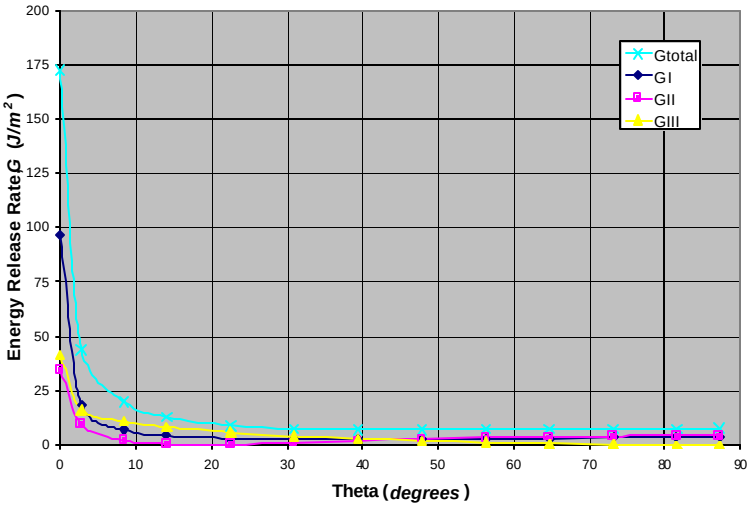

Figure 6.12a

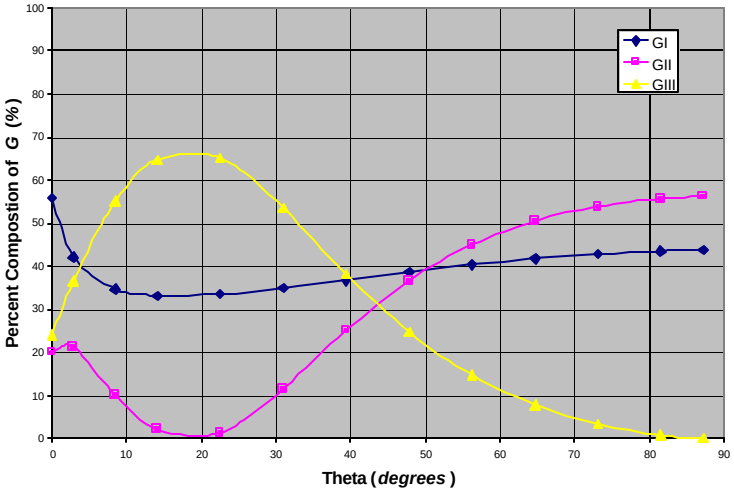

Figure 6.12b

Figure 6.12a. Non-linear energy release rate plot with residual stress with 0.08 *mm* debond radius
Figure 6.12b. Non-linear mode mixity plot with residual stress with 0.08 *mm* debond radius

From Figures 6.11a and 6.12a it is to be noted that inclusion of residual stress further flattens energy release rate curves. Figure 6.12b indicates that mode I experiences a slight drop in composition after a dramatic rise at the free edge. Residual stress also significantly influences mode mixity. The transition of mode II (radial) displacements from negative to positive has shifted to about 18° as seen in Figure 6.13.

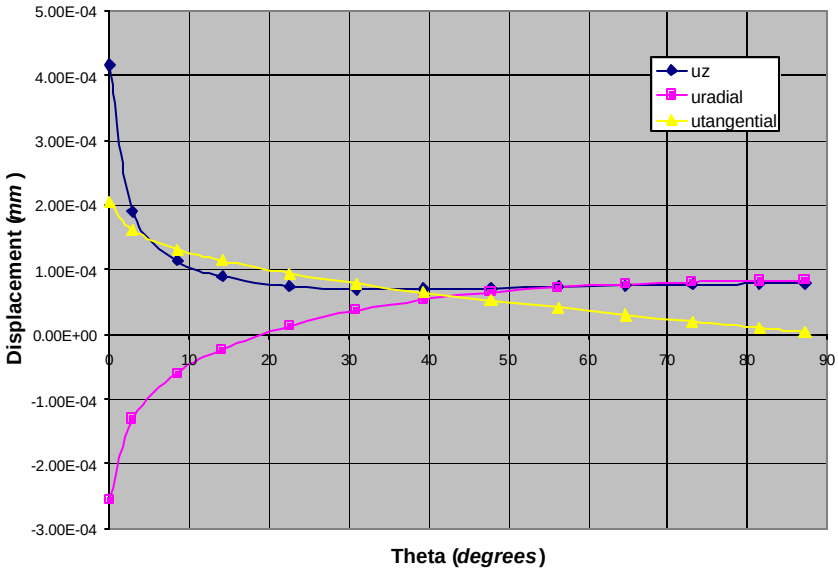

Figure 6.13. Debond front displacements for residual stress analysis at a debond radius of 0.08 *mm*

Again, the transition of mode II (radial) displacements is the cause for the significant percent increase in mode III composition at 18°.

6.4.3 0.1 mm debond radius (h/a=0.4)

Figure 6.14 presents the results of the linear analysis without residual stress, and Figure 6.15 presents the results of the non-linear analysis with residual stress for a 0.1 *mm* debond radius. For this case maximum total G_{linear} = 0.55 and maximum total $G_{residual}$=112, producing a $G_{residual}$ to G_{linear} ratio, $\frac{G_{residual}}{G_{linear}} = 204.$

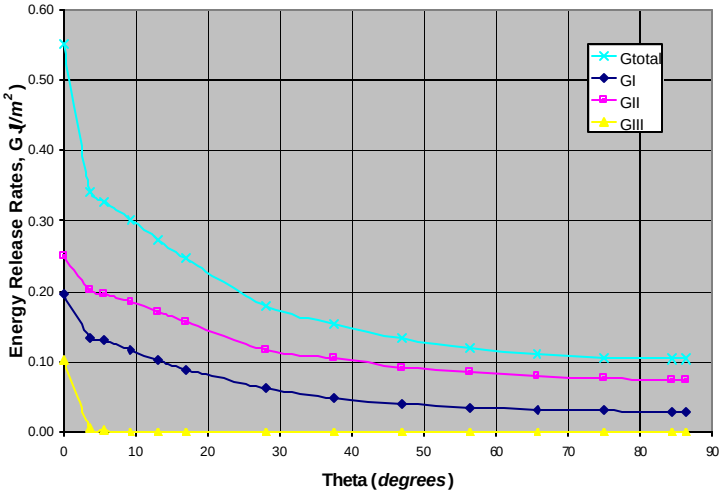

Figure 6.14a

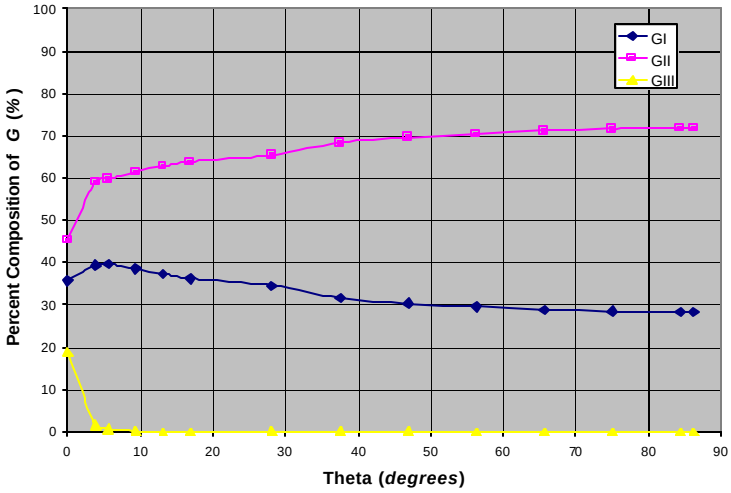

Figure 6.14b

Figure 6.14a. Linear energy release rate plot without residual stress with 0.1 *mm* debond radius
Figure 6.14b. Linear mode mixity plot without residual stress with 0.1 *mm* debond radius

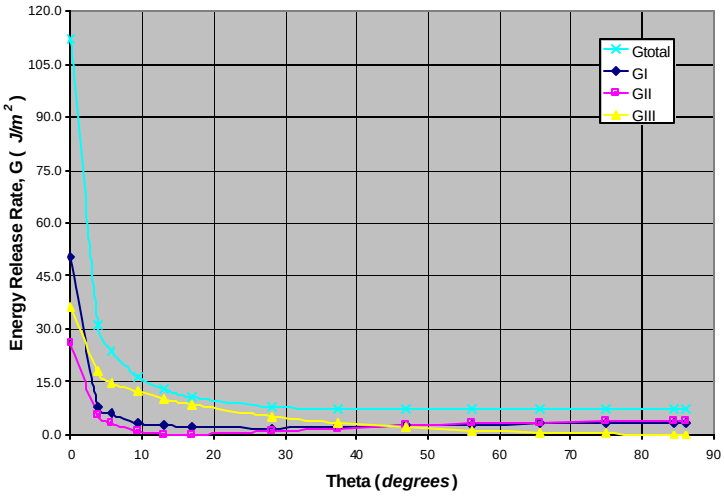

Figure 6.15a

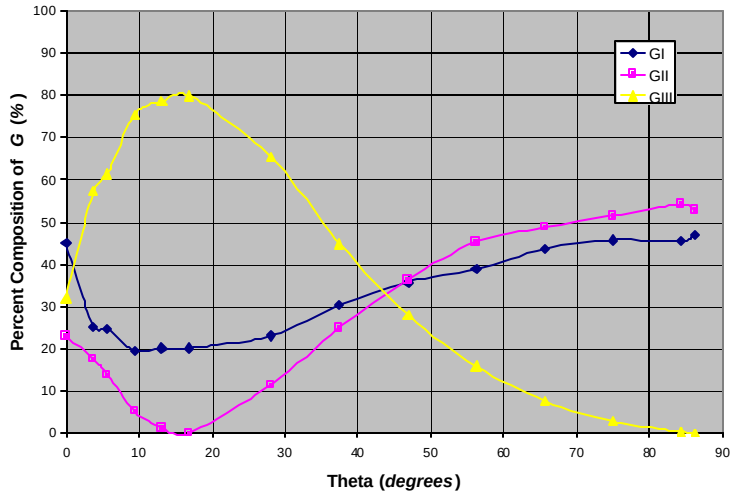

Figure 6.15b

Figure 6.15a. Non-linear energy release rate plot with residual stress with 0.1 *mm* debond radius
Figure 6.15b. Non-linear mode mixity plot with residual stress with 0.1 *mm* debond radius

Figures 6.14a and 6.15a indicate that inclusion of residual stress increases the magnitude of energy release rates by a factor of about 200. Figure 6.14a indicates that release rates of the analysis without residual stress have achieved mode clarity, meaning mode dominance is stable throughout theta. Figure 6.16 shows the z, radial, and tangential displacements for the 0.1*mm* debond.

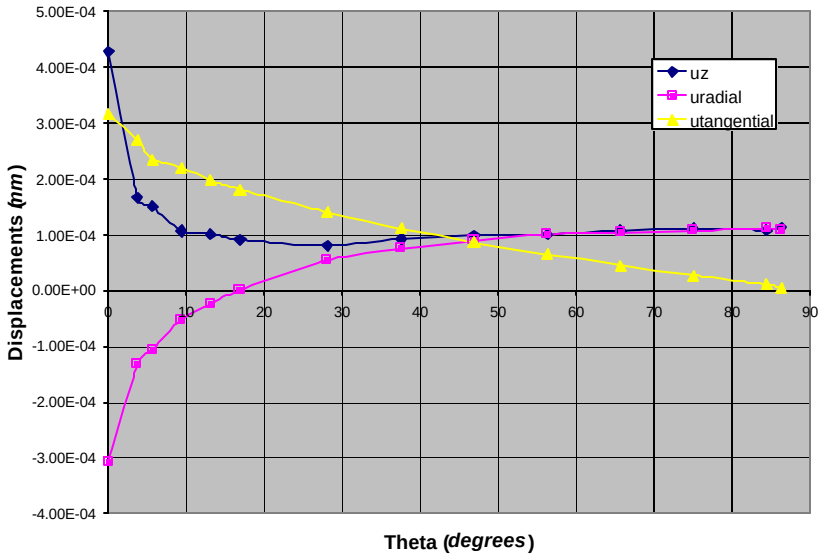

Figure 6.16. Debond front displacements for residual stress analysis at a debond radius of 0.1 *mm*

Figure 6.16 indicates that direction crossover for mode II (radial) displacements has decreased slightly to 17°. The decline in z-displacements combined with the slower transition of radial displacements results in higher mode III compositions as shown in Figure 6.15b.

6.4.4 0.2 mm debond radius (h/a=0.2)

Figure 6.17 presents the results of the linear analysis without residual stress, and Figure 6.18 presents the results of the non-linear analysis with residual stress for a 0.2 *mm* debond. For this case maximum total $G_{linear} = 0.46$ and maximum total $G_{residual}$=227, producing a $G_{residual}$ to G_{linear} ratio, $\frac{G_{residual}}{G_{linear}} = 494.$

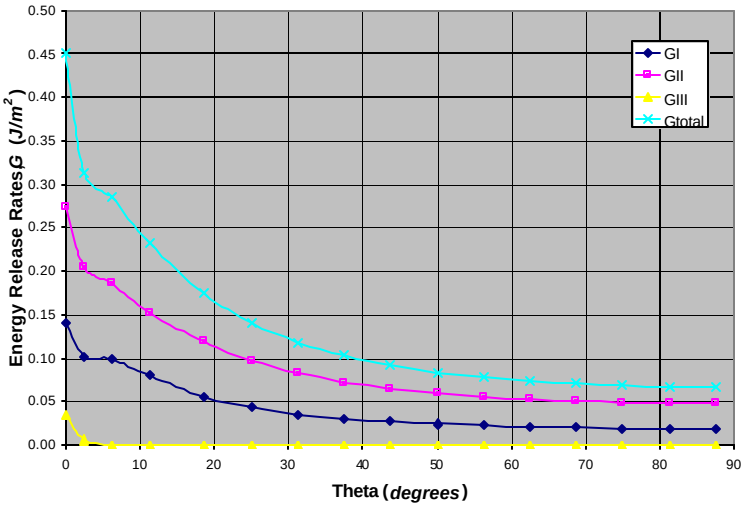

Figure 6.17a

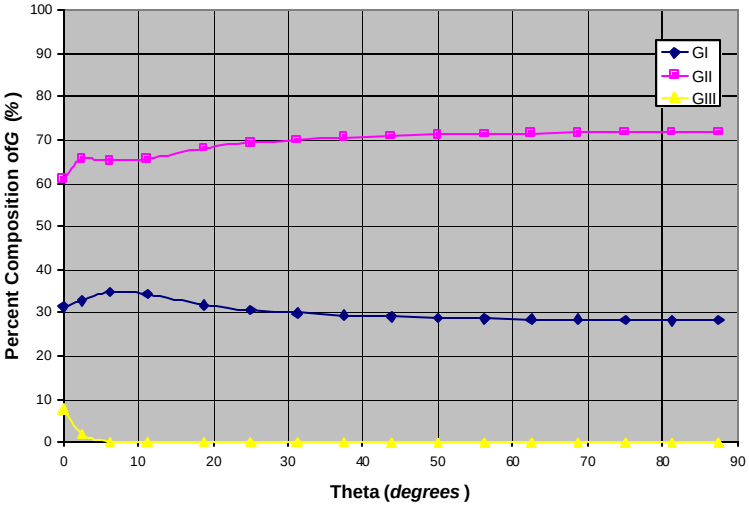

Figure 6.17b

Figure 6.17a. Linear energy release rate plot without residual stress with 0.2 *mm* debond radius
Figure 6.17b. Linear mode mixity plot without residual stress with 0.2 *mm* debond radius

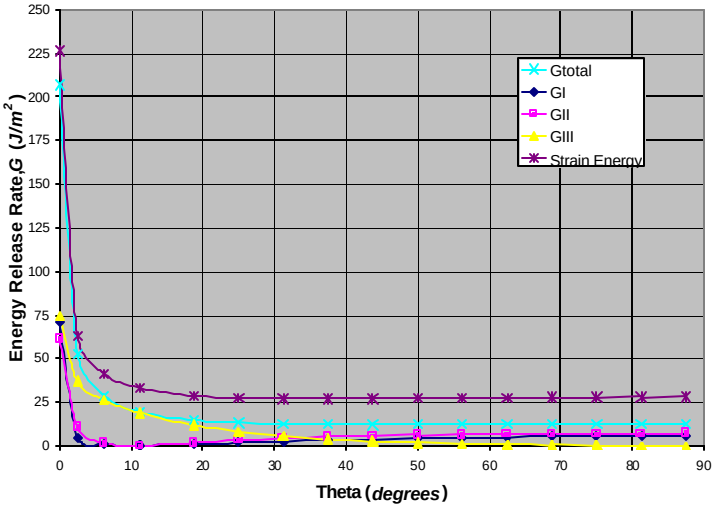

Figure 6.18a

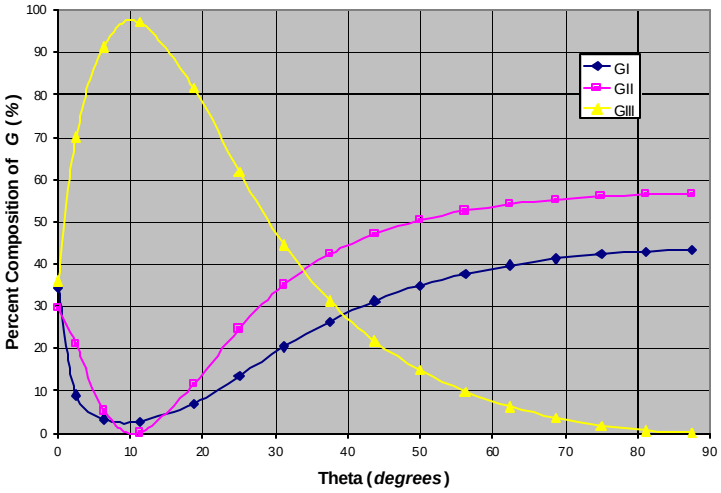

Figure 6.18b

Figure 6.18a. Non-linear energy release rate plot with residual stress with 0.2 *mm* debond radius
Figure 6.18b. Non-linear mode mixity plot with residual stress with 0.2 *mm* debond radius

In Figure 6.17b it is apparent that the mode composition has leveled off for the case without residual stress, with mode I at 30%, and mode II at 70%. The increase in mode III composition in Figure 6.18b now occurs at 11° and is more abrupt. Evidence for this can be found in the displacement plot of Figure 6.19.

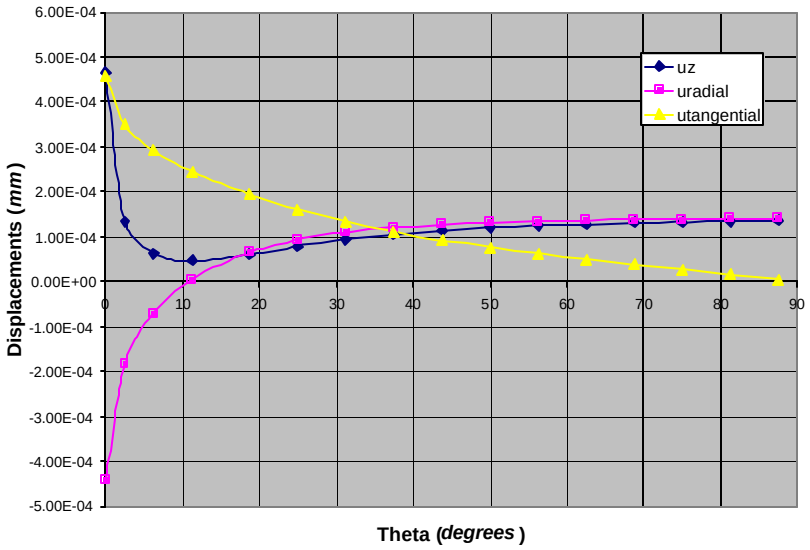

Figure 6.19. Debond front displacements for residual stress analysis at a debond radius of 0.2 *mm*

The crossover point from negative to positive of mode II (radial) displacements has come closer to the free edge (0°), at 11°. Z-displacements reach a minimum near the same location. The combined effect of the mode I and II displacements is domination of G by mode III near the free edge (0°).

6.4.5 0.3 mm debond radius (h/a=0.133)

Figure 6.20 presents the results of the linear analysis without residual stress, and Figure 6.21 presents the results of the non-linear analysis with residual stress for a 0.3 *mm* debond. For this case maximum total G_{linear} = 0.11 and maximum total $G_{residual}$=210, producing a $G_{residual}$ to G_{linear} ratio, $\frac{G_{residual}}{G_{linear}} = 1909$.

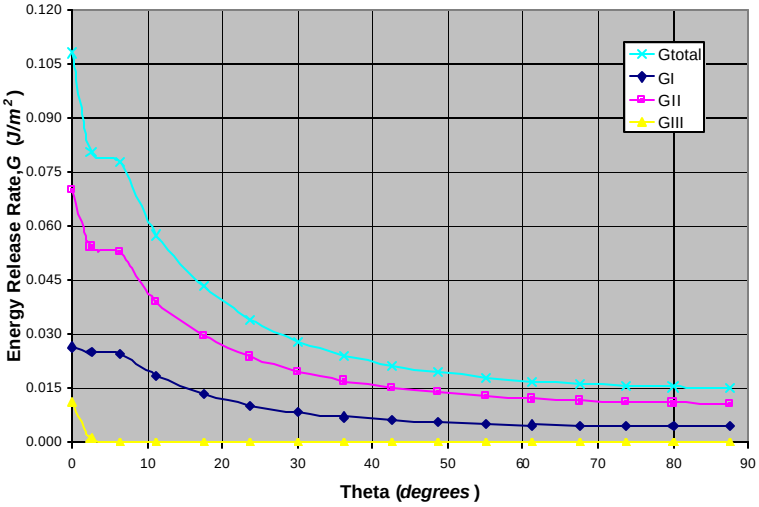

Figure 6.20a

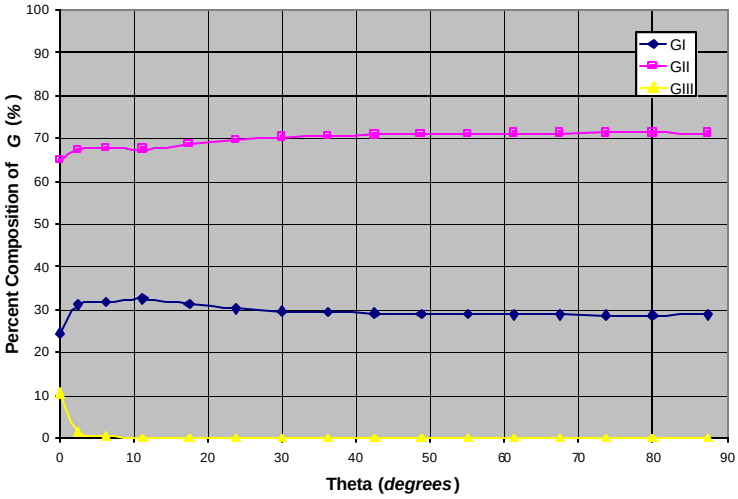

Figure 6.20b

Figure 6.20a. Linear energy release rate plot without residual stress with 0.3 *mm* debond radius
Figure 6.20b. Linear mode mixity plot without residual stress with 0.3 *mm* debond radius

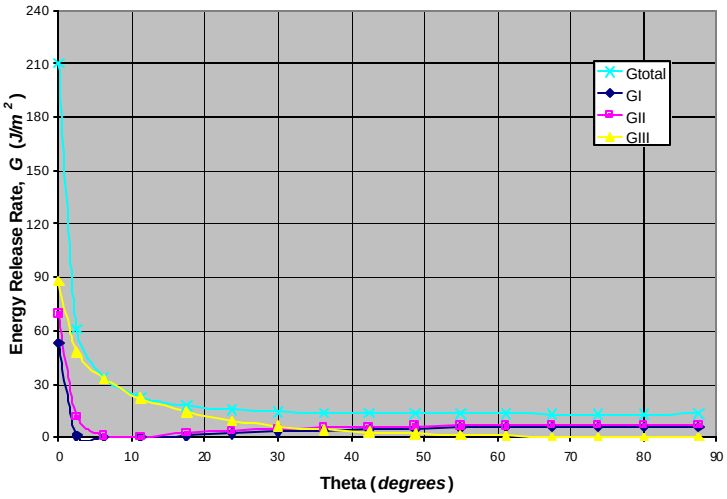

Figure 6.21a

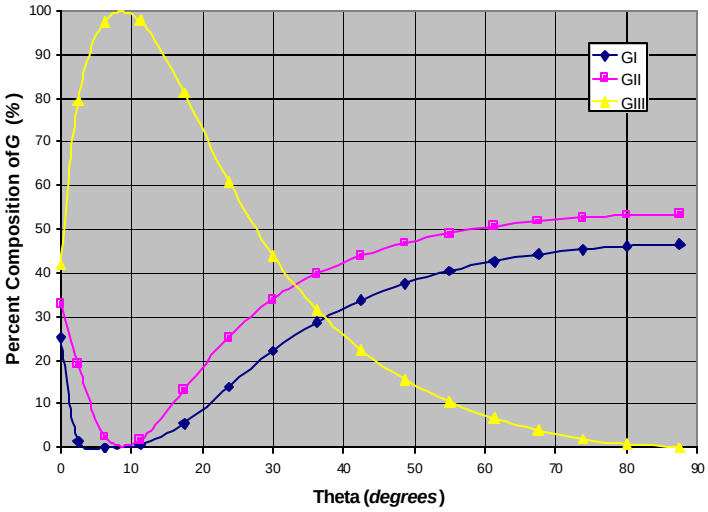

Figure 6.21b

Figure 6.21a. Non-linear energy release rate plot with residual stress with 0.3 *mm* debond radius
Figure 6.21b. Non-linear mode mixity plot with residual stress with 0.3 *mm* debond radius

The energy release rate and mode-mixity trends of Figures 6.20 and 6.21 are nearly identical to the trends from Figures 6.17 and 6.18 of the 0.2 *mm* debond radius. Radial displacements crossover even closer to the free edge (0°), as shown in Figure 6.22.

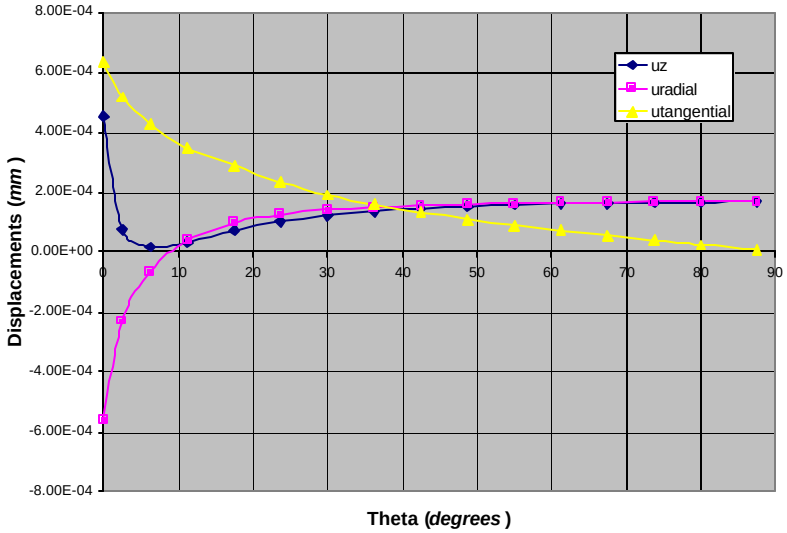

Figure 6.22. Debond front displacements for residual stress analysis at a debond radius of 0.3 *mm*

The crossover point for mode II (radial) displacements has reached 9°. Combined with the sharp decline in z-displacements caused by compressive residual stresses, a very high mode III energy release rate composition results at this point.

6.5 Sensitivity to residual stress

6.5.1 Overview

Residual stress plays a significant role in deformation of thin films as can be seen in the difference between corresponding graphs in the previous section. Residual stress tends to pre-tension the bottom surface of the film. Therefore residual stress has a significant impact on energy release rates about the assumed blister circumference. An analysis has been performed to understand the effects of residual stress on thin films. A 1*mm* by 1*mm* by 0.04 *mm* swatch of thin film has been adhered to a substrate and exposed to a temperature change of -155°C. The von Mises stress contours of the bottom surface of this geometry can be found in Figure 6.21

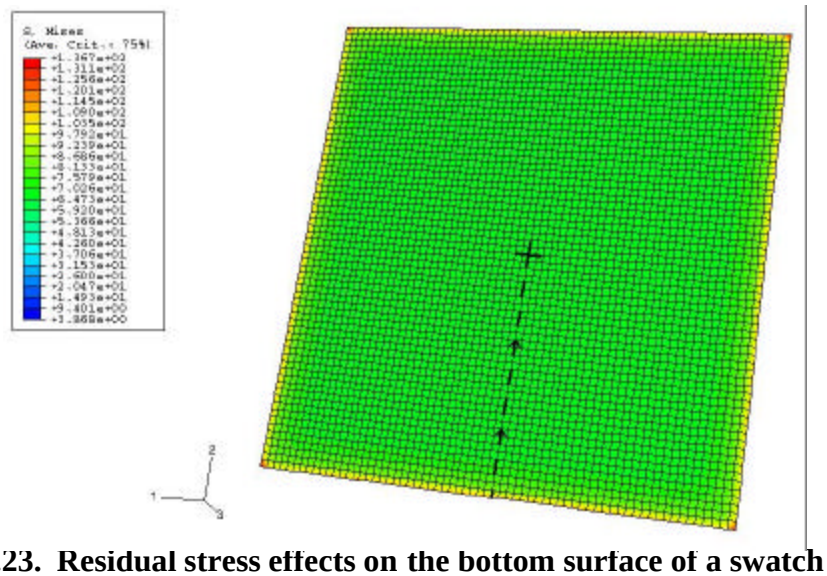

Figure 6.23. Residual stress effects on the bottom surface of a swatch of thin film

Figure 6.24 evaluates how the interface stresses from Figure 6.23 change as a function of distance towards the center of the swatch along the path indicated.

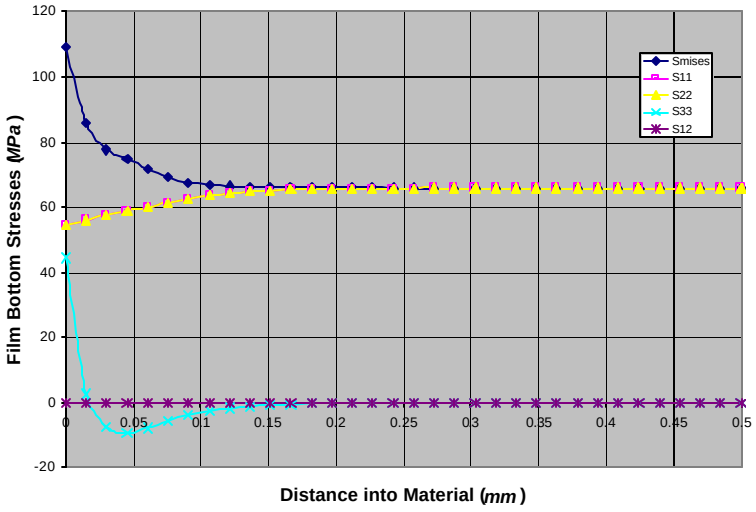

Figure 6.24. Stress levels as a function of distance into material

From Figure 6.24 it is evident that stresses do not reach a uniform state until 0.2 *mm* into the material, which is 5 times the film thickness of 0.04 *mm*. S11 and S22 stresses are equal only because the cited stresses are taken at the interface. Had stresses been taken at any other location within the thickness, the two would have differed. What is more insightful is that residual stress causes S33, or opening stresses, to be highly tensile near the free edge and then quickly drop to being compressive before trailing off to zero as 0.2

mm is approached. This helps to explain why the mode I energy release rates of Section 6.4 decreased in significance at theta values just past the free edge (0°). As the length of debond radius increases, it is expected that any decline in mode I significance will occur closer and closer to the free edge. This is because residual stress will always affect mode I energy release rates at the same distance from the free edge despite the length of debond radius. However, at larger radii, the value of theta that corresponds to this depth will have to decrease. This concept is pictured in Figure 6.25.

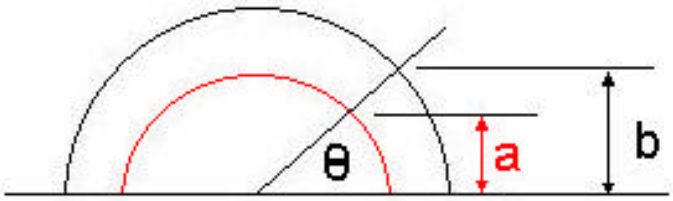

Figure 6.25. Schematic to explain how a single theta corresponds to different depths

Figure 6.25 indicates that for two different radii of debond, a particular theta value will correspond to two different depths into the material, **a** for the smaller debond radius and **b** for the larger debond radius. In order for the depth of the larger debond radius, **b**, to match the depth of the smaller debond radius, **a**, theta would have to decrease.

The S11 and S22 residual stresses of Figure 6.24 may cause the angle at which radial displacements switch directions to become smaller as the length of debond radius increases for the same reasoning as Figure 6.25.

This section investigates energy release rate and mode-mixity sensitivity to residual stress in the thin film. This is captured in sensitivity plots of the change in *G* per change in maximum von Mises stress, $dG/ds'_{\max}$ *(J/m²)/(MPa).* Sensitivity plots of the change in percent composition of *G* per change in maximum von Mises stress, $d\%G/ds'_{\max}$, are also developed. The former is calculated as,

$$\frac{dG}{ds'_{\max}} = \frac{G_{res} - G_{nores}}{s'_{res\,\max} - s'_{nores\,\max}} \tag{6.6}$$

where the maximum von Mises stress occurs at the debond front element closest to the free edge for all models. The sensitivity of mode mixity to residual stress is calculated

using the same type of equation as Eq. 6.6. Positive sensitivities indicate that residual stress causes an increase in energy release rates, zero sensitivities indicate no effect, and negative sensitivities indicate a decline in energy release rates. Sensitivity is discussed as a function of theta about the assumed debond front, and as a function of length of debond radius.

6.5.2 Mode I sensitivity with respect to s'_{max}

6.5.2.1 dG_I / ds'_{max}

Figure 6.26 presents the sensitivity plot for mode I energy release rates to residual stress versus theta for all debond radii from 0.04 to 0.3*mm*. .

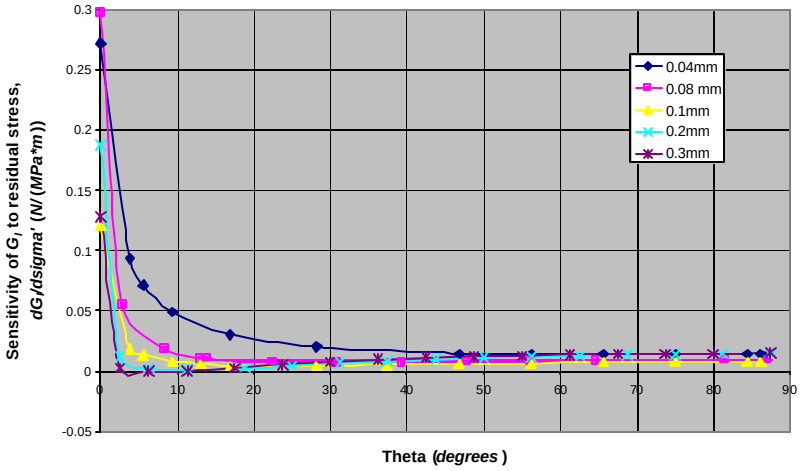

Figure 6.26. Mode I energy release rate sensitivity to residual stress

Figure 6.26 indicates that for all debond radii, G_I is far more sensitive to residual stress at points along the debond near the free edge (0°) than at points along the debond in the film interior. In fact, at thetas approaching the plane of symmetry (90°), the effect of residual stress is minimal. Sensitivity is far more pronounced in smaller debond radii, both at the free edge (0°) and further into the film. For the largest of debond radii, residual stress does not affect energy release rates for thetas of 5 to 20°. Otherwise, residual stress increases mode I energy release rates.

6.5.2.2 $d\%G_I / ds'_{\max}$

Figure 6.27 presents the sensitivity plot of percent contribution of G_I to residual stress versus theta for all debond radii from 0.04 to 0.3*mm*.

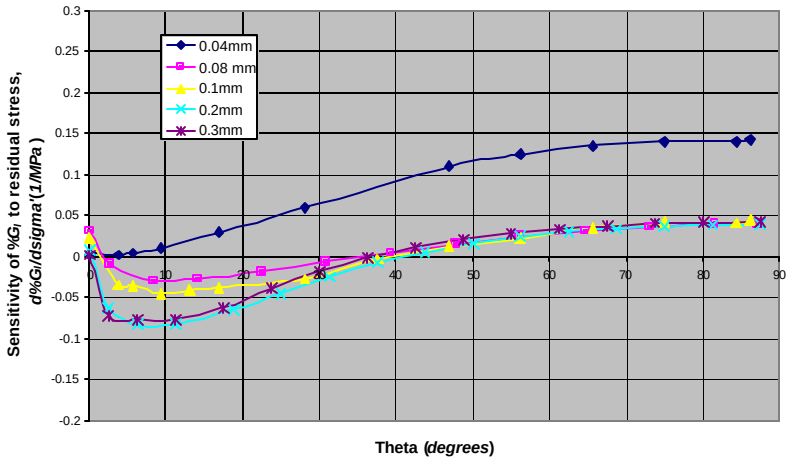

Figure 6.27. Sensitivity of mode I contribution percentage to residual stress

Figure 6.27 indicates that the sensitivity of percent contribution of G_I to residual stress is highly dependent upon the length of debond radius. The curve corresponding to the smallest debond radius of 0.04 *mm* shows that $\%G_I$ is more sensitive in the interior of the film than near the free edge (0°). The 0.04 *mm* debond radius curve behaves unlike any of the other curves mainly because under the same prescribed loading, a short debond radius undergoes intense shearing, which primarily concerns mode I release rates, whereas the larger debond radii undergo more of a bending behavior. These modes reflect the infinite medium and thin plate behavior described for the blister tests of Chapters 4 and 5. Residual stress affects all other debond radii similarly, but to different degrees. Residual stress reduces mode I contributions from approximately 2 to 40°, and then increases mode I contributions from 40 to 90°. As the length of debond radius progresses, the intensity of reduction between 2 and 40° increases. The transition from infinite medium to thin plate behavior reduces mode I contributions from mechanical loading. This transition combined with the z-direction compressive residual stress effect demonstrated in Figure 6.24 results in large reductions in mode I contributions.

6.5.3 Mode II sensitivity with respect to s'_{max}

6.5.3.1 dG_{II}/ds'_{max}

Figure 6.28 presents the sensitivity plot for mode II energy release rates to residual stress versus theta for all debond radii from 0.04 to 0.3*mm*.

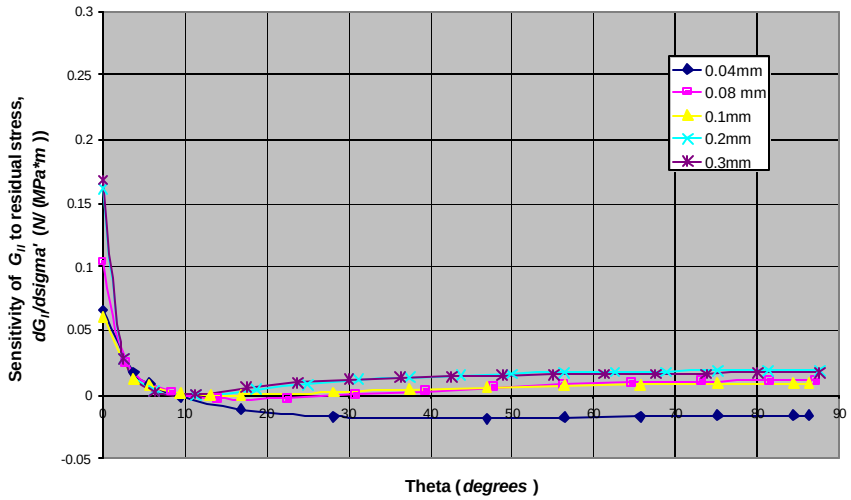

Figure 6.28. Mode II energy release rate sensitivity to residual stress

Figure 6.28 indicates that for all debond radii, G_{II} is highly sensitive to residual stress near the free edge (small thetas). At approximately 10°, residual stress has no effect on any size debond radius. At thetas beyond 10°, sensitivity to residual stress differs depending on the length of debond radius. At the smallest radius of debond, residual stress has a declining effect on G_{II}. For debond radii of 0.08 *mm* and 0.1 *mm*, residual stress begins to once again increase G_{II}, though minimally. Debond radii of 0.2 *mm* and 0.3 *mm* experience the same effect, though slightly more pronounced. In fact, at thetas approaching the plane of symmetry (90°), the effect of residual stress is minimal.

6.5.3.2. $d\%G_{II}/ds'_{max}$

Figure 6.29 presents a sensitivity plot of $\%G_{II}$ to residual stress versus theta for all debond radii from 0.04 to 0.3*mm*.

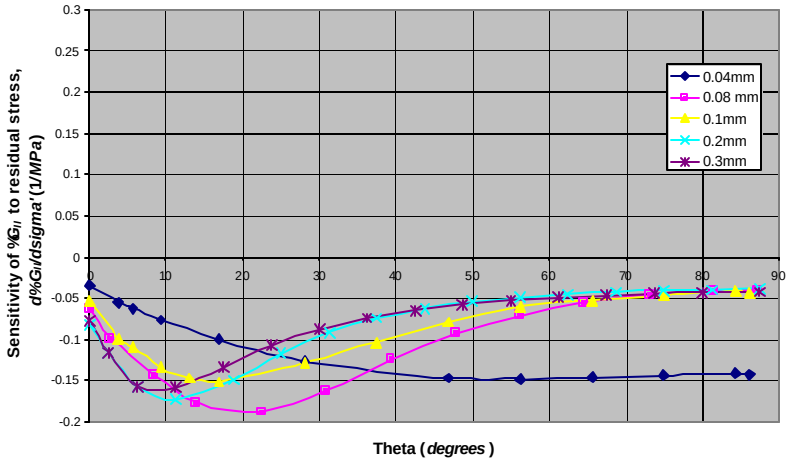

Figure 6.29. Sensitivity of mode II contribution percentage to residual stress

Again, the 0.04 *mm* radius of debond behaves quite differently than all other debond radii. Inclusion of residual stress reduces mode II composition for all thetas, with increasing sensitivity near the symmetry edge. For larger debond radii, residual stress also reduces mode II composition for all thetas, but the minimum occurs at thetas from 10 to 25°, depending on radius of debond. As the radius of debond progresses, the theta at which peak influence occurs declines. The cause of this has been described in Section 6.4 as a product of the transitioning of radial displacements from negative to positive. The shifting of the minimum from high to low is a result of residual stress induced phenomena occurring at particular depths into the film, which correspond to different angles based on the radius of debond. (see Figure 6.25)

6.5.4 Mode III sensitivity with respect to s'_{max}

6.5.4.1. $dG_{III}/ds'_{\max}$

Figure 6.30 presents the sensitivity plot of mode III energy release rates to residual stress versus theta for all debond radii from 0.04 to 0.3*mm*.

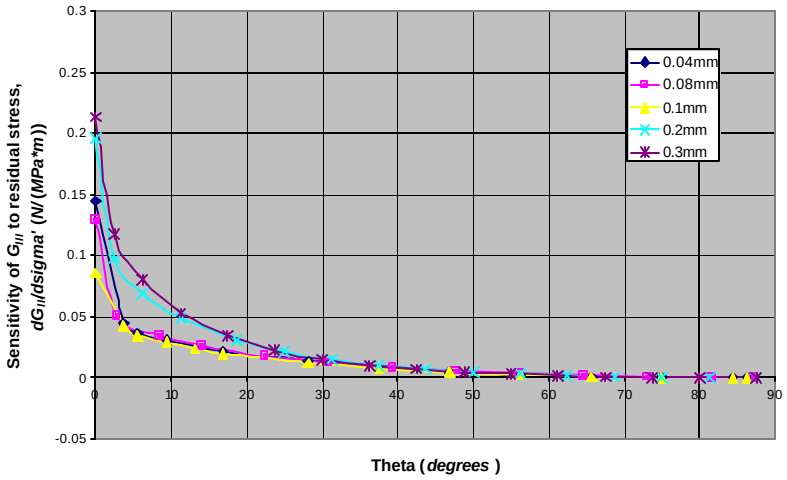

Figure 6.30. Mode III energy release rate sensitivity to residual stress

Figure 6.30 indicates that G_{III} is highly sensitive to residual stress near the free edge (small thetas). As theta increases, the effect slowly dies out until there is no effect of residual stress at the symmetry edge, 90°. This is because at 90°, mode III energy release rates with and without residual stress are forced to zero due to boundary conditions that do not allow displacements across the plane of symmetry. As mentioned in Section 6.4.1, the large increase in significance of mode III with applied residual stress is caused by the in-plane tensile strains activated by residual stress. Larger debond radii experience higher and more prolonged G_{III} sensitivities to residual stress than smaller debond radii.

6.5.4.2. $d\%G_{III}/ds'_{\max}$

Figure 6.31 presents the sensitivity plot for $\%G_{III}$ energy release rates to residual stress.

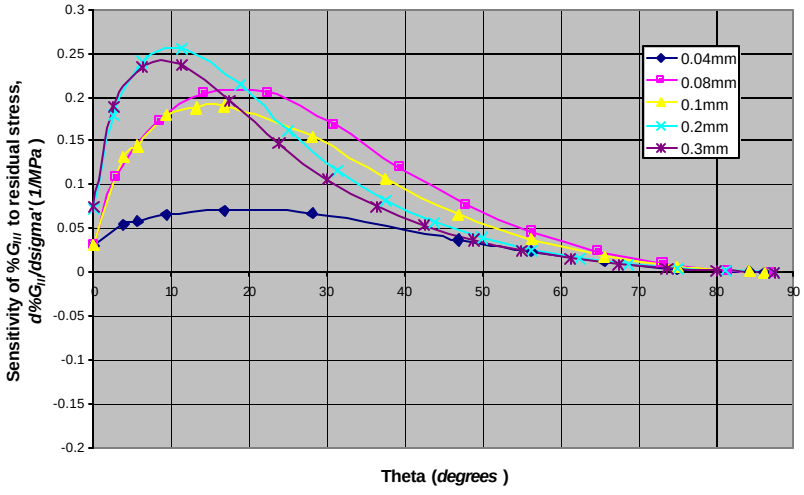

Figure 6.31. Sensitivity of mode III contribution percentage to residual stress

Figure 6.31 indicates that mode III contributions are highly sensitive to residual stress, particularly at thetas of 2 to 50°. As the radius of debond increases, the sensitivity to residual stress intensifies in this range of thetas. The reason for this sharp intensity in sensitivity of G_{III} to residual stress is the crossing over of radial displacements from negative to positive, which reduces mode II contributions at these locations. As indicated in Figure 6.30, there is no intensified G_{III} effect from residual stress.

6.5.5. G_{total} sensitivity with respect to s'_{max}

Figure 6.32 presents a sensitivity plot for total energy release rates to residual stress versus theta for all debond radii from 0.04 to 0.3*mm*.

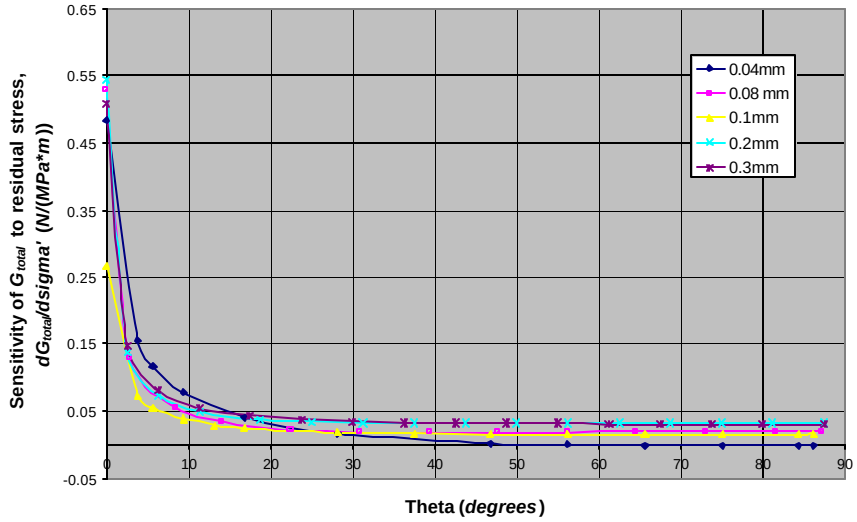

Figure 6.32. G_{total} energy release rate sensitivity to residual stress

Figure 6.32 reveals that even though individual mode sensitivities differed for each radius of debond, the combined sensitivity of all modes of energy release rates to residual stress is similar for all debond radii. Overall, residual stress increases G_{total} for all radii of debond and for all values of theta. G_{total} is very sensitive to residual stress at the free edge. Sensitivities plateau around 20° for all lengths of debond radii, with larger debond radii seeing slightly higher residual stress effect.

6.6 *Effect of length of debond radius*

For ease of comparison, the energy release rate and mode-mixity data of section 6.4 are plotted for all debond radii in this section. The data is divided between linear, no residual stress data and non-linear, residual stress data.

6.6.1 *Linear, no residual stress*

6.6.1.1 *Mode I*

The effect of debond radius on mode I energy release rates is presented in Figure 6.33.

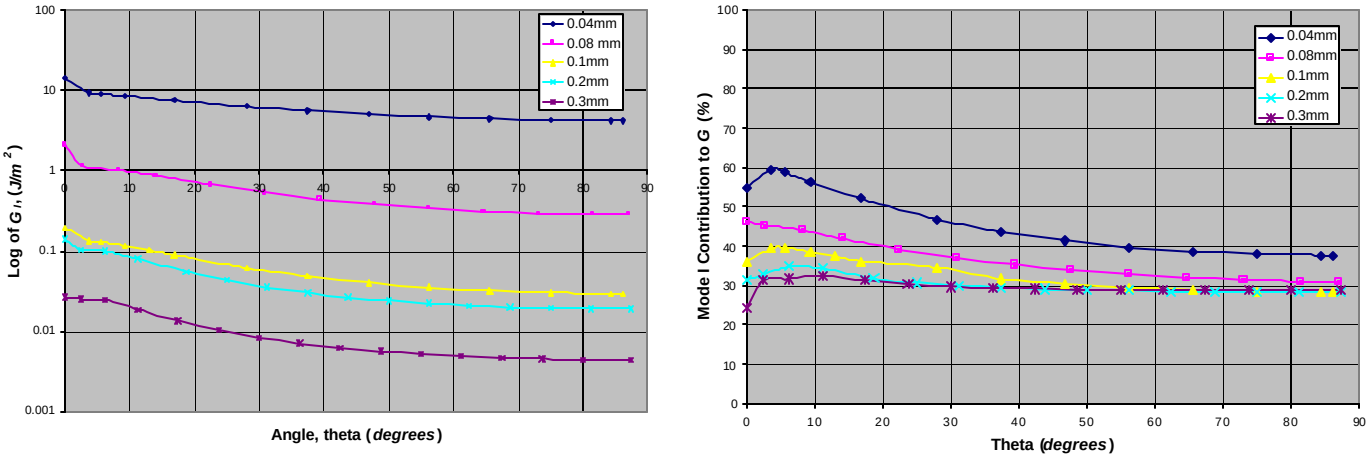

a) **b)**

Figure 6.33. a) Linear G_I values with changing debond radius
b) Linear %G_I contributions with changing debond radius

Figure 6.33a shows that increasing the radius of debond steadily decreases G_I. Figure 6.33b indicates mode I contributions decrease, particularly near the free edge (0°), when the displacement is held constant and the radius of debond progresses. As a 0.3 *mm* radius is approached, the contributions begin to converge to a near flatline of approximately 30% contribution to G_{total}.

6.6.1.2 *Mode II*

Figure 6.34 presents the effect of debond radius on mode II energy release rates in a linear analysis without residual stress.

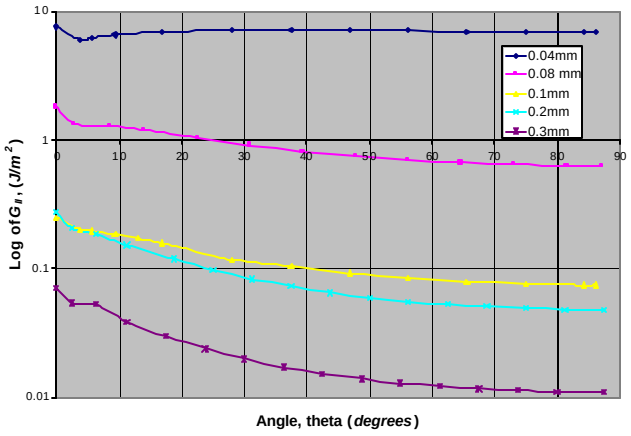

a)

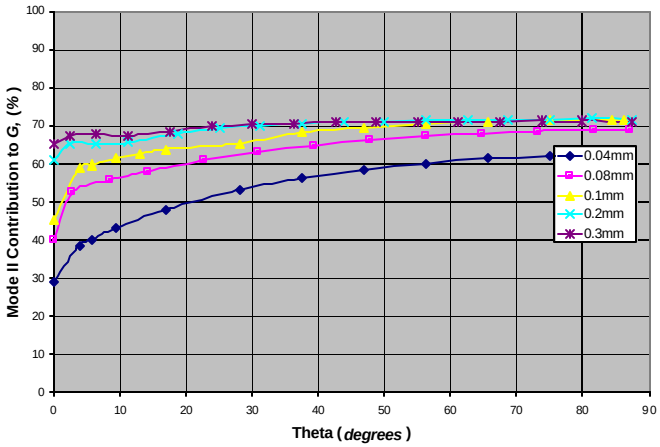

b)

Figure 6.34. a) Linear G_{II} values with varying debond radius
b) Linear %G_{II} contributions with changing debond radius

Figure 6.34a shows that increasing the radius of debond decreases G_{II}, much the same as it decreased G_I in Figure 6.33a. Figure 6.34b indicates that mode II contributions vary inversely to mode I contributions. As the radius of debond increases, mode II contributions increase, particularly near the free edge. Contributions converge towards the 0.3 *mm* radius line, which is an approximate flatline near 70% contribution to G_{total}.

6.6.1.3 Mode III

Figure 6.35 presents the effect of debond radius on mode III energy release rates in a linear analysis without residual stress.

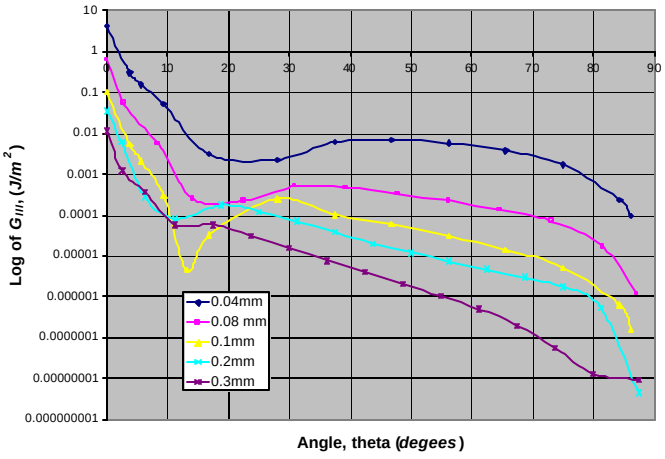

a)

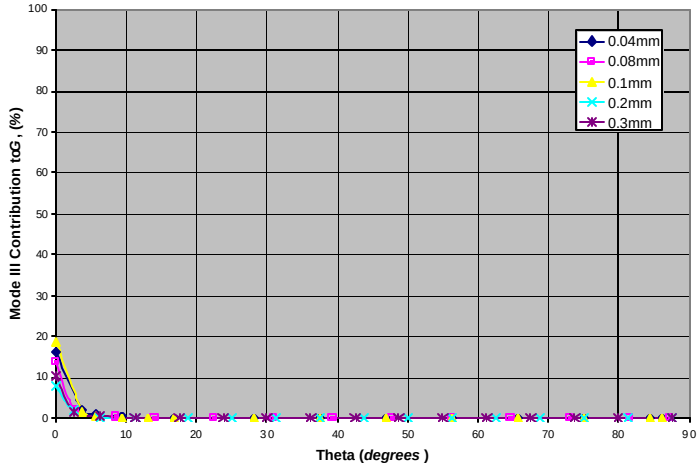

b)

Figure 6.35. a) Linear G_{III} values with changing debond radius
b) Linear %G_{III} contributions with changing debond radius

Although G_{III} is fairly insignificant in linear analyses, Figure 6.35a shows that G_{III} values also uniformly decrease with increasing radius of debond. Figure 6.35b indicates that mode III contributions are negligible except near the free edge. The radius of debond appears to play no role on the amount of contribution from mode III. As previously mentioned, the increase at 0° is caused by Poisson's ratio coupling effects brought on by significant tensile stresses during mechanical loading.

6.6.1.4 Total energy release rate

The effect of length of debond radius on G_{total} in linear analyses without residual stress is presented in Figure 6.36.

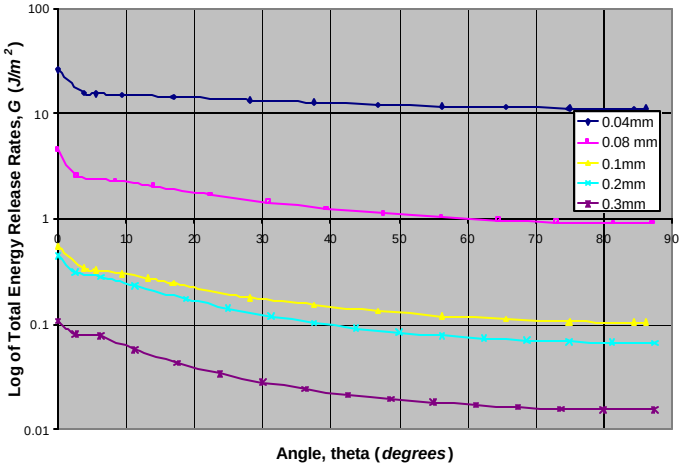

Figure 6.36. Linear G_{total} values with changing debond radius

Figure 6.36 shows that overall energy release rates in linear analyses without residual stress uniformly decrease with increasing radius of debond. Figure 6.37 summarizes the effects of debond radius in a log plot of G components at the free edge, 0°, and at the symmetry edge, 90°, versus radius of debond.

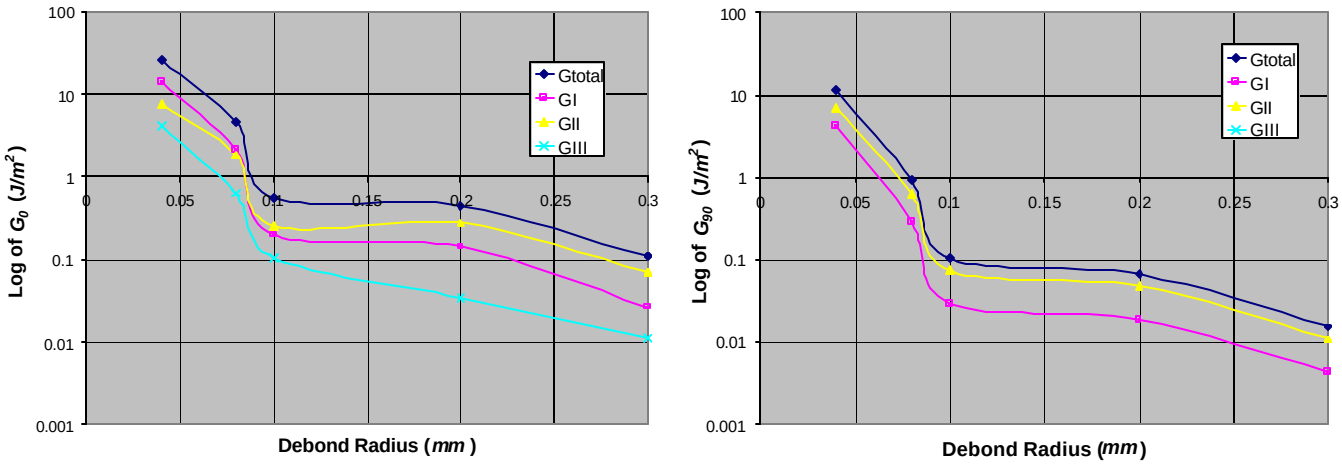

a) **b)**

Figure 6.37. a) Linear *G* components with changing radius at 0°
b) Linear *G* components with changing radius at 90°

Figures 6.37a and 6.37b indicate a decline for all components of *G* values with increasing radius of debond. A small fluctuation occurs at 0.09 *mm* at both the free edge and the symmetry edge, interrupting linear declines. The fluctuation coincides with a changeover in mode dominance from mode I to mode II at the free edge, 0°. This could attribute the fluctuation to the transition from infinite medium behavior to thin plate behavior that is seen as the radius of debond is increased. At small debond radii, the effect is more like an indentation, where only compressive stress and shearing are present. As the radius increases, bending mechanics becomes more prevalent. To determine whether the fluctuation is real or merely an artifact of modeling requires an in-depth analysis of additional debond radii about 0.1 *mm*. G_{III} is absent from Figure 6.37b because the values are zero for all radii.

6.6.2 Non-linear, residual stress

6.6.2.1 Mode I

Figure 6.38 presents the effect of debond radius on mode I energy release rates in a non-linear analysis including residual stress.

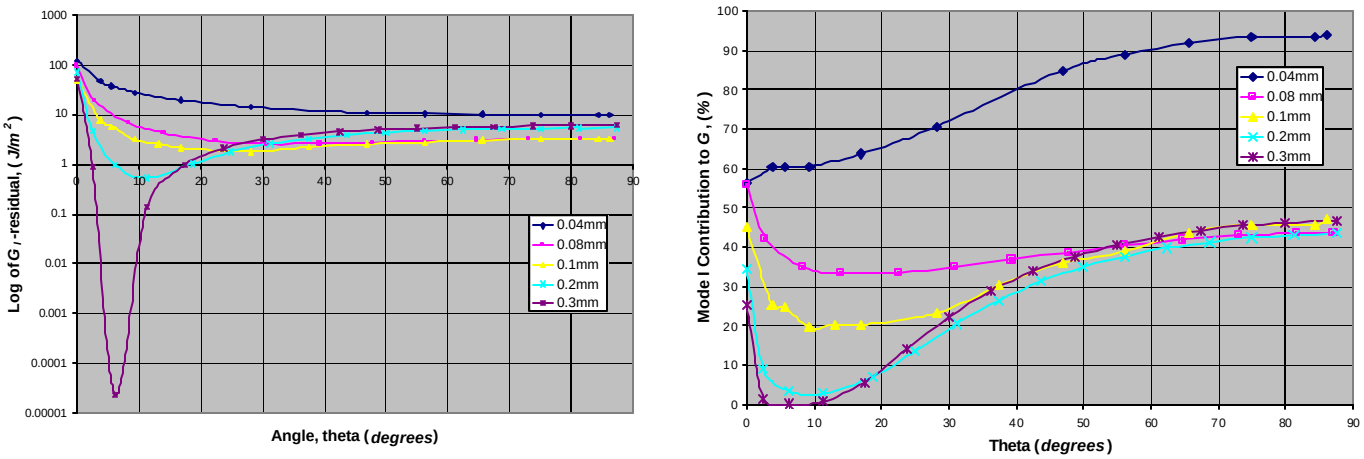

a) **b)**

Figure 6.38. a) Non-linear G_I values with changing radius and residual s
b) Non-linear %G_I contributions with changing radius and residual s

Figure 6.38a shows that increasing the radius of debond significantly decreases G_I at small angles near the free edge. For larger angles in the interior of the film the radius of debond has little effect on G_I. Figure 6.37b indicates that as the debond radius progresses, a decline in mode I contributions at a range of angles from 3° to 15° greatly increases in significance. At a debond radius of 0.3 *mm*, the presence of G_I is absent around 7°, meaning there is no opening effect in the thin film. Past 15° all debond radii except for the smallest of 0.04 *mm* converge to approximately a 45% G_I contribution. The decline in contribution is thought to be an artifact of compressive z-direction stresses brought on by residual stress. As the radius of debond progresses, these stresses become more significant because the transition from shearing to bending weakens the tensile z-direction stresses at the debond from mechanical loading. The value of theta for which G_I contributions become a minimum decreases with increasing debond radius for reasons explained in Figure 6.25.

6.6.2.2 Mode II

Figure 6.39 gives the results for the effect of debond radius on G_{II} in the non-linear analysis with residual stress.

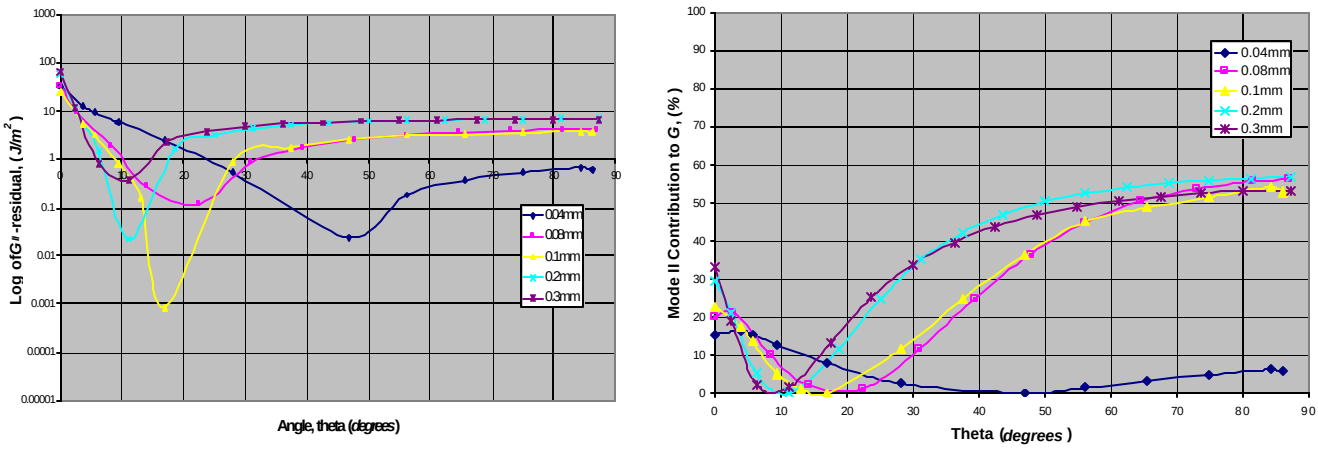

a) **b)**

Figure 6.39. a) Non-linear G_{II} values with changing radius and residual s
b) Non-linear %G_{II} contributions with changing radius and residual s

Increasing the radius of debond in the non-linear residual stress analysis of Figure 6.39a causes an overall increasing of G_{II}. However, a floating minimum shifts its presence towards the free edge (0°) as the debond radius increases. The magnitude of the minimum fluctuates: increasing from 0.04*mm* to 0.1*mm*, and then decreasing from 0.1*mm* to 0.3*mm*. Figure 6.39b indicates a minimum in contribution similar to the minimum in Figure 6.38b. Increasing the radius of debond both narrows the width of the minimum and shifts the point of occurrence from higher thetas to lower thetas. Beyond a 0.04 *mm* debond radius, contributions converge to about 55% at the symmetry plane (90°).

6.6.2.3. Mode III

The effect of debond radius on G_{III} for a non-linear analysis with residual stress is presented in Figure 6.40.

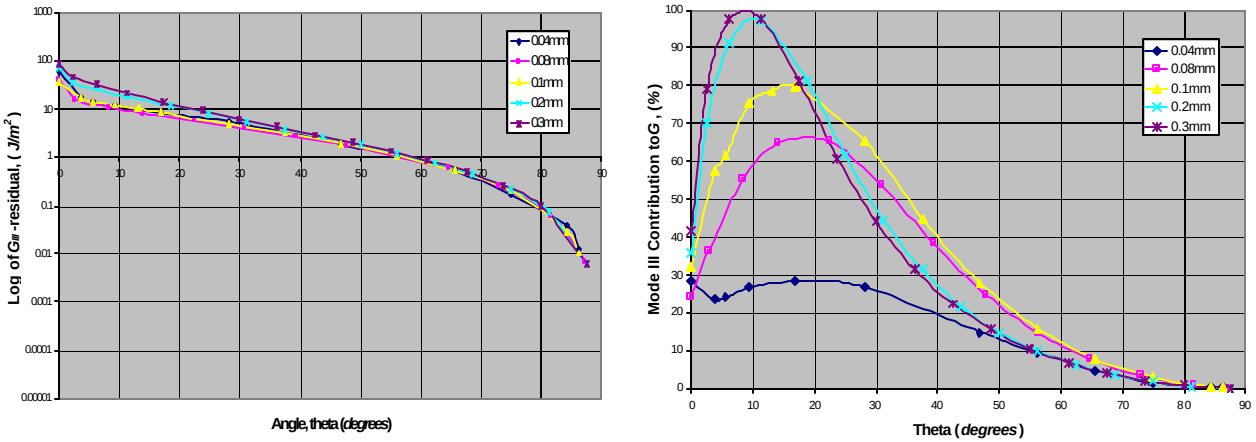

a) **b)**

Figure 6.40. a) Non-linear G_{III} values with changing radius and residual s
b) Non-linear %G_{III} contributions with changing radius and residual s

A lack of change in G_{III} with changing radius is found in the non-linear residual stress analysis of Figure 6.40a. Figure 6.40b shows that the percent contribution of G_{III} largely increases with increasing debond radius, becoming the dominant contributing mode in the absence of mode I and mode II as shown in Figures 6.38b and 6.39b.

6.6.2.4. Total energy release rate

The effect of debond radius on G_{total} for the non-linear residual stress analysis is presented in Figure 6.41.

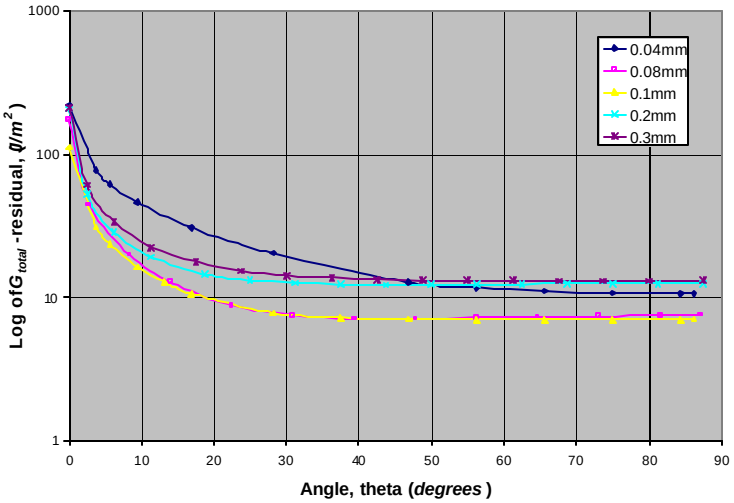

Figure 6.41. Non-linear G_{total} values with changing debond and residual s

Figure 6.41 shows that increasing the length of debond radius for the case of a non-linear analysis with residual stress first lowers the value of G_{total},. Past a debond radius of 0.1 *mm*, increasing the radius of debond increases G_{total}.

Figures 6.42a and 6.42b summarize the effect of debond radius on energy release rates in non-linear analyses with residual stress. The figures present log plots of *G* components at the free edge, 0°, and at the symmetry edge, 90°, versus debond radius.

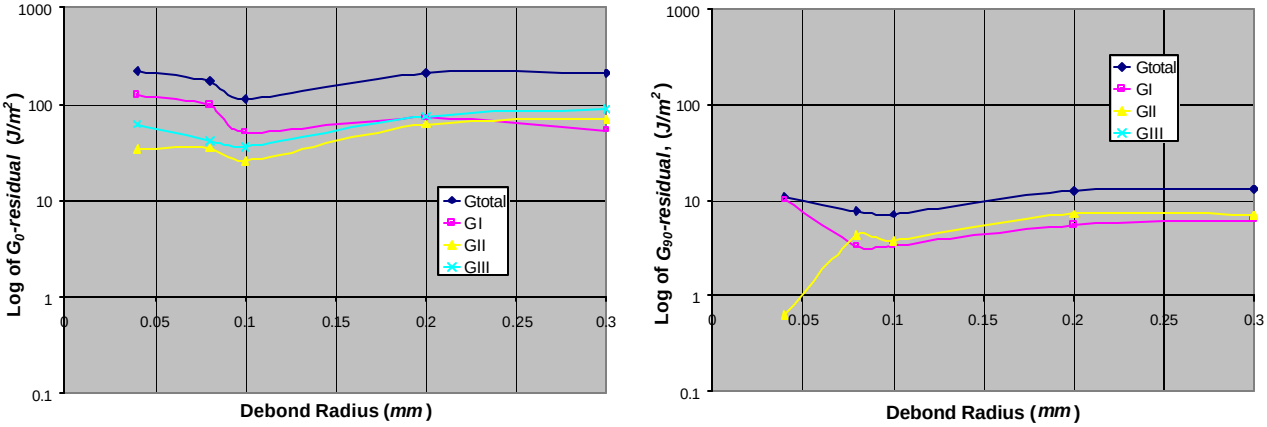

Figure 6.42. a) NL residual *G* components with changing radius at 0°
b) NL residual *G* components with changing radius at 90°

The most notable aspect of Figures 6.42a and b is the order of magnitude difference caused by the free edge in Figure 6.42a. The linear analysis without residual stress in Figure 6.37a did not experience this effect to the same degree. Inclusion of residual stress greatly enhanced the influence of the free edge. All components of *G* still undergo a fluctuation at 0.1 mm, but to a lesser degree than in the linear analysis presented in Figure 6.37. Again, this trend may be due to the transition from infinite medium behavior to thin plate behavior as the radius of debond increases. The free edge also tends to extend mode I dominance because mode I dominance is lost at a much smaller debond radii at 90° that at 0°.

6.7 Chapter Summary

This chapter focused on exploration of the underlying mechanics driving the delamination of coatings during probe tests. The analysis techniques built off of

successfully tested methodologies used on the pressurized and shaft-loaded blister tests of Chapters 4 and 5. A new step-wise methodology for determining energy release rates as a function of an assumed debond shape was developed. Analyses with and without residual stress were run for five different debond radii, 0.04 *mm*, 0.08 *mm*, 0.1 *mm*, 0.2 *mm* and 0.3 *mm*. Data results in the form of energy release rates and mode-mixity were presented for all three fracture modes and in total with and without residual stress. These results were then analyzed for the effects of residual stress, radius of debond, and the free edge.

The data of the 0.1 *mm* debond radius seems to give anomalous behavior in several of the figures of Chapter 6. However, when viewed as a whole, the results are consistent and define a trend. Moreover, additional finite element runs were performed at this debond radius and similar results were obtained. Therefore this anomalous behavior is attributed to a change in mechanics that is taking place, such as a transition from infinite medium behavior to thin plate behavior.

6.7.1 Residual Stress

The inclusion of residual stress into the models significantly impacted results. A sensitivity analysis showed that all individual modes of G as well as G_{total} see higher sensitivity to residual stress near the free edge (small thetas) than in the body of the film. The cause of this was investigated by exposing a swatch of thin film to pure residual stress conditions. This simple test showed that von Mises stresses are high at the free edge and decline until a depth into the material of five times the film thickness, where no more change occurs. High stresses indicate high strains, which reflect high energy release rates, thereby explaining why energy release rates would be more sensitive to residual stress near the free edge (0°). Each fracture mode was impacted differently by residual stress. Residual stress caused percent mode I composition to reduce near the free edge (small thetas) and increase near the symmetry plane (90°). Residual stress decreased percent mode II composition, particularly for thetas just past the free edge (8-22°). On the other hand, residual stress caused a large increase in percent mode III composition in the same range of thetas that percent mode II was reduced. One of the most significant effects of residual stress is the transition of mode II displacements from

negative to positive. Figure 6.43 shows how the angle of transition changes as the radius of debond increases. Plotted alongside this result is the angle of anomalous behavior found in the experimental results shown in progressive debonds of Appendix B.

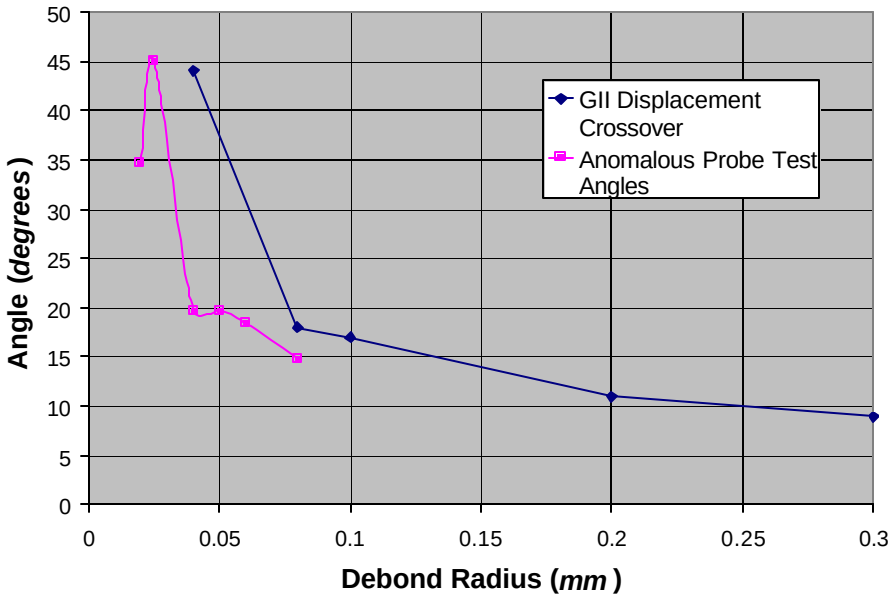

Figure 6.43. Angles of G_{II} crossover and anomalous experimental behavior

Figure 6.43 indicates that both the angle of transition in G_{II} and the angle of anomalous experimental behavior decrease drastically as the radius of debond is increased. There is also strong correlation between the two curves, indicating that the angles of G_{II} crossover may correspond to the angles of shearing or tearing seen at the sides of the delamination pattern of Appendix B. It is a good point to note that both x-y parameters for the plot of Figure 6.43 are measured by hand for the experimental probe test results. This incorporates human error, meaning the curves may very well be even more similar. The changing of angles with increasing radius could be an artifact of switching from half-space behavior to thin plate behavior.

6.7.2 Radius of debond

The radius of debond also plays an important role in energy release rates of the system, affecting both the magnitude and mode mixity. Since residual stress was established to have a significant impact on energy release rate results for thin films, only the solutions including residual stress need be analyzed for dependence on debond radius.

6.7.2.1 Magnitude of G

Concerning the magnitude of energy release rates, increasing the radius of debond in residual stress analyses universally decreases G_I rates, with a sharp minimum developing near the free edge (small thetas) at larger debond radii. G_{II} rates increase with increasing radius, although a fluctuating minimum shifts towards the free edge as well. The largest G_{II} minimum occurs at a radius of 0.1 *mm*. Perhaps the most interesting aspect of the residual stress analyses is that G_{III} rates do not see significant change with increases in radius of debond. The combined effect on G_{total} of increasing the debond radius is to initially decrease G_{total} from 0.04 *mm* to 0.1 *mm*, and thereafter steadily increase G_{total}. This effect is attributed to the loss of infinite medium behavior and the prevailing thin plate behavior.

6.7.2.2 Mode-mixity of G

The radius of debond plays a significant role on mode-mixity as well. Increasing the radius of debond in the residual stress analyses creates an absence in percent mode I contributions around 8°. After initially high mode I contributions at 0.04 *mm*, all other lengths converge to a 40% contribution near the symmetry plane (90°). Percent mode II contributions increase with increasing debond radius. At 0.04 *mm*, mode II contributions are minimal, but as larger radii are reached, mode II contributions begin to follow the same pattern as mode I contributions. Percent mode III contributions greatly increase with increasing radius of debond. A maximum also increases in size and shifts towards the free edge (small thetas) as the radius increases. This maximum corresponds to the minimums of mode I and mode II.

6.7.3 Analysis with respect to Experimental Probe Test

Overall, the results of the finite element analysis of the probe test indicate that debonding will always start at the free edge (0°). Figures 6.41 and 6.42 provide conclusive evidence that the magnitude of total energy release rates is at least 10 times higher at the free edge than at the symmetry plane (90°). For initial debond radii, fracture at the free edge is dominated by the opening mode of fracture, mode I, as seen in mode-mixity plots from Figures 6.36, 6.37, and 6.38 (56% mode I, 16% mode II, and 28% mode III). As the

radius of debond progresses, the free edge maintains approximately the same total energy release rate, but experiences a more even mix of fracture modes (25% mode I, 33% mode II, and 42% mode III). Figures 6.39 and 6.40 also indicate that energy release rates in the presence of residual stress are stable despite progression of debond. Figure 6.41 alone conceals several very significant effects taking place in individual modes of energy release rates. As the debond radius progresses under displacement control, the film experiences steep drop-offs in mode I and mode II energy release rates at a point in the material just beyond the free edge (6-15°) as shown in Figures 6.38a and 6.39a. Although Figure 6.40a shows that mode III energy release rates are unaffected in this zone, the changes in mode I and II along with the changeover in mode II displacements indicate that an out of plane buckling or rippling effect is taking place. With progression of debond, mode I and mode II energy release rates even off beyond 15°as mode III energy release rates descend to zero upon approaching the forced boundary conditions at the symmetry plane. The combined effect of the three modes past 20°, as seen in Figure 6.41, is a fairly even total energy release rate curve. These trends indicate that the film will tend to uniformly debond about theta in the bulk of the material beyond the free edge and beyond the buckling effect, thereby creating a semi-circular debond. These results concur with the delamination patterns seen in the experimental probe test, as shown in Figure 6.1 and Appendix B.

Chapter 7 Summary, Conclusions, and Recommendations

7.1 Review of research objectives

7.1.1 Primary objective

Recall from Chapter 1 that the primary objective of this research was to establish a means of quantifying the energy release rates associated with fracture modes in the probe-loaded thin film/substrate system in order to understand fracture patterns.

7.1.2 Secondary objectives

Several secondary objectives were also developed in Chapter 1 to support the primary objective.

1. Identify the fracture mechanics parameters that represent integrity of adhesion
2. Develop finite element methods by which the fracture parameters can be determined
3. Identify types of finite element models and elements suitable for fracture analysis of thin film/substrate systems
4. Propose key classical test methods to explore the capabilities of thin films bonded to substrates
5. Bound finite element solutions of classical idealized blisters with limiting theory cases to ensure model correlation
6. Interpret finite element results so as to:
    a) Understand the effects of both mechanical loading and residual stresses
    b) Quantify the energy release rates in the form of all three fracture modes
    c) Characterize the effect of length of debond on energy release rates
7. Transfer finite element methodology developed for classical blister tests to probe loading of the edge of a coating

7.2 Conclusions

The chapters of this thesis follow a logical pattern and build on one another. This section discusses the overall key points to take away from the work. For the discussion of key

points, it must be kept in mind that the results of this thesis are based on the material, loading, and boundary conditions specified in tables at the beginning of each chapter.

Chapter 2 set the stage for the thesis by addressing secondary objectives 1&2. Specifically, *Chapter 2* provided the following,

- Reviewed the early developments of fracture mechanics and sought understanding of the driving principles
- Established energy release rates, *G*, as the most suitable parameter for this research.
- Performed general analytical development of energy release rates for fracture mechanics problems from basic fracture mechanics concepts
- Introduced the change in strain energy approach, the modified crack closure method, and the J-integral method for obtaining energy release rates

Chapter 3 builds off of the background from *Chapter 2*, concentrating on model and element selection to fulfill secondary objective 3. The following are key points from the chapter.

- **Model selection**
  - Demonstrated the limitations of structural elements in modeling thin films at the geometry scale in this thesis.
  - Instigated the move towards the use of solid continua elements.
  - Reinforced the fact that significant forethought should be applied to finite element analyses before accepting any results produced by the computer. Particular consideration should be given to:
    - the scale of the problem
    - material properties
    - complexity of geometry and boundary conditions
    - type of loading

- **Element selection**
  - Discussed the advantages and disadvantages of element order of interpolation, element shape, and element degree of integration.

- Compared element types for the geometry of this thesis by using an axisymmetric pressurized blister test case.
- Proved that first-order, reduced integration, quadrilateral elements are most accurate elements for both large debond ($2mm$) and small debond ($0.0067mm$).
- Established that crack closure results from axisymmetric model with small debond radii are inaccurate.
- Proved that increasing the modeling power with a 3-D model obtains accurate crack closure results for small debond radii using first-order, reduced integration brick elements.

Chapter 4 and *Chapter 5* are based on the energy release rate developments of *Chapter 2* and the model and element choices of *Chapter 3*. These chapters address secondary objectives 4, 5, and 6 to build a strong foundation for the finite element analyses. By correlating finite element energy release rates to established analytical solutions for the pressurized blister test in *Chapter 4* and the shaft-loaded blister test in *Chapter 5*, the modeling choices, element choices, and energy release rate extraction methodologies were validated. Thereby, the results of *Chapter 4* and *Chapter 5* on the pressurized and shaft-loaded blister tests proved that the finite element method can provide a reliable assessment of available energy release rates. Validation of the finite element techniques also allowed the finite element analysis to become a productive tool for transcending the limitations of analytical expressions by changing the different variables in the system. In particular, *Chapters 4* and *5* investigated the effects of changing the radius of debond and inclusion of residual stress on blister energy release rates.

- **Increasing the radius of debond**
  - Transitioned blister behavior from infinite medium behavior to thin plate behavior for both the pressurized and shaft-loaded blister tests.
  - Increased energy release rates for pressurized blisters with fixed applied pressure. Applying the same pressure to a larger area creates a larger total load, and thus greater energy release rates, which is in agreement with the finite element results.

- Decreased energy release rates in shaft-loaded blisters under a fixed applied displacement. At a fixed displacement, increasing the length of debond radius would lessen the total energy in the blister, thereby decreasing energy release rates, which corresponds to the finite element results.
- Transitioned mode mixity of energy release rates in both blister tests from mode I dominance at small debond radii to mode II dominance at large debond radii. This trend indicates a change from shearing to bending as the radius of debond increases.

➢ **Inclusion of residual stress**

- Pressurized blister
  - Reduced both blister deflections and blister energy release rates, with more significant influence on large debond radii rather than small.
  - Evened out mode contributions, although the overall trend in mode mixity remained the same.
- Shaft-loaded blister
  - Decreased G_{total} at small debond radii, and increased G_{total} at large debond radii.
  - Increased G_I regardless of length of debond radius.
  - Decreased G_{II} at debond radii less than 0.8 *mm*, otherwise increased $G_{II.}$
  - Transitioned mode-mixity from mode I dominance at very small debond radii to mode II dominance at large debond radii.
  - Had more influence on mode-mixity at larger debond radii, and influenced modes I and II inversely.

Chapter 6 addressed the geometry of the experimental probe test of thin coatings on silicon substrates. The chapter transferred the finite element methodology developed in *Chapter 4* and *Chapter 5* to edge-loaded films, to realize secondary objective 7. The basis of the new finite element model was extracted directly from the three-dimensional models of the pressurized and shaft-loaded blister tests. The only difference between the shaft-loaded blister model and the edge-loaded thin film model was the release of

boundary constraints on one edge. Again, this transition from a well established, correlated solution to a new, unknown solution by the release of only one boundary condition establishes faith in the results of the new model. An step-wise methodology was developed for determining energy release rates at different points about an assumed debond shape. Analyses with and without residual stress were run for five different debond radii, 0.04 *mm*, 0.08 *mm*, 0.1 *mm*, 0.2 *mm* and 0.3 *mm*. The resulting energy release rates and mode-mixity were found to be greatly influenced by both residual stress and the length of debond radius.

- **Inclusion of residual stress**
  - Prompted a sensitivity analysis to determine the sensitivity of energy release rates and mode-mixity to residual stress.
  - Established that all individual modes of G as well as G_{total} are much more sensitive to residual stress near the free edge (small thetas) than in the body of the film. A simple test showed that residual stress induces higher stresses near the free edge than in the body of the film, indicating higher strains, higher energy release rates.
  - Reduced percent mode I composition near the free edge (small thetas) and increased mode I composition near the symmetry plane (90°).
  - Decreased percent mode II composition, particularly for thetas just past the free edge (8-22°).
  - Greatly increased percent mode III composition in the same range of thetas that percent mode II was reduced, indicating tearing.

Having established the significance of residual stress in the thin film, there is no need to further analyze the results of the linear analysis without residual stress.

- **Increasing radius of debond**
  - Non-linear analysis with residual stress
    - Universally decreased magnitude of G_I rates, with a sharp minimum developing near the free edge (small thetas) at larger debond radii.

- Increased G_{II} rates, although a fluctuating minimum shifts towards the free edge as well. The largest G_{II} minimum occurs at a 0.1 *mm* radius of debond.
- Produced no significant change in G_{III} rates.
- Initially decreased G_{total} at radii of 0.04 *mm* to 0.1 *mm*, and thereafter steadily increased G_{total}. This effect is attributed to the loss of infinite medium behavior and consequent prevailing thin plate behavior.
- Aside from the 0.04 *mm* debond radius, reduced mode I composition from 0° to 50°, at which point all radii of debond converge to a 40% contribution near the symmetry plane (90°).
- Increased percent mode II contributions except for a shifting minimum from 20° to 10°.
- Greatly increased percent mode III contributions with increasing debond radius. A maximum also increases in size and shifts towards the free edge (small thetas). This maximum corresponds to the minimums of mode I and mode II.

7.3 Contributions to the Literature

The work contained in this thesis contributes significantly to the literature. The document contains many new and groundbreaking findings based on a new probe test of a half-blister to quantify the adhesion of thin coatings to substrates. The thesis focuses on edge and residual stress effects; topics the majority of adhesive papers do not take into consideration. Both of these effects have significant influence on the delamination of the coating from the substrate.

Delamination of coatings tends to initiate along free edges due to the vulnerability of the interface between coating and substrate to the surrounding environment. The geometry of the probe test exploits this characteristic with out of plane loading at the edge of a coating. This is effectively one-half of a shaft-loaded blister. As noted in the results of this thesis, the free edge acts as a stress intensifier due to the unconstrained geometry.

Residual stress is an extremely important factor to be accounted for in thin film systems. It can come about from thermal mismatch, processing, moisture absorption, and chemical changes to name a few. These issues are all major hurdles that are fought not only in the microelectronics industry, but in all industries that use thin film systems such as automotive and biomedical. Oftentimes, residual stresses can be more influential than actual applied loading, and is thereby accountable for the failure of a part. This thesis accounts for residual stress in both blister and half-blister testing. It demonstrates that residual stress extremely influences both the magnitude and distribution of energy release rates within the coating.

Additionally, the thesis develops a new means of incrementally sampling G about an assumed debond front for comparative analysis of debond. The finite element work allows for a rigorous investigation of all three modes of energy release rates; G_I, G_{II}, and G_{III}. The distribution of each mode of energy release rate allows for determination of dominating mechanics within the system. The development of a step-wise data extraction technique, with an assumed debond front and an assumed coordinate system, allows the direction of future debond propagation to be dictated by comparisons of energy release rates at different locations. This helps to quantify both the adhesion strength and the reliability of the thin film/substrate packages.

Studies on the experimental results seen in Appendix B will be conducted in the near future in Virginia Tech labs to provide a rigorous comparison to the theoretical results developed in this thesis. These studies will be based on the optical interference fringe patterns and on the out-of-plane deformation profiles induced by 45° probe loading.

7.4 Recommendations for Future Research

7.4.1 In-plane loading

The work included in this thesis has been limited to out-of-plane film loading. Future research could include in-plane as well as out-of-plane loading. This lateral loading can be incorporated into models using forced displacements as indicated in Figure 7.1.

Figure 7.1 shows preliminary findings for a linear analysis of prescribed in-plane loading of a coating with a 0.08 *mm* debond radius. A rigid plane representing the substrate is placed under the coating to ensure that the coating does not displace below its original bottom plane.

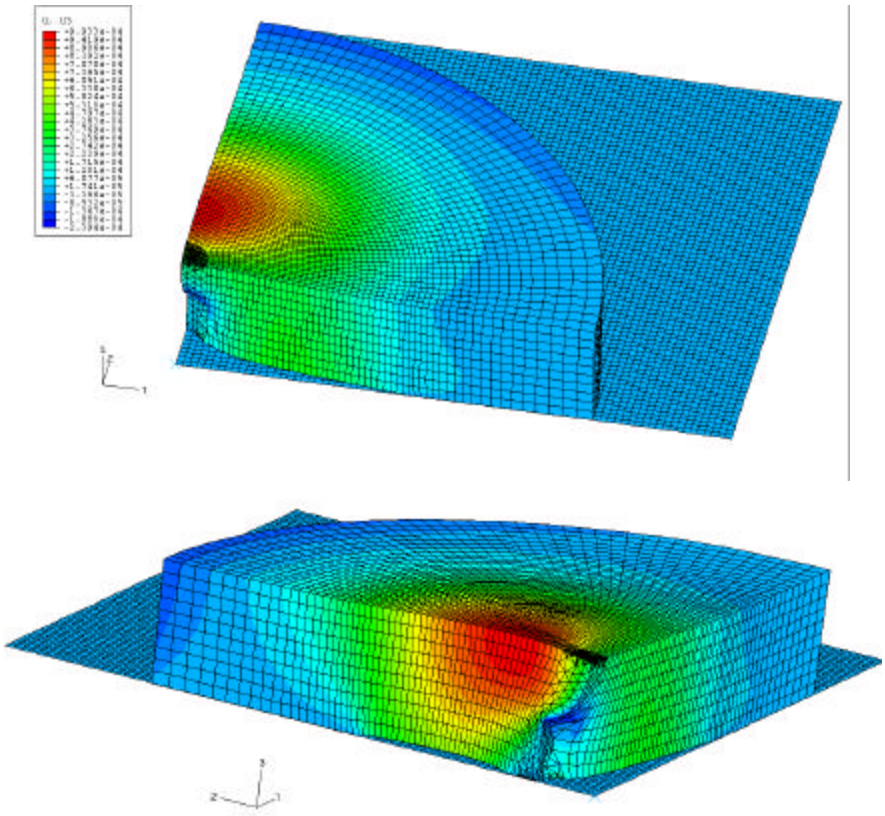

Figure 7.1. Z-direction displacement contours of in-plane probe loading at a 0.08 *mm* debond radius

Figure 7.2 indicates the preliminary energy release rate results associated with the geometry pictured in Figure 7.1.

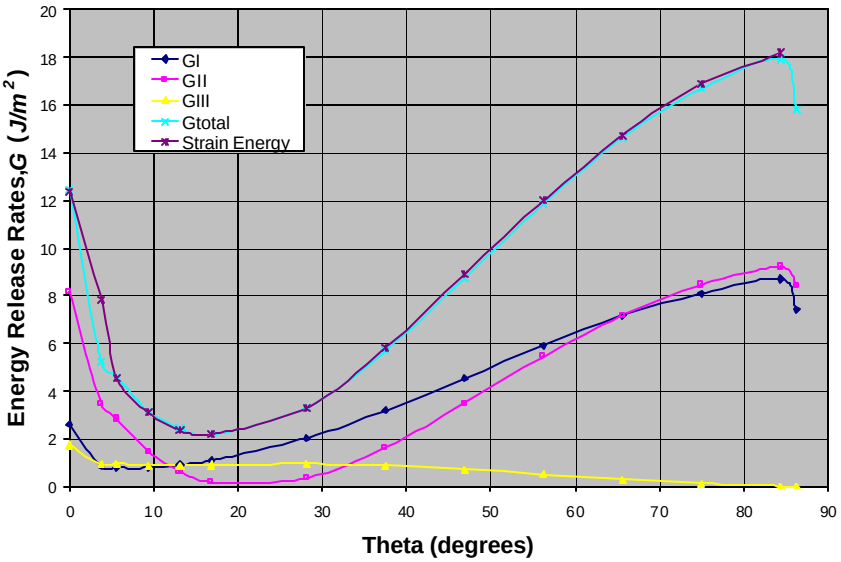

Figure 7.2. Energy release rates for in-plane loaded blister at a 0.08*mm* debond radius

The energy release rate curves in Figure 7.2 resulting from the linear analysis of in-plane loading are far different than the energy release rate curves developed for linear analyses of out-of-plane loading, as indicated in Figure 7.3. In-plane loading causes a significant decline in both mode I and II energy release rate magnitude around 10 and 20°, respectively. Another difference to note is the high energy release rates at 90° for the in-plane loading conditions, which is not seen in the results for the out-of-plane loading conditions.

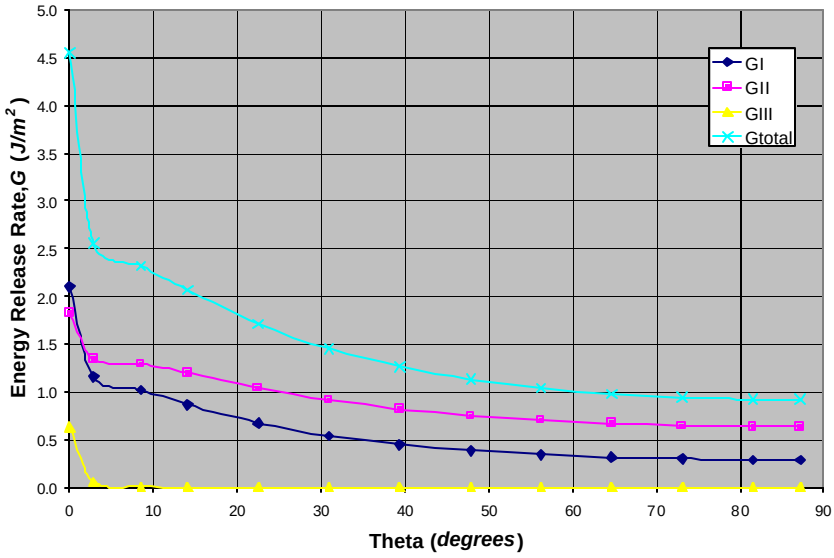

Figure 7.3. Energy release rates for out-of-plane loaded blister at a 0.08*mm* debond radius

7.4.2 Contact modeling

For insight into the localized effects of probe loading, the actual geometry of the probe can be modeled in ABAQUS/CAE as a rigid part. Contact between the probe and the thin film can then be established in the finite element models. A rigid plane would also be modeled to serve as the substrate. The probe and substrate parts are instanced into the film/substrate assembly. Contact can be established by specifying the probe and substrate as master surfaces. The film would be denoted as the slave surface. For initial models, contact behavior could be set as tangential, frictionless contact between the surfaces. Loading then occurs by prescribing a fixed displacement to the probe. Figure 7.4 presents the preliminary resulting von Mises stress contours from a probe loaded film with a debond radius of 0.08 *mm*. The analysis is non-linear due to the large deformations encountered and complex loading by contact.

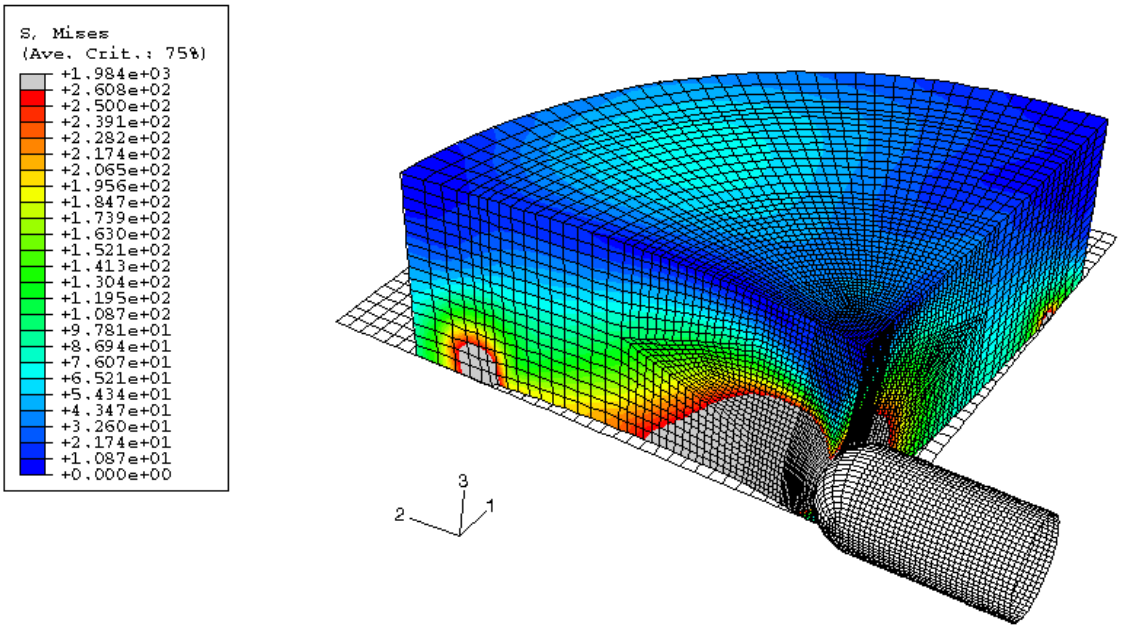

Figure 7.4. Contact probe loading of a thin film with a debond radius of 0.08 *mm*

7.4.3 Advanced material model

The material model used throughout this thesis has been limited to linear elasticity. The only properties specified were the elastic modulus and Poisson's ratio. Future work might include further development of the material model by incorporating any of the

following: hyperelasticity, plasticity, viscoelasticity, or hysteresis. An in-depth analysis of material characterization of adhesives in ABAQUS 6.1 can be found in Appendix B.

7.4.4 Interface elements

This thesis only calculates the available energy release rates associated with delamination. It does not predict where a crack may initiate, or in which direction it may propagate. Future studies could include interface elements, such as springs between the substrate and film to represent adhesion. Based on the stress in the system, the springs could detach once a specified critical energy release rate is reached, thereby releasing the film from the substrate.

References

1. C.E. Inglis, "Stresses in a plate due to the presence of cracks and sharp corners", *Proc Inst Naval Arch*, Vol 55, pp. 219-30, 1913.

2. A.A. Griffith, "The phenomenon of rupture and flow in solids", *Phil. Trans. Roy. Soc. London*, A221, pp. 163-98, 1920.

3. B. Cotterel, "The past, present, and future of fracture mechanics", *Engineering Fracture Mechanics*, Vol 69, pp533-553, 2002.

4. K.L. DeVries, P.R. Borgmeier, Chapter 5. Testing of Adhesives, *Handbook of Adhesive Technology*, Marcel Dekker Inc., 1994.

5. A.C. Fischer-Cripps, *Introduction to Contact Mechanics*, Chapter 2, pp 31-48, Springer-Verlag New York, Inc, 2000.

6. G.R. Irwin, "Onset of fast crack propagation in high strength steel and aluminum alloys", *Proceedings of the 2nd Sagamore Ordinance Materials Conference*, 2, pp 289-305, 1956.

7. J.A. Kies, H.L. Smith, "Toughness testing of hot-stretched acrylics", *Proc. Aircraft Industries Association and Air Development Command Joint Conference*, Dayton, OH, 1955.

8. H.P. Rossmanith, "The struggle for recognition of engineering fracture mechanics", *Fracture research in retrospect*, Rotterdam, AA Balkema, pp 37-93, 1997

9. G.R. Irwin, "Analysis of stresses and strains near the end of a crack traversing a plate", *Journal of Applied Mechanics*, Vol 24, pp 361-364, 1957.

10. D.A. Dillard, III Fracture Mechanics, CASS/ASC Adhesion Science Short Course, Virginia Tech, 2001.

11. Sankar, B.V., "A finite element for modeling delaminations in composite beams", *Computers and Structures*, Vol. 38, No. 2, pp 239-246, 1991.

12. K-T Wan, Personal communication, Virginia Polytechnic Institute and State University, Blacksburg, VA, November 2001.

13. S. J. Bennett, K. L. DeVries, M. L. Williams, "Adhesive fracture mechanics", *Int. J. Fracture*, Vol. 10, No. 1, pp. 33-43, March 1974.

14. Rybicki, Kanninen, “A finite element calculation of stress intensity factors by a modified crack closure integral”, *Engineering Fracture Mechanics*, Vol 9, pp. 931-938, 1977.

15. J.R. Rice, “A path independent integral and the approximate analysis of strain concentrations by notches and cracks”, *J. Appl. Mech. Trans.*, ASME, 85, 588, 1963.

16. M.A. Pinheiro, B.V. Sankar, “Beam finite element for analyzing free edge delaminations”, *Journal of Thermoplastic Composite Materials*, Vol. 13, pp 272-291, July 2000.

17. D. Zhao, Y. Wang, “Mode III fracture behavior of laminated composite with edge crack in torsion”, *Theoretical and Applied Fracture Mechanics*, 29, pp109-123, 1998.

18. ABAQUS/Standard User’s Manual, Volume I, Version 5.8, pp 7.8.1-7.8.2, Hibbitt, Karlsson & Sorensen, Inc. 1998

19. ABAQUS/Standard Example Problems Manual, Volume I, Version 5.8, pp 3.1.6-9, Hibbitt, Karlsson & Sorensen, Inc. 1998.

20. H.K. Kim, S.B. Lee, “Stress Intensity Factors of an oblique edge crack subjected to normal and shear tractions”, Theoretical and Applied Fracture Mechanics, Vol 25, Issue 2, pp. 147-154, Sept. 10, 1996.

21. Y. Cao, “Three-dimensional finite element modeling of subsurface median crack in trilayer sandwiches due to contact loading”, *Engineering Fracture Mechanics*, 69, pp 729-743, 2002.

22. Shell Elements in ABAQUS, Hibbit, Karlsson, Sorensen, Inc. 1993.

23. ABAQUS/Standard User’s Manual, Volume II, Version 5.8, Chapters 14,15, Hibbit, Karlsson, Sorensen, Inc. 1998.

24. Cook, R. D., “Finite Element Modeling for Stress Analysis”, Chapter 4, John Wiley & Sons, Inc., 1995.

25. M. L. Williams, “Continuum interpretation for fracture and adhesion”, *Journal of Applied Polymer Science*, 13, pp 29-40, 1969.

26. G. P. Anderson, S. J. Bennett, K. L. DeVries, “Analysis and testing of adhesive bonds”, New York Academic Press, 1977.

27. H. M. Jensen, “The blister test for interface toughness measurement”, *Engineering Fracture Mechanics*, Vol. 40, No. 3, pp 475-486, 1991.

28. KT Wan, YW Mai, "Modified blister tests for evaluation of thin flexible membrane adhesion on rigid substrate", *Materials Science Research International*, 1, issue 2, pp78-81, 1995.

29. J. G. Williams, "Energy release rates for the peeling of flexible membranes and the analysis of blister tests", *International Journal of Fracture*, 87, pp. 265-288, 1997.

30. KT Wan, SC Lim, "The bending to stretching transition of a pressurized blister test", *International Journal of Fracture*, 92, pp L43-L47, 1998.

31. Timoshenko, Woinowsky-Krieger, *Theory of Plates and Shells*, McGraw-Hill Book Company, 1959.

32. V. I. Mossakovskii, M. T. Rybka, "Generalization of the Griffith-Sneddon criterion for the case of a non-homogeneous body", *PPM*, 28, pp 458-464, 1964.

33. I. N. Sneddon, "The distribution of stress in the neighborhood of a crack in an elastic solid", *Proceedings of Royal Society of London A*, Vol. 187, no. 1009, pp 229-260, (1946).

34. H.M. Jensen, J.W. Hutchinson, K.-S. Kim, "Decohesion of a cut prestressed film on a substrate.", *Int. J. Solids Structures*, 26, pp.1099-1114, 1990.

35. B. M. Malyshev, R. L. Salganik, "The strength of adhesive joints using the theory of cracks", *International Journal of Fracture*, 1, pp 114, 1965.

36. KT Wan, YW Mai, "Fracture mechanics of a shaft-loaded blister of thin film flexible membrane on rigid substrate", *International Journal of Fracture*, 74, pp 181-197, 1995.

37. KT Wan and K Liao, "Measuring mechanical properties of thin flexible films by a shaft-loaded blister test", *Thin Solid Films*, 352, pp 167-172, 1999.

38. KT Wan, "Fracture mechanics of a shaft-loaded blister test – Transition from a bending plate to a stretching membrane", *Journal of Adhesion*, 70, pp 209-219, 1999.

39. KT Wan, S. Guo, D.A. Dillard, "A theoretical and numerical study of a thin clamped circular film under an external load in the presence of residual stress", *Thin Solid Films*, 2003 in print.

40. K. L. Johnson, Contact Mechanics, Chapter 2&3, Cambridge University Press, 1985.

41. Modeling Rubber in ABAQUS, Hibbitt, Karlsson & Sorensen, Inc. 2001.

42. W.D. Callister, Jr., Materials Science and Engineering, An Introduction, 3rd edition, John Wiley & Sons, Inc., 1994.

Appendix A J-Integral ABAQUS/Standard Code

```
*Heading
**
**Establish key node positions for J-integral mesh
*NODE
100001,1,0
100033,.99,0
100233,.99,.008
101033,1.01,.008
101201,1,0
101233,1.01,0
112233,.99,.025
113033,1.01,.025
**Begin node specification for standard mesh created in CAE
      1,         1.01,         0.04
      .
      .
      .
      8945,       0.0022,           0.
**End node specification
**Begin element specification for standard mesh created in CAE
*Element, type=CAX8
  1,    1,   15,  605,  127, 3083, 3084, 3085, 3086
  .
  .
  .
  2782, 3082,  376,   12,  377, 8494, 8944, 8945, 8942
**End element specification
**Generate all elements
*Elset, elset=solid, generate
    1,  2782,     1
**Enter node sets
*NGEN, NSET=TIP
100001,101201,50
*NGEN,NSET=BOUND1
100033,100233,50
*NGEN,NSET=BOUND2
101033,101233,50
*NGEN,NSET=ARCBOUND
100233,101033,50
**
**NGEN,NSET=ARCBOUND,LINE=C
**100233,101033,50,109999
**
*NSET,NSET=OUTBOUND
BOUND1,ARCBOUND,BOUND2
*NFILL,NSET=TIPMESH,SINGULAR=1
TIP,OUTBOUND,16,2
*NGEN,NSET=LIN12233
112233,113033,50
*NFILL,NSET=MIDDLE
ARCBOUND,LIN12233,8,1500
**Specify element type, and declare elements
*ELEMENT,TYPE=CAX8
```

```
100001,100001,100101,100105,100005,100051,100103,100055,100003
100233,100233,100333,103333,103233,100283,101833,103283,101733
**Generate specific element sets
*ELGEN,ELSET=TIPMESH
100001,12,100,100,8,4,4
*ELGEN,ELSET=TOPMID
100233,8,100,100,4,3000,3000
*ELSET,ELSET=ALLELS
TIPMESH,TOPMID,solid
**Prescribe the section for the part
*Solid Section, elset=ALLELS, material=su8
1.
**Specify nodes for node set CLAMPED SURFACE to later be constrained
**CLAMPED SURFACE
*Nset, nset=_G45
    4,    6,   22,   23,   24,   25,   26,   27,   28,   29,   30,
31,   32,   33,   34,   35
   36,   37,   38,   39,   40,   41,   42,   43,   44,   45,   46,
47,   48,   49,   50,   51
   52,   53,   54,   55,   56,   57,   58,   59,   60,   61,   62,
63,   64,   65,   66,   67
   68,   69,   70, 3112, 3133, 3154, 3175, 3196, 3217, 3238, 3259,
3280, 3301, 3322, 3343, 3364
 3385, 3406, 3427, 3448, 3469, 3490, 3511, 3532, 3553, 3574, 3595,
3616, 3637, 3658, 3679, 3700
 3721, 3742, 3763, 3784, 3805, 3826, 3847, 3868, 3889, 3910, 3931,
3952, 3973, 3994, 4015, 4036
 4057, 4078, 4099, 4120, 4141
*Elset, elset=_G45, generate
  10,  500,   10
*NSET,NSET=_G46,generate
101201,101231,2
**Specify elements and surfaces for OUTER SURFACE set
**OUTER SURFACE
*Elset, elset=_solidboundright_S1, generate
 5, 10,  1
*Surface, type=ELEMENT, name=solidboundright
_solidboundright_S1, S1
*Elset, elset=_solidboundtop_S4, generate
 501,  529,    4
*Surface, type=ELEMENT, name=solidboundtop
_solidboundtop_S4, S4
*Elset, elset=_solidboundleft_S4, generate
 1433,  2558,   225
*Surface, type=ELEMENT, name=solidboundleft
_solidboundleft_S4, S4
**Specify elements and surfaces for INNER SURFACE set
**INNER SURFACE
*ELSET,ELSET=_IN_1
101129,101029
*ELSET,ELSET=_IN_2
100933,103933,106933,109933
*SURFACE,TYPE=ELEMENT,NAME=INRIGHT1
_IN_1,S3
*SURFACE,TYPE=ELEMENT,NAME=INRIGHT2
_IN_2,S2
**
```

```
*ELSET,ELSET=_IN_3
109233,109333,109433,109533,109633,109733,109833,109933
*SURFACE,TYPE=ELEMENT,NAME=INTOP
_IN_3,S3
**
*ELSET,ELSET=_IN_4
109233,106233,103233,100233
*ELSET,ELSET=_IN_5
100129,100029
*SURFACE,TYPE=ELEMENT,NAME=INLEFT1
_IN_4,S4
*SURFACE,TYPE=ELEMENT,NAME=INLEFT2
_IN_5,S3
**Apply contact conditions, tying surfaces together
**TIE SURFACES
*TIE,NAME=GLUE1
INRIGHT1,solidboundright
*TIE,NAME=GLUE2
INRIGHT2,solidboundright
*TIE,NAME=GLUE3
INTOP,solidboundtop
*TIE,NAME=GLUE4
INLEFT1,solidboundleft
*TIE,NAME=GLUE5
INLEFT2,solidboundleft
**
** Initiate loading
**PRESSURE LOADING
*Elset, elset=__G9_S3, generate
 2558,  2782,     1
*Surface, type=ELEMENT, name=_G9
__G9_S3, S3
*ELSET,ELSET=__G11,generate
100001,100029,4
*Surface,type=ELEMENT,name=_G11
__G11,S1
** Specify material properties
** MATERIALS
**
*Material, name=su8
*Elastic
3400., 0.32
** ----------------------------------------------------------------
** Initiate first loading step
** STEP: load&bcs
**
*Step
*Static
**
** APPLY BOUNDARY CONDITIONS and LOADS to sets created earlier
**
** Name: clamped Type: Symmetry/Antisymmetry/Encastre
*Boundary
_G45, ENCASTRE
_G46, ENCASTRE
**
** LOADS
```

```
**
** Name: press   Type: Pressure
*Dsload
_G9, P, 0.0068947
_G11, P, 0.0068947
** Specify the node/element set at which the crack occurs
*CONTOUR INTEGRAL, FREQUENCY=1, CONTOURS=4, OUTPUT=BOTH
TIP, 1.0, 0.0
**
** OUTPUT REQUESTS from ABAQUS
**
*Restart, write, frequency=1
*Output, field, variable=PRESELECT
*Output, history, variable=PRESELECT
*El Print, freq=999999
*Node Print, freq=999999
*End Step
```

Appendix B Progressive Delamination of Coating

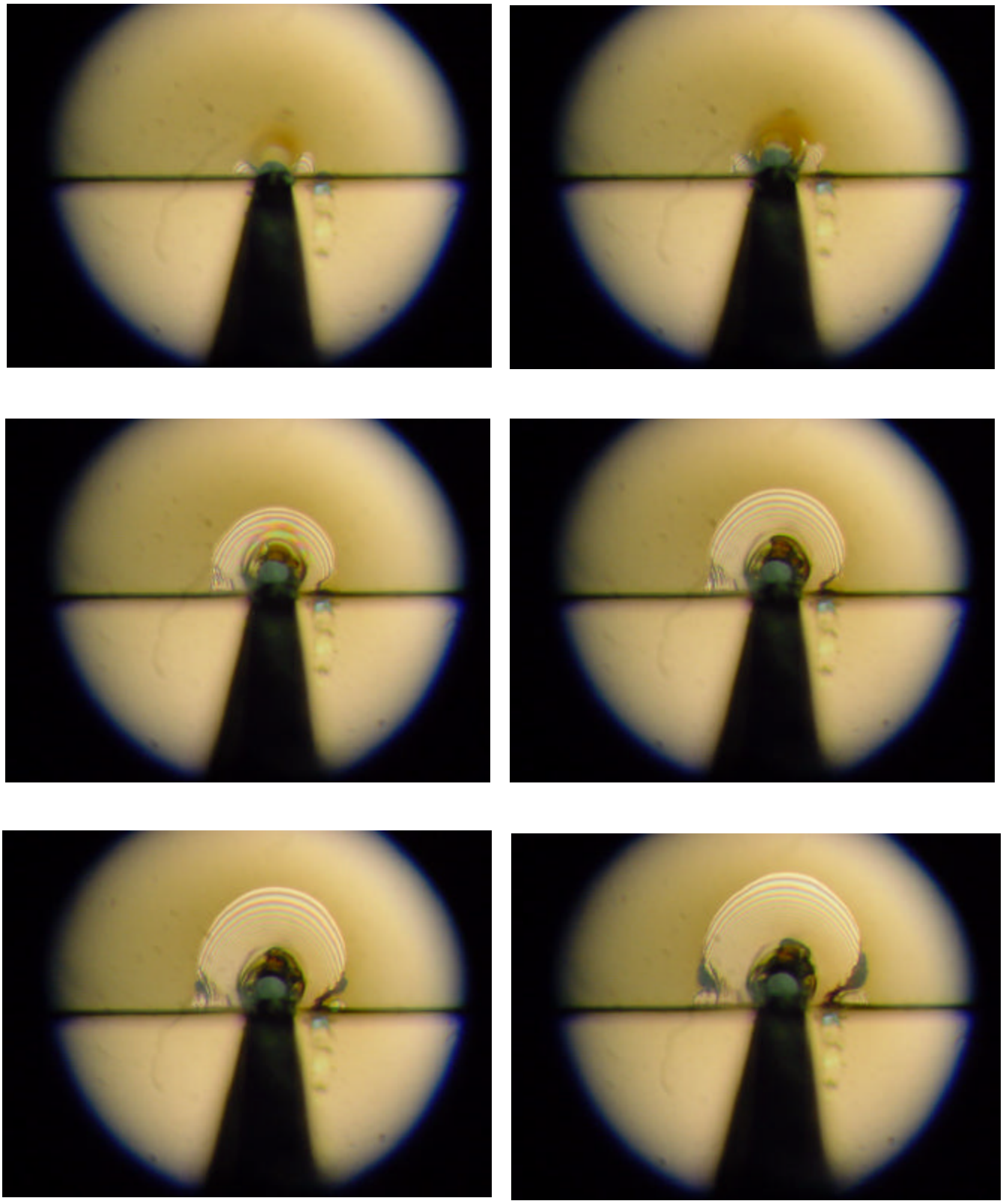

Appendix C Material Characterization of Adhesives in ABAQUS 6.1

The following material characterization of adhesives for ABAQUS 6.1 is based on readings of [30] and [31].

Four components

- Elasticity
- Hyperelasticity
- Viscoelasticity
- Hysteresis

C.1 Elasticity

ABAQUS linear elastic material model is valid for small elastic strains (<5%). The material can be isotropic, orthotropic, or fully anisotropic. These features indicate the directional dependence of the material.

Isotropic – physical properties are independent of the direction of measurement. ABAQUS requires Young's Modulus (E) and Poisson's ratio (υ).

Anisotropic – properties of single crystals depend on the crystallographic direction in which measurements are taken. Extent of anisotropy depends on the symmetry of the crystal structure. ABAQUS requires 21 independent elastic stiffness parameters.

Orthotropic – three mutually perpendicular planes of elastic symmetry. ABAQUS requires Young's Modulus, Shear Modulus (G), and Poisson's ratio for each principal material direction.

For incompressible materials, Poisson's ratio approaching 0.5, use hybrid elements.

C.2 Hyperelasticity

Hyperelasticity in ABAQUS provides a means to model solid rubbers (large strains). The following assumptions are made:

- Material is elastic
- Material is isotropic
- Material is nearly incompressible
- Deformation occurs instantly unless using a viscoelastic or hysteresis model as well

Mechanical behavior is expressed in terms of strain energy potential, U. The strain energy function is expressed in terms of strain invariants I_1, I_2, and J_{el} as $U=U(I_1,I_2,J_{el})$. Any of the following test methods can be used to specify hyperelasticity in ABAQUS.

1. Uniaxial (tension/compression) tests
2. Equibiaxial Tension Test
3. Planar tension test (pure shear test for solid rubbers)
4. Volumetric test

ABAQUS requires nominal stress-nominal strain data for input from tests 1-3, and pressure/volume ratio data from test 4.

2 Model Bases

1. **Physically motivated models**

   Based on microstructure. Rubber is idealized as long chains of crosslinked polymeric molecules. (Arruda-Boyce, Van der Waals)

2. **Phenomenological models**

   Based on continuum mechanics, where the mathematics framework characterizes the stress-strain behavior of the material. (Mooney-Rivlin, Reduced Polynomial, Neo-Hookean, Yeoh, Ogden)

ABAQUS automatically evaluates the different models to correlate predicted model behavior and experimental test data by performing standard unit element tests.

Model Selection

If test data is limited, or data from only one test setup is available, higher order polynomial models such as Ogden should be avoided. Instead physically motivated

models or reduced polynomial models such as Yeoh should be applied. If full data is available, Ogden well tend to provide the best fit to rubber.

Material Damage

Rubber often exhibits elasticity damage during cyclic loading, so preliminary load cycling should be performed to obtain a stationary state before taking final measurements for input to ABAQUS.

C.3 Viscoelasticity

Viscoelastics are rubbery solid materials that exhibit the combined mechanical characteristics of two extremes:

- Low temperature materials which behave elastically for relatively small deformations
- High temperature materials which exhibit viscous or liquid-like behavior

Viscoelastics show instant deformation, which means that total deformation or strain occurs the instant stress is applied or released. (ie. strain is independent of time) Upon release of stress, deformation is totally recovered.

ABAQUS viscoelastics are materials that are rate dependent and behave elastically.

Two components

- Creep
- Relaxation

Two types of linear viscoelasticity in ABAQUS

- Classical: small strain theory w/ instantaneous stress proportional to strain
- Finite Strain: hyperelastic theory (large strains) w/ relaxation rate proportional to stress. E(t) (relaxation modulus) depends on magnitude and direction of straining. Thus a strain energy function is required, such as Polynomial or Ogden Energy functions
- THUS, HYPERELASTICITY AND VISCOELASTICITY COMBINE

Temperature dependence affects

- Instantaneous response
- Rate of relaxation

Frequency Domain Response

- Apply sinusoidal strain, stress response out of phase w/ strain, strain lags by δ
- Two components
  - "In phase" Storage Modulus Gs

$$G_s = \frac{s_o}{g_o}\cos d$$

  - "Out-of phase" Loss Modulus G_L

$$G_L = \frac{s_o}{g_o}\sin d$$

- Frequency domain viscoelasticity can only be used with *STEADY STATE DYNAMICS DIRECT

Time-Temperature Correspondence

- Logarithmic time shifts

$$h(q) = -\log(A(q))$$

  with $h(\theta)$ the horizontal shift of the curve at temp θ from the curve at temp θ_o and $A(\theta)$ the time reduction factor at temp θ relative to a reference temp θ_o.

- Relaxation curves can be extrapolated using master curves technique (use high temps to simulate long time periods)

Viscoelastic Parameters

3 ways to define

1. Direct input of Prony Series parameters
2. Creep test data
3. Relaxation test data

- ABAQUS uses Prony Series Representation which requires Shear and Bulk Relaxation Moduli
- G_o and K_o taken from *ELASTIC data option (E,υ)
- ith parameters taken from either relaxation or creep data, or direct input

C.4 Hysteresis

ABAQUS defines hysteresis as general, non-linear, finite-strain time/strain rate dependent behavior of materials that undergo comparable elastic and inelastic strains. Hysteresis arises when creep or relaxation rate is not proportional to the stress. Creep and stress relaxation will become more pronounced at higher stress levels, and creep and relaxation will occur faster initially and plateau more slowly than with viscoelasticity. Hysteresis is characterized by the following three properties:

1. Repeatability of results
2. Lack of permanent set after one completed load cycle
3. Higher rate dependence during loading than during unloading

ABAQUS employs the Bergstrom & Boyce model. This model assumes large elastic and creep strains, creep response due only to deviatoric behavior (volumetric response is purely elastic), and non-linear dependence on strain rate. The mechanical response is decomposed into two parts:

A. Equilibrium network that corresponds to the state that is approached in long-time stress relaxation tests.
B. Time dependent network that captures the nonlinear rate-dependent deviation from the equilibrium state.

The two are combined to form Eq. B.1.

$$Total\ Stress = Network\ A + Network\ B \tag{B.1}$$

Hysteresis in ABAQUS is characterized by the following effective creep strain rate in network B,

$$\dot{e}_B^{cr} = A(l_B^{cr} - 1)^C s_B^m. \tag{B.2}$$

In Eq. B.2,

λ_B-1 = nominal creep strain in Network B
σ_B = effective stress in Network B = Sqrt[3/2 S_B:S_B]
S_B = deviatoric Cauchy stress tensor
λ_B = Sqrt[1/3 I:C_B]
$C_B = [F_B]^T * F_B$
F = deformation gradient acting on both networks

The following four parameters define hysteresis in ABAQUS.

- The positive exponent, m, characterizes the scalar effective stress dependence of the effective creep strain rate in Network B.

- The exponent C:{-1,0}, characterizes the creep strain dependence on the creep strain rate in Network B.

- The non-negative constant A is the effective creep strain rate that maintains dimensional consistency in the equation

- The stress scaling factor S defines the ratio of the stress of Network B to the stress of Network A under instantaneous loading.

Hyperelasticity must be defined along with Hysteresis in the ABAQUS material definition.

C.5 Required/preferred test data

For Elastic formulation:

E, ν

For Hyperelastic formulation:

1. Uniaxial (tension/compression) tests
2. Equibiaxial Tension Test
3. Planar tension test (pure shear test for solid rubbers)

Nominal Stress/Nominal strain curves

For Viscoelastic formulation:

Creep or Relaxation Test Data

Relaxation Modulus vs time curve or Creep Modulus vs time curve

$$E_r(t) = \frac{s(t)}{e_0} \qquad E_c(t) = \frac{s_0}{e(t)}$$

Tests:

Stress relaxation: specimen is strained rapidly to a certain level and maintained there. The stress necessary to maintain this strain is measured as a function of time.

Creep test: instantly apply a stress and maintain a certain level while strain is measured as a function of time

For Hysteresis formulation: See Section B.4.

Vita

Kristopher Patrick Mount

Kristopher Patrick Mount was born May 27, 1978 in Washington, D.C to parents James and Dolores Mount. His entire childhood was spent in White Plains, MD. He graduated from Maurice J. McDonough High School in May 1996 and began his college career at UMBC in Baltimore, MD the following fall. After only one semester, he transferred to Virginia Tech in January of 1997. As an undergraduate, Kris worked winters and summers at the Naval Surface Warfare Center (NSWC) in Indian Head, MD. Under the CAD/PAD program, he assisted senior engineers in both design and maintenance of rocket motors for ejection seats of Navy aircraft. He graduated Virginia Tech in May 2000 with a Bachelor's of Science in Mechanical Engineering with Magna Cum Laude honors.

After a summer of full-time hire with NSWC, Kris entered graduate school at Virginia Tech in the fall of 2000. Having entered into an advanced 5 year Bachlor's/Master's program, he spent the first year in classes and supporting an undergraduate finite element course under Bob West. In the fall of 2001, Kris entered into a project supported by Hewlett Packard and the Center of Adhesive and Sealant Science (CASS) at Virginia Tech. This ended up as his thesis project.

Upon completion of his master's degree, Kris will be returning to work in the CAD/PAD department at the Naval Surface Warfare Center in Indian Head, MD as a design engineer.